ISSN 2222-5617

МІНІСТЕРСТВО ОСВІТИ І НАУКИ УКРАЇНИ

Вісник Харківського Національного Університету імені В.Н.Каразіна

№ 1158

Серія “Фізика”

Випуск 22

Серія започаткована 1998 р.

Харків 2015

УДК 530.1/539.8

Вісник містить статті, присвячені сучасному стану теоретичних та експериментальних досліджень у галузі фізики
Видання призначене для науковців, викладачів, аспірантів та студентів фізичних спеціальностей вищих навчальних закладів та наукових установ

Затверджено до друку рішенням Вченої ради Харківського національного університету імені В.Н.Каразіна (протокол №7 від 01 липня 2015 р.)

Редакційна колегія:
Головний редактор
Вовк Р.В. - доктор фіз. - мат. наук, професор , ХНУ імені В.Н.Каразіна, Україна
Заступник головного редактора
Пойда В.П. - доктор тех. наук, професор, ХНУ імені В.Н.Каразіна, Україна
Відповідальний секретар
Криловський В.С. - канд. фіз. - мат. наук, доцент, ХНУ імені В.Н.Каразіна, Україна
Редакційна колегія
Агеєв Л.О. - доктор фіз. - мат. наук, професор, ХНУ імені В.Н.Каразіна, Україна
Андерс О.Г. - доктор фіз. - мат. наук, професор, ХНУ імені В.Н.Каразіна, Україна
Бойко Ю.І. - доктор фіз. - мат. наук, професор, ХНУ імені В.Н.Каразіна, Україна
Гуревич Ю.Г. - доктор фіз. - мат. наук, професор, Дослідницький центр, Мексика
Зиман З.З. - доктор фіз. - мат. наук, професор, ХНУ імені В.Н.Каразіна, Україна
Кагановський Ю.С. - доктор фіз. - мат. наук, професор, Бар - Іланський університет, Ізраїль
Камзін О.С. - доктор фіз. - мат. наук, професор, ФТІ імені Іоффе, Росія
Кунцевич С.П. - доктор фіз. - мат. наук, професор, ХНУ імені В.Н.Каразіна, Україна
Пархоменко О.О. - доктор фіз. - мат. наук, професор, ННЦ ХФТИ НАНУ, Україна
Портной М.Ю. - доктор фізики, професор, університет Ексетеру, Великобританія
Рошко С.М. - доктор фізики, професор, Лондонський центр нанотехнологій, Великобританія
Хронеос Олександр - доктор фізики, професор, Империал коледж, Великобританія
Фегер Олександр - доктор фіз. - мат. наук, професор, інститут фізики університету імені Шафарика, Кошице, Словакія
Федоров П.М. - доктор фіз. - мат. наук, професор, ХНУ імені В.Н.Каразіна, Україна
Шехтер Роберт - доктор фіз. - мат. наук, професор, Гетеборгський університет, Швеція
Шкловський В.А. - доктор фіз. - мат. наук, професор, ХНУ імені В.Н.Каразіна, Україна
Шкуратов Ю.Г. - член-кор. НАН України, доктор фіз. - мат. наук, професор,
ХНУ імені В.Н.Каразіна, Україна
Ямпольський В.О. - член-кор. НАН України, доктор фіз. - мат. наук, професор, ХНУ
імені В.Н.Каразіна, Україна

Адреса редакції:
Україна, 61022, Харків, майдан Свободи, 4, Харківський національний університет імені В.Н. Каразіна, фізичний факультет, 057-707-53-83, ruslan.v.vovk@univer.kharkov.ua
Статті пройшли внутрішнє та зовнішнє рецензування.
Свідоцтво про державну реєстрацію КВ №11825-696 ПР від 04.10.2006

© Харківський національний університет
імені В.Н. Каразіна, оформлення, 2015

UDC 530.1/539.8

Bulletin contains articles on the current state of theoretical and experimental research in the field of physics.
The publication is intended for researchers, teachers and students of physical specialties of higher education and research institutions.

Approved for publication by the decision of the Academic Council of Kharkiv Karazin National University. (Minutes №7 dated July 01, 2015 p.)

Editorial Board
Editor-in-Chief -
Vovk R.V. - Dr. Sci., Prof., V.N. Karazin Kharkiv National University, Ukraine
Deputy Editor-in-Chief -
PoidaV.P. - Dr. Sci., Prof., V.N. Karazin Kharkiv National University, Ukraine
Assistant Editor -
Krylovskiy V.S. – Ph.D., Assoc. Prof. , V.N. Karazin Kharkiv National University, Ukraine
Ageev L.O. - Dr. Sci., Prof., V.N. Karazin Kharkiv National University, Ukraine
Anders O.G. - Dr. Sci., Prof., V.N. Karazin Kharkiv National University, Ukraine
Boiko Yu.I. - Dr. Sci., Prof., V.N. Karazin Kharkiv National University, Ukraine
Gurevich Yu.G. - Dr. Sci., Prof., Center for Research and Advanced, Mexico
Zyman Z.Z. - Dr. Sci., Prof., V.N. Karazin Kharkiv National University, Ukraine
Kaganovskiy Yu.S. - Dr. Sci., Prof., Bar - Ilan University, Israel
Kamzin O.S. - Dr. Sci., Prof., Ioffe Institute, Russia
Kuncevich S.P. - Dr. Sci., Prof., V.N. Karazin Kharkiv National University, Ukraine
Parhomenko O.O. - Dr. Sci., Prof., NSC "Kharkov Institute of Physics & Technology", Ukraine
Portnoi M. Yu. - Dr. Sci., Prof., University of Exeter, UK
Rozhko S.M. - Dr. Sci., Prof., London Centre for Nanotechnology, UK
Chroneos A. - Dr. Sci., Prof., Imperial Colledge, UK
Feher A. - Dr. Sci., Prof., , Pavol Jozef Šafárik University in Košice, Kosice, Slovakia
Fedorov P.M. - Dr. Sci., Prof., V.N. Karazin Kharkiv National University, Ukraine
Shekhter R.I. - Dr. Sci., Prof., University of Goteborg, Sweden
Shklovskij V. A. - Dr. Sci., Prof., V.N. Karazin Kharkiv National University, Ukraine
Shkuratov J.G.- Corresponding Member of the NAS of Ukraine, Dr. Sci., Prof., V.N. Karazin Kharkiv National University, Ukraine
Yampol'skii V. A. - Corresponding Member of the NAS of Ukraine, Dr. Sci., Prof., V.N. Karazin Kharkiv National University, Ukraine

Editorial address:
Svobody Sq. 4, 61022, Kharkiv, Ukraine, V.N. Karazin Kharkiv National University, Department of Physics, 057-707-53-83,ruslan.v.vovk@univer.kharkov.ua
All articles reviewed.
Certificate of state registration of CT number 11825-696 PR on 04/10/2006

© V.N. Karazin Kharkiv National University,
design, 2015

Content

Вісник ХНУ, № 1158, серія «Фізика», вип. 22, 2015. с. 6-9

УДК 535.4
PACS: 42. 25. Dd.42.25Hz

Researsh of altitude of potential barrier at the metal-vacuum interface by the diffraction method

A.V. Bezuglyi, E.S.Orel, A. M. Petchenko

O.M. Beketov National University of Urban Economy in Kharkiv,
Ukraine, 61002, Kharkov, Revolyutsii street, 12
physics@kname.edu.ua

The paper considers the problem of diffraction at normal incidence of a monochromatic beam of photons on a grating of thin metal strips. Quantum-mechanical approach is used to describe the phenomenon of diffraction of particles. Based on the elastic interaction of photons with electrons, that is in the strip and carries a one-dimensional movement in the potential pit with barriers of finite height, relations for discrete values of angles, at which the diffraction peaks should be observed, were obtained in the first approximation. The equations obtained in this work are the same in the case of small angles of diffraction as the known in the scientific literature expressions that determine the position of the diffraction peaks in the case of diffraction of light at a diffraction grating surface. The relation to determine the height of the potential barrier at the metal – vacuum interface was obtained.

Keywords: electrons, photons, diffraction, beam, potential barer, potential pit, discrete spectrum, elastic interaction, diffraction grating.

В роботі розглянута задача дифракції при нормальному падінні монохроматичного пучка фотонів на гратку нескінченно тонких металевих стрічок. При розв’язанні задачі використано квантово-механічний підхід до описання явища дифракції частинок. Виходячи із уявлення про пружну взаємодію фотона з електроном, що знаходиться в стрічці, і здійснює одновимірний рух в потенціальній ямі з потенціальними бар’єрами обмеженої висоти, отримано в першому наближенні співвідношення для дискретних значень кутів, під якими повинні спостерігатися дифракційні максимуми. Показано, що рівняння, отримані в роботі, збігаються у випадку малих значень кутів дифракції з відомими в науковій літературі виразами, що визначають розташування дифракційних максимумів у випадку дифракції світла на дифракційній гратці. Отримано співвідношення для визначення висоти потенціального бар`єра на межі метал-вакуум.

Ключові слова: електрон, фотони, дифракція, пучок, потенціальний бар’єр, потенціальна яма, дискретний спектр, пружна взаємодія, дифракційна гратка.

В работе рассмотрена задача дифракции при нормальном падении монохроматического пучка фотонов на решетку бесконечно тонких металлических лент. Используется квантово-механический подход к описанию явления дифракции частиц. Исходя из представления об упругом взаимодействии фотона с электроном, находящимся в ленте и осуществляющем одномерное движение в потенциалрной яме с барьерами конечной высоты, получены в первом приближении соотношения для дискретных значений углов, под которыми должны наблюдаться дифракционные максимумы. Уравнения полученные в работе, совпадают в случае малых углов дифракции с известными в научной литературе выражениями, определяющими положения дифракционных максимумов в случае дифракции света на дифракционной решетке. Получено соотношение для определения высоты потенциального барьера на границе раздела металл - вакуум.

Ключевые слова: Электрон, фотоны, дифракция, пучок, потенциальный барьер, потенциальная яма, дискретный спектр, упругое взаимодействие, дифракционная решетка.

Introduction

The article [1] offers a quantum approach to describe the diffraction of light from two slits and from periodic system of parallel slits on metal screen where they form a diffracting screen. This approach is based on the following model. Metal tape is compared to infinitely deep potential pit, slits are infinitely high barrier. Herewith, diffraction pattern composed of interleaving of minimum and maximum of illumination intensity is explained as a result of elastic interaction of photons with electrons. These electrons in strips are in the state of free movement.

This work offers a model close to reality where strips are compared to finite depth pit and slits are compared to finite height barriers.

Statement and solution of the problem

Supposing photon flux falls normally to the screen plane from the side of negative values X located in the YOZ plane with Y-axis slit (Fig.1). When photons pass through slits they interact with electrons of material, suppose photon deflection from rectilinear propagation is observed as a result of this interaction.

Further the following model is taken as a base. Quantum-mechanical model of grating formed by infinite

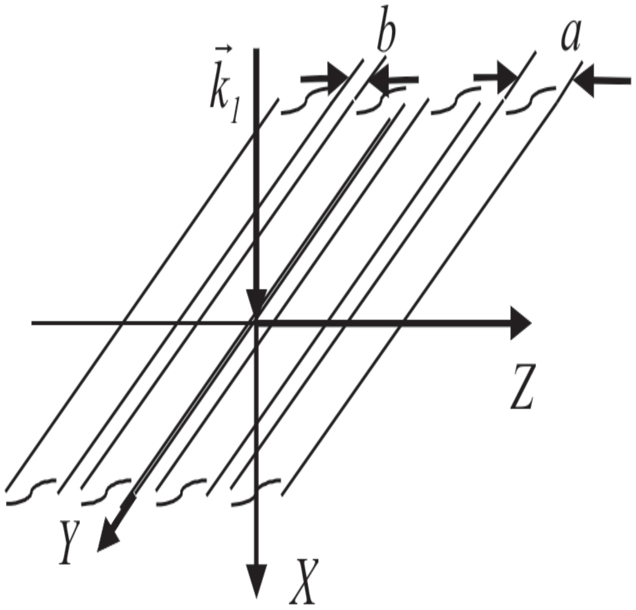

Fig. 1. Photon falling on the screen with slits.

sequence of slits (Fig.2) may be a periodic sequence of potential barriers (pits) where pits correspond to non-transparent opaque areas and barriers correspond to slits

Here we will base on the following assumptions:

1) photon passing through the slits interacts with electron;

2) electron is in the state of free movement in one-dimensional potential pit with walls of finite height;

3) collision of photon with electron occurs according to the perfectly elastic collision law;

4) width of slit *b* is small compared to the width of the metal strip *a*.

It is a complicated task to produce mathematical expression of intensity distribution in the interference pattern. Here we will limit ourselves to dimension that determines the positions of the maximums.

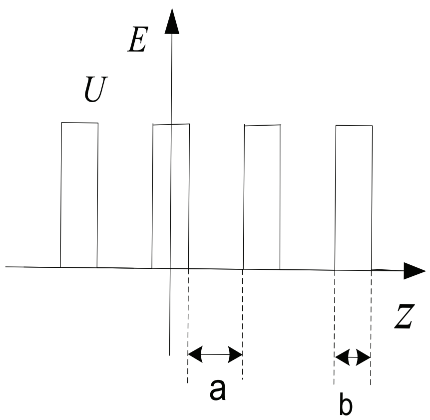

Fig. 2. Quantum-mechanical model of grating.

According to the law of conservation of impulse

$$\vec{p}_1 + \vec{k}_1 = \vec{p}_2 + \vec{k}_2, \qquad (1)$$

where $\vec{k}_1$, $\vec{k}_2$ are photon impulses before and after collision, $\vec{p}_1$, $\vec{p}_2$ are impulses of electrons in metal strip before and after collision. Diagram of impulses is shown in Figure 3.

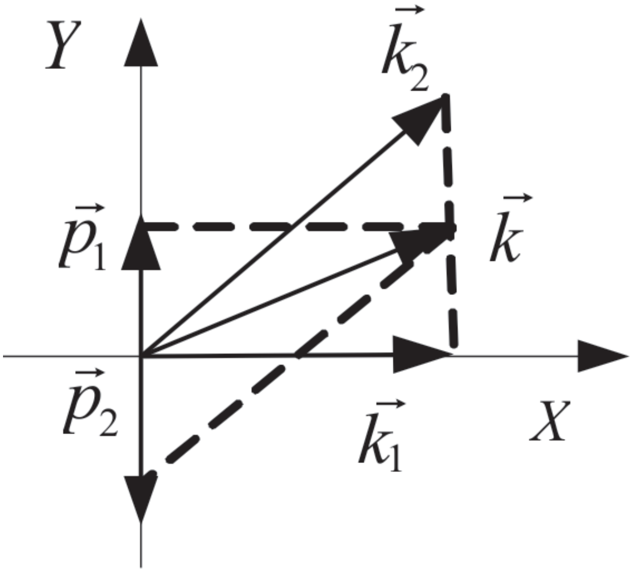

Fig. 3. Diagram of impulses of photons and electrons.

Since electron is in a plate-dimensional motion in one-dimensional potential pit, it can not have X, an impulse component. Consequently, in the projections on the axis we will get

$$k_1 = k_2 \cos\vartheta, \qquad (2)$$

$$p_1 = -p_2 + k_2 \sin\vartheta.$$

Rewrite the system of equations (2) as following

$$0 = -k_1 + k_2 \cos\vartheta,$$

$$p_2 = -p_1 + k_2 \sin\vartheta.$$

After squaring and adding we will get

$$p_2^2 = k_1^2 + k_2^2 + 2k_1k_2\cos\vartheta +$$

$$+ p_1^2 - 2p_1k_2\sin\vartheta. \qquad (3)$$

According to the energy conservation law

$$E_{p1} + E_{k1} = E_{p2} + E_{k2}, \qquad (4)$$

Where E_{k1}, E_{k2} is total energy of photon before and after collision, E_{p1}, E_{p2} is total energy of electron before and after collision. $E_{p1} = \hbar\varpi_1$, $E_{p2} = \hbar\varpi_2$,

$E_{p1} = \sqrt{m^2c^4 + p_1^2c^2}$, $E_{p2} = \sqrt{m^2c^4 + p_2^2c^2}$, m - stands for mass of electron at rest.

Using binomial theorem, we get the following approximate expressions to calculate energy of photon and electron of metal strip:

$$\mathrm{E}_{k1} = mc^2\left(1 + \frac{k_1^2}{m^2c^2}\right)^{\frac{1}{2}} \approx mc^2\left(1 + \frac{k_1^2}{2m^2c^2}\right)$$

$$E_{k2} \cong mc^2\left(1 + \frac{k_2^2}{2m^2c^2}\right), \qquad (5)$$

$$E_{p1} \cong mc^2\left(1 + \frac{p_1^2}{2m^2c^2}\right),\ E_{p2} \cong mc^2\left(1 + \frac{p_2^2}{2m^2c^2}\right)$$

.

Rewrite the energy conservation law (4) as following:

$$\begin{aligned} &mc^2\left(1 + \frac{k_1^2}{m^2c^2}\right)^{\frac{1}{2}} + mc^2\left(1 + \frac{p_1^2}{2m^2c^2}\right) = \\ &= mc^2\left(1 + \frac{k_2^2}{2m^2c^2}\right) + mc^2\left(1 + \frac{p_2^2}{2m^2c^2}\right) \end{aligned}, \qquad (6)$$

After minor changes in the expression (6) we will get

$$\begin{aligned} &\mathrm{m}^2c^4 + p_2^2c^2 = m^2c^4\left(1 + \frac{k_1}{2m^2c^2}\right)^2 + \\ &+ m^2c^4\left(1 + \frac{p_1^2}{2m^2c^2}\right)^2 + m^2c^4\left(1 + \frac{k_2^2}{2m^2c^2}\right)^2 + \\ &+ 2m^2c^4\left(1 + \frac{k_1^2}{2m^2c^2}\right)\left(1 + \frac{p_1^2}{2m^2c^2}\right) - \\ &- 2m^2c^4\left(1 + \frac{k_1^2}{2m^2c^2}\right)\left(1 + \frac{k_2^2}{2m^2c^2}\right) - \\ &- 2\mathrm{m}^2c^4\left(1 + \frac{p_1^2}{2m^2c^2}\right)\left(1 + \frac{k_2^2}{2m^2c^2}\right) \end{aligned}. \qquad (7)$$

Ignoring second-order term in the expression (7) we receive

$$p_2^2 = p_1^2 + k_1^2 - k_2^2\ . \qquad (8)$$

Equating right parts of (3) and (8) we will get

$$-2k_1k_2\cos\vartheta + 2p_1k_2\sin\vartheta = -2k_2^2\ . \qquad (9)$$

In the optical range the change of frequency of photon as a result of collisions with electrons (the Compton effect) is very small [3], therefore in the equation (9) can be assumed that $k_1 \approx k_2$ and get the relation between the initial value of the impulses of interacting particles and the photon scattering angle, a diffraction angle ϑ:

$$\frac{1 - \cos\vartheta}{\sin\vartheta} = \frac{\sin\vartheta}{1 + \cos\vartheta} = \frac{p_1}{k_1}. \qquad (10)$$

We now determine the eigenvalues impulses of the free-electron that are moving in a symmetric potential pit with a height of potential barriers U. The spectrum of impulses / momentum of electrons, which move in the potential wells is discrete [2], and thus the deflection angles of the photons (diffraction angles) when passing through a screen with slits will also be discrete. For a given task the eigenvalues of the wave numbers can not be obtained analytically. To determine them, the transcendental equation has been obtained [2]

$$ka = n\pi - 2\arcsin\frac{k\hbar}{\sqrt{2mU}},\ \ \mathrm{n} = 1,2,3,... \qquad (11)$$

where $k = \frac{\sqrt{2mE}}{\hbar}$, $\hbar = h/2\pi$ is the Planck constant.

It is obvious that the movement of electrons is localized in potential pits, beyond which they can not get out, which is consistent with the idea that the free electrons in the metal are free to move in the sample, but can not go beyond it. So when we have a periodic sequence of N stripes, energy levels corresponding to a single isolated pit will not be split.

Solution of equation (11) can be obtained by iteration method. We rewrite this equation in the form

$$k\,\hbar = \frac{\pi\,n\,\hbar}{a} - \frac{2\hbar}{a}\arcsin\frac{k\,\hbar}{\sqrt{2mU}}\ . \qquad (12)$$

The first term on the right-hand side of equation (11) determines the eigenvalues of the momentum for an infinitely deep potential pit. As shown by numerical analysis, results of which are shown in Table 1, it is a good starting (zero) approximation for calculating eigenvalues of impulses (and energy levels) of the finite depth pit U. Therefore, it is better to represent it in the following form

$$p_1 = p_0 - \frac{2\hbar}{a}\arcsin\frac{p_0}{\sqrt{2mU}}\ , \qquad (13)$$

where $p_0 = \frac{\pi\,n\,\hbar}{a}$, n = 1,2,3… .

This expression (13) shows the electron momentum in the first approximation in the pit depth U (obtained by iteration method). Equation (13) can be simplified. Assuming that in the equation $\frac{p_0}{\sqrt{2mU_0}} \ll 1$, we will get

$$p_1 = p_0 - \frac{2\hbar}{a}\frac{p_0}{\sqrt{2mU}}\ . \qquad (14)$$

Substituting (14) into (10) we obtain an equation of a diffraction grating

$$\frac{\sin\vartheta}{1+\cos\vartheta}=\frac{n\lambda}{2a}\left(1-\frac{\hbar\sqrt{2}}{a\sqrt{mU}}\right), \qquad (15)$$

determining the position of the maxima in the diffraction pattern, λ is the wavelength of the incident light. For small diffraction angles $\vartheta < 1$ and a deep well (pit) $U \to \infty$ we get the well-known equation of diffraction grating in the case of normal incidence of light [4],

$$a\sin\vartheta = n\lambda \qquad (16)$$

Table 1 shows the results of numerical calculations for pit depth U = 33 eV, and width a = 10^{-9} m. It also presents the results of comparison of the values of energy $E_{n\infty}$ and momentum p_∞ for the infinitely deep well with the values of energy E_n and momentum p_1 for the finite depth pit that were calculated by the formula (14) in the first approximation .

In the above table also shows the values of energy $E_n^{''}$ and momentum p_1* for the finite depth pit, calculated by formula (12) by finding successive approximations by Newton's method. There are 9 roots in a pit at a given height of the barrier. As the table shows, the energy eigenvalues differ little from $E_{n\infty}$ as well as p_∞ from p_1* and really are a good zero-order approximation for calculating eigenvalues of momentum for the finite depth pit. Comparing the energy eigenvalues $E_n^{''}$ with E_n (and accordingly p_1* with p) we can see that the error does not exceed 3.5%.

According to the definition arcsin equation (12) can be written as

$$\sin\frac{p_0-p_1}{2\hbar}a=\frac{p_0}{\sqrt{2mU}} . \qquad (17)$$

From equation (17) can determine the height of the potential barrier

$$U=\frac{p^2{}_0}{2m\sin^2\left[\frac{a}{2\hbar}\left(p_0-p_1\right)\right]} . \qquad (18)$$

Suppose that we know the diffraction angles ϑ from the diffraction pattern obtained as the result of light diffraction on two slits or a grating formed by the N slits. In this case, the magnitude of the impulse p_1 can be determined from equation (9)

$$p_1=k_1\frac{\sin\vartheta}{1+\cos\vartheta}=\frac{2\pi\hbar}{\lambda}\frac{\sin\vartheta}{1+\cos\vartheta} \qquad (19)$$

Conclusion

In the article the expression for calculating eigenvalues of the electron impulses in a potential well bounded by barriers of finite height has been obtained. Their estimation accuracy is given. An expression that defines the angle of diffraction, allowing finding the position of the maxima in the diffraction pattern has been obtained in the first approximation. The formula for the calculation of the potential barrier at the metal-vacuum interface has been derived.

1. Безуглый А.В. Радиотехника. 2006. Вып. 147. с. 65-68.
2. Ландау Л.Д., Лифшиц Е.М. Теоретическая физика. М., 1963, т. 3. с. 61-65, 87-89.
3. Борн М., Атомная физика, М.,1970 с.135.
4. Борн М., Вольф Э. Основы оптики. М., Наука 1973. с.371.

Table 1

n	$E_{n\infty}$, eV	E''_n, eV	E_n, eV	p_∞, 10^{-5}kGm/s	p, 10^{-5} kGm/s	p^*_1,10^{-5}kGm /s	$(p-p_1)/p$,%	$(E''_n-E_n)/E''_n$, %
1	0.381	0.334	0.324	3.297	3.118	3.077	1.3	2
2	1.524	1.335	1.299	6.594	6.234	6.151	1.4	2.6
5	9.528	8.301	8.123	16.49	15.55	15.32	1.5	3
9	30.87	26.32	26.32	29.67	27.66	27.11	1.9	3.5

Вісник ХНУ, № 1158, серія «Фізика», вип. 22, 2015. с. 10-12

УДК 523.4
PACS: 96.12.Kz

Modeling of the spectral properties of the dwarf planet Makemake

T. A. Hromakina, L. V. Starukhina, I. N. Belskaya, V. V. Korokhin

Institute of Astronomy of V.N. Karazin Kharkiv National University

We present the results of spectral modeling for dwarf planet Makemake in the visible and near infrared ranges. The spectral modeling of surface properties suggests the presence of both large and small (~1 μm) grains of methane ice on the top surface, and possible presence of ethane ice and other long-chain hydrocarbons.

Keywords: small Solar system bodies, planetary surfaces, spectral modeling.

В работе представлены результаты моделирования спектра карликовой планеты Макемаке в видимой и ближней инфракрасной областях. Предложена наиболее вероятная модель поверхности Макемаке, которая предполагает наличие как крупных, так и мелких (~1 микрон) частиц метанового льда в поверхностном слое, а также возможное наличие льда этана и более сложных гидрокарбонатов в качестве примесей.

Ключевые слова: малые тела Солнечной системы, планетные поверхности, моделирование спектра.

У роботі наведені результати моделювання спектра карликової планети Макемаке у видимому та ближньому інфрачервоному діапазоні. Запропонована найбільш імовірна модель поверхні Макемаке, яка передбачає наявність як великих, так і малих за розмірами (~1 мікрон) часток метанового льоду на поверхні, а також можливу наявність льоду етану та більш складних гідрокарбонатів у якості домішок.

Ключові слова: малі тіла Сонячної системи, планетні поверхні, моделювання спектра.

Introduction

The dwarf planet (136472) Makemake is one of the largest and brightest trans-Neptunian objects (TNOs). The first hints of its surface composition were obtained shortly after the discovery in 2005; they were based on spectral observations in the 0.3-2.5 μm spectral region by Brown et al. [3] and Licandro et al. [13]. Spectral observations have revealed the presence of methane absorption bands. Moreover, Makemake's spectra show the strongest absorption bands of methane ice compared to other methane-rich Solar system objects, namely (134340) Pluto, (136199) Eris, and Neptune's satellite Triton [3, 13].

Later Makemake was repeatedly observed in the visible and near-IR spectral region in search for possible surface heterogeneity [5, 14, 17]. Available for ground-based observations, this spectral range is particularly useful because it contains absorptions bands of silicate minerals, ices and hydrocarbons [1]. All spectra of Makemake are compatible with each other. Some discrepancies between the continuum slope and the depth of absorption bands are due rather to the use of different solar analog stars than due to real changes over surface. However, as stated in [14], the color variation over the surface of Makemake is also not excluded.

Spectral modeling [3, 5, 13] suggests that the dominant substance on the surface of Makemake is methane and not nitrogen as it is for Pluto and Eris. No nitrogen absorption lines were detected. But close examination of the methane ice bands revealed that they are blue shifted by ~4 Å [14, 17]. The authors argue that such shift is related to the presence of a small (up to a few percents) amount of nitrogen on the surface. As for methane ice, spectral modeling performed by [3, 13, 17] in the visible and near-IR spectral ranges using Hapke model [9] implies the presence of large grains at least one centimeter in size. By applying both Hapke and so-called slab model, the authors [7] suggested that methane presented on Makemake's surface in the form of low-porosity ice slab formed by sintered micron-sized grains.

The red spectral slope in the visible range measured for Makemake is rather typical of outer Solar system bodies. This is usually explained by the presence of tholins that could be formed by solar irradiation of simple organic compounds such as methane or ethane [3]. The presence of ethane and more complex hydrocarbons as natural products of methane irradiation on the Makemake's surface was also suggested [3, 5].

The presence of very large particles or slab on the Makemake's surface looks rather unrealistic, since the typical estimate of the methane grain size on the other dwarf planets is about 100 μm or less (see., e. g, [19, 20]). Furthermore, according to recent polarimetric observations of Makemake [2], its surface should be covered by a thin fluffy layer of submicron grains. In this paper we use spectral modeling based on other approach to analyze possible texture of the Makemake's surface.

Spectral modeling

We have analyzed spectral data published by Brown et al. [3] and Licandro et al. [3 13], and kindly provided by the authors. The spectra were normalized at the wavelength λ = 0.55 μm to the value of the visible albedo $p_v = 0.8$ [4, 15]. Both spectra are rather similar with only minor differences in the absorption bands shape at 1.4 and 1.95 μm. For the modeling we used spectrum from [3] in the 1.0-2.5 μm wavelength range which has the higher signal-to-noise ratio.

In order to model the spectrum of Makemake we used the model of Shkuratov et al. [21, 23]. One of the advantages of this model is that it uses directly the optical constants of the surface material (real and imaginary parts of the complex refractive index). Another advantage is its invertibility, i.e. possibility to calculate both the albedo of the surface starting from its optical constants and the absorption coefficient of the surface material starting from the albedo, if the value of the real part of complex refractive index is preliminary estimated. The mathematical concept of the model is described in [21, 23].

In our modeling we used optical constants of methane, ethane, tholins, acetylene, and other hydrocarbons [6, 8, 10, 11, 12, 18]. It should be noted that optical laboratory spectra depend on conditions under which they were obtained, in particular, on the temperature. Therefore, we used optical constants that were obtained at the temperatures corresponding to those on Makemake surface (~40 K).

We also used modification of the model [21, 23] for submicron particles (~λ), because the presence of such small grains results in change of both absorption and refraction indices. The modification is also described in [21, 23].

The best agreement between the observed reflection spectrum and the model was achieved by minimizing the chi-square value:

$$\chi^2 = \sum_{i=1}^{n} \frac{(O_i - M_i)^2}{M_i},$$

where O_i are the points of the measured spectrum, M_i are the points of model spectrum, n is the number of points. For fitting procedure we used the astronomical software “xIRIS Framework” developed by V. V. Korokhin, E. V. Shalygin., and Yu. I. Velikodsky (for more information see http://www.astron.kharkov.ua/dslpp/iris/xiris.html).

Assuming that the Makemake’s surface is covered mostly by methane ice [3, 13, 17], at the beginning we used only laboratory spectrum of methane obtained at 40 K [8]. Varying methane grain size from 10^{-5} to 1 cm we have found the best fit for the grain size of 0.3-0.4 mm though the coincidence is not perfect (Fig. 1).

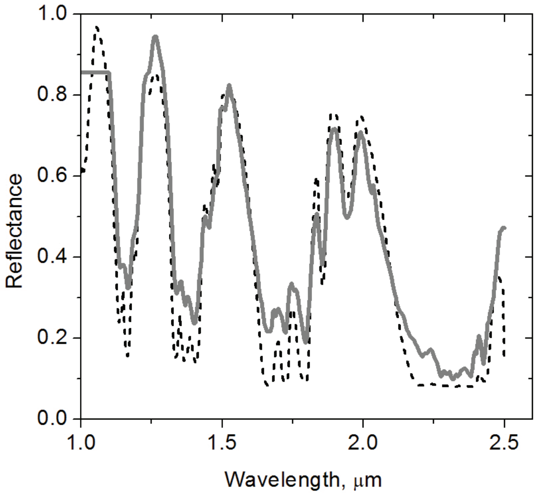

Fig. 1. Comparison between the measured spectrum of Makemake (dashed black line) and the spectral model that uses large (~0.35 mm) methane ice grains (solid gray line).

Polarimetry results for Makemake [2] indicate presence of micron-size particles on its surface. Taking this into account, as the next step of our modeling we used a two-component surface model, that includes large (d > λ) and small (d ~ λ) methane ice particles.

The assumption about the presence of small methane ice particles on the surface significantly improved the agreement between the model and the observed spectra. The minimum of χ^2 value was achieved at 70:30 mix of large (~ 0.3 cm) and small (~1 μm) methane ice grains, respectively (Fig. 2). Note that two free parameters of our modeling (the concentration and grain size) cannot be varied independently, so the determination of both free parameters is difficult. Very similar model spectra can be obtained either with very large grain size and high concentration of

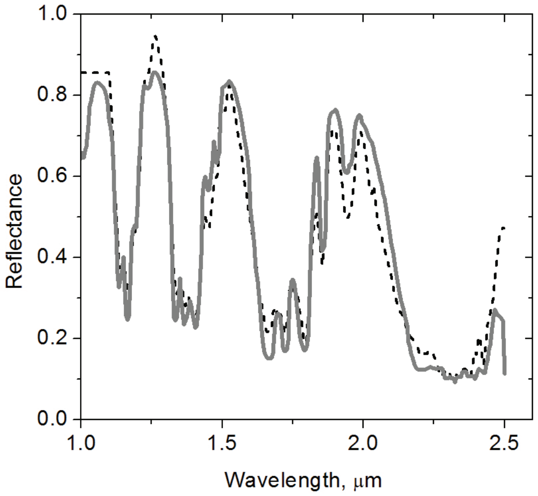

Fig. 2. Comparison between the measured spectrum of Makemake (dashed black line) and model that uses large (~0.3 mm) and small (~1 μm) methane ice in a 70:30 mix (solid gray line).

micron-sized component or with smaller grain size and low concentration of micron-sized component.

To improve the agreement between the measured and calculated spectra we used different admixtures found by spectral modeling on the surfaces of dwarf planets and methane-rich Solar system bodies, and theoretically possible on the surface of Makemake. We used reflectance spectra of tholins, ethane, acetylene, and other hydrocarbons. Spectral modeling of methane ice mixed with various inclusions has shown that an addition of ~30 μm ethane ice grains in concentration of about 20% reduces the difference between the observed and calculated spectra of Makemake at some wavelengths. It also reduces total residual in comparison with pure methane ice spectrum (Fig. 3). The presence of tholins is also not ruled out. The influence of other organic materials on the model is insignificant.

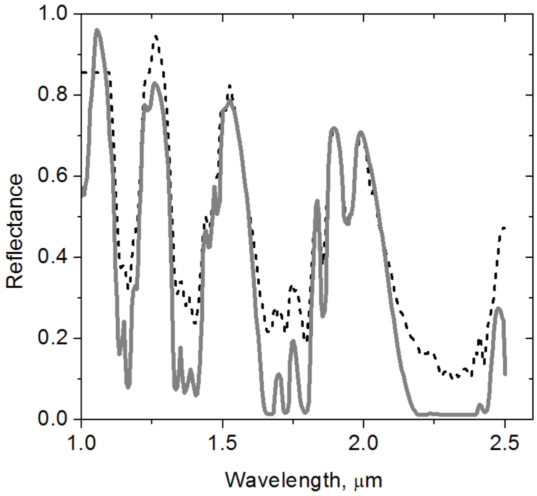

Fig. 3. Comparison between the measured spectrum of Makemake (dashed black line) and the model that uses large methane ice grains (~0.3 mm), small methane ice grains (~1 μm), and ethane ice (~30 μm) in a 60:20:20 mix (solid gray line).

Conclusion

We present the results of spectral modeling for dwarf planet Makemake. We used a slightly different approach as compared to other researchers in order to analyze surface properties of Makemake and to check the plausibility of very coarse methane ice grains on the surface of Makemake suggested before [3, 13, 17]. According to our results, the most likely model of the Makemake's surface suggests the presence of large methane ice particles of a size ~0.3 cm (~60%) coated with fine particles of a size ~1 μm (~20%), as well as the possible presence of ethane ice (~20%). The assumption about the presence of small particles covering large particles enables us to reconcile the results of spectral and polarimetric observational data.

1. M. A. Barucci. Composition and Surface Properties of Transneptunian Objects and Centaurs. The Solar System Beyond Neptune, University of Arizona Press (2008), p. 143.
2. I. N. Belskaya et al. A&A, 479, 265 (2008).
3. M. E. Brown et al. The Astronomical Journal, 133, 284 (2007).
4. M. E. Brown et al. The Astrophysical Journal Letters, 767, L7, (2013).
5. M. E. Brown et al. The Astronomical Journal, 149, 105 (2015).
6. R. N. Clark et al. Journal of Geophysical Research, 114, E03001 (2009).
7. J. Eluszkiewicz et al. Journal of Geophysical Research, 122, E06003 (2007).
8. W.M. Grundy et al. Icarus, 155, 486 (2001).
9. B. Hapke and E. Wells. Journal of Geophysical Research, 86, 3039 (1981).
10. R. L. Hudson et al. Icarus, 228, 276 (2014).
11. R. L. Hudson et al. Icarus, 243, 148 (2014).
12. B. N. Khare and K. Sagan. Icarus, 60, 127 (1984).
13. J. Licandro et al. A&A, 445, 35 (2006).
14. V. Lorenzi et al. A&A, 577, 86 (2015).
15. J. L. Ortiz et al. Nature, 491, 566 (2012).
16. F. Poulet et al. Icarus, 160, 313 (2002).
17. S.C Tegler et al. Icarus, 195, 844 (2008).
18. E. Quirico et al. Icarus, 127, 354 (1997).
19. D. L. Rabinowitz et al. The Astrophysical Journal, 639, 1238 (2006).
20. T. Sasaki et al. The Astrophysical Journal, 618, 57 (2005).
21. Yu. Shkuratov and L. Starukhina. Icarus, 137, 235 (1999).
22. B. Sicardy et al. Nature, 478, 493 (2011).
23. L.V. Starukhina, Yu. G. Shkuratov. Astron. Vestnik, 30, 4, 299 (1996).

Вісник ХНУ, № 1158, серія «Фізика», вип. 22, 2015. с. 13-17

PACS: 77.22.Ch, 81.05.Dz, 81.70.Jb.
УДК: 621.315.592.9

Wavelet analysis of composition microinhomogeneities of $Cd_{1-x}Zn_xTe$ crystals grown from melt

O.N. Chugai, S.L. Abashin, A.V. Gaidachuk, D.P. Zherebyatiev, I.V. Lunyov, A.A. Poluboiarov*, S.V. Sulima*

N.E. Zhukovsky Kharkiv National Aerospace University, Chkalova str., 17, Kharkiv, 61070, Ukraine
**Institute for Single Crystals of NAS of Ukraine, Lenin Ave., 60, Kharkiv, 61001, Ukraine*
chugai@xai.edu.ua

Linear dependencies of composition of $Cd_{1-x}Zn_xTe$ (x = 0.03 - 0.15) crystals grown from melt were measured along direction of its growth. Wavelet analysis shows that in these dependences for Zn mole fraction corresponding to different sections there are several harmonic components with spatial period about units – tens micrometers. Anisotropy of low-frequency dielectric properties on crystals where specified direction is physically marked out was revealed. Peculiarities of crystal composition and properties are explained with self-oscillating processes at their growth.

Keywords: $A^{II}B^{VI}$ crystals, dielectric permittivity, semiconductors solid solutions, composition inhomogeneities, wavelet analysis.

Виміряні лінійні залежності складу вирощених з розплаву кристалів $Cd_{1-x}Zn_xTe$ (x = 0.03 - 0.15) у напрямку їхнього росту. Вейвлет-аналіз показав, що в цих залежностях для мольної частки Zn, що відповідає різним ділянкам, є кілька гармонічних складових з просторовим періодом порядку одиниць – десятків мікрометрів. Виявлена анізотропія низькочастотних діелектричних властивостей кристалів, при якій фізично виділеним є зазначений напрямок. Особливості складу і властивостей кристалів пояснені автоколивальними процесами при їх рості.

Ключові слова: кристали $A^{II}B^{VI}$, діелектрична проникність, тверді розчини напівпровідників, неоднорідності складу, вейвлет-аналіз.

Измерены линейные зависимости состава выращенных из расплава кристаллов $Cd_{1-x}Zn_xTe$ (x = 0.03 - 0.15) в направлении их роста. Вейвлет-анализ показал, что в этих зависимостях для мольной доли Zn, соответствующих разным участкам, имеются несколько гармонических составляющих с пространственным периодом порядка единиц - десятков микрометров. Обнаружена анизотропия низкочастотных диэлектрических свойств кристаллов, при которой физически выделенным является указанное направление. Особенности состава и свойств кристаллов объяснены автоколебательными процессами при их росте.

Ключевые слова: кристаллы $A^{II}B^{VI}$, диэлектрическая проницаемость, твердые растворы полупроводников, неоднородность состава, вейвлет-анализ.

Introduction

It is well known that a characteristic feature of solid solution semiconductors is a heterogeneous composition that significantly affects their electrical and optical properties. Moreover, the heterogeneity of composition is determined not only by statistical distribution of atoms over the lattice sites, but also by the conditions of solutions growth. In recent decades interest in the study of the effect of growth conditions on the specified semiconductor solutions composition feature has sharply increased. This is due to the possibility of spontaneous modulation (see. Eg. [1-2]) or in other words the superlattice ordering [3] of their composition. Notice that solid solutions investigated in mentioned and other studies differ in composition one from another, but represent as thin layers with thickness of several μm. The particular role of the surface simplifies composition self-structuring in such layers in comparison with the bulk solid solutions with the same components content [4]. In work [5] we first reported on the observation of self-organization of the composition in $Cd_{1-x}Zn_xTe$ (x = 0.05 - 0.20) bulk crystals grown from the melt. The aim of this work consists in a detailed study of these solutions heterogeneity. We notice that these solutions are one of the most promising materials for uncooled gamma-ray detectors [6]. That is why the vast majority of studies on their composition spatial distribution are closely linked to the achievement of physical properties which are important for this application. For example, in work [7] the composition distribution in $Cd_{1-x}Zn_xTe$ crystalline ingot has been investigated in connection with the uniformity of optical and electrical properties. In work [8] the correlation of Zn content with electrical resistivity of crystals doped with Se have studied. Also we should notice, solid solutions of cadmium – zinc telluride are still used as a substrates for the $Hg_{1-x}Cd_xTe$ layers in optoelectronic devices [9].

Method of experiment

Investigated crystals were grown from melt under high pressure of argon. Crystal wafers oriented with its plane parallel to the axis of the ingot were cut from it. One of these wafers after surface mechanical lapping is shown in Fig. 1a. The numbers I, II and III mark the position of linear sections along which the crystals composition was measured by energy dispersive electron microscope РЭМ – 106. Sections were oriented parallel to the ingot axis (Z-axis in the Figure 1a inset). Their length was 50 μm. Measurements were performed in the region of the spot 1 μm diameter with pitch of the same magnitude. Their relative error depends on the content of the solid solution components and in case of Zn is 20%. Before these measurements wafer surface had not only lapped but also was mechanically polished and chemically etched to remove affected surface layer. The same operations were used in production of rectangular samples from the wafers (7x6x5 mm) for measuring real and imaginary parts of dielectric permittivity of crystals at low frequencies. Sample planes were oriented perpendicular to the axes X, Y and Z (see Figure 1a inset). Electrical contacts to planes were created by coating with conducting lacquer TLC. Condenser-type method with partial filling of the space between plane capacitor plates with samples was used for measuring ε' and ε''.

In our studies of $Cd_{1-x}Zn_xTe$ crystal composition microinhomogeneities we paid special attention to changing in the mole fraction of Zn (i.e. x) along with the coordinate since this value determines crystal band gap. Fig. 2a shows the dependence of x coordinate for the section I (see. Fig. 1a), and Fig. 2b – the same dependence, but after the wavelet analysis. As is well known [10, 11], this analysis allows us to solve a wide range of experimental data processing tasks, including tasks of solid state physics (see. Eg. [12]). In our work, wavelet analysis was applied to filter mentioned dependence, i.e. $x(\ell)$, assimilated to "signal structure". Pursued goal was not only in detecting frequency of signal, but also in ascertainment of other its features. It was taken into account that the studied data characterize transient process whose statistical properties are unknown. Therefore filtering operation which removes both fast (fluctuations) and slow (trend) components from the dependence $x(\ell)$ was applied. We should notice that these components can provide useful information, but to receive it indicated composition dependence had to be measured at other magnitudes of d.

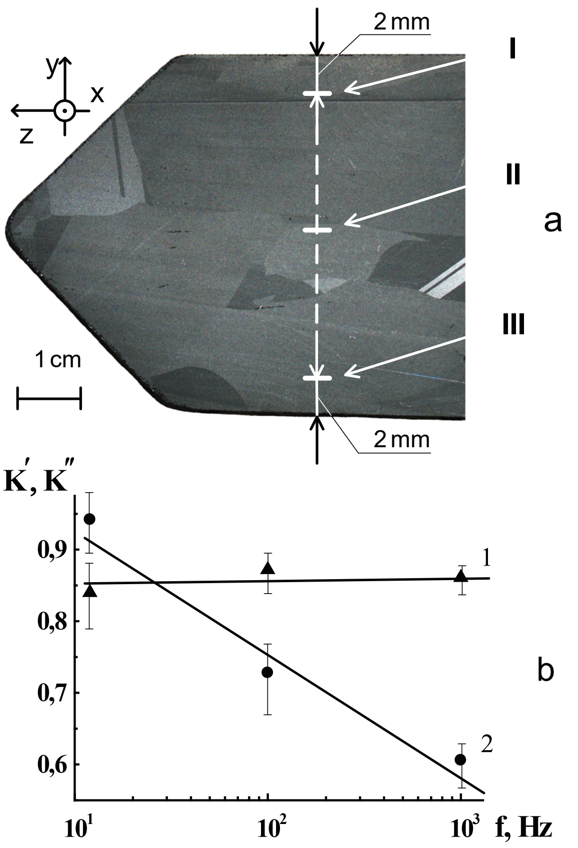

Fig. 1. Image of $Cd_{1-x}Zn_xTe$ wafer in reflected light (a) and anisotropy coefficients dependencies of dielectric permittivity by frequency. Data is averaged by all investigated samples (b).

Results and discussion

Wavelet analysis has carried out using application package MatLab [13]. Thereby for the initial coordinate dependence x represented as a sequence $x_n = x(nd)$, $n = 0,1...N-1$, $(N = 50)$ direct discrete wavelet transform

$$W(k_i,\ell_j) = a_i^{-1/2}\sum_{n=0}^{N-1} x_n \psi^*\left(\frac{nd-\ell_j}{a_i}\right)$$

has been carried out, where $W(k_i,\ell_j)$ is a value of wavelet coefficient for the wave number $k_i = \lambda_i^{-1}$ (λ_i – spatial period) and coordinate ℓ_j, ψ is a basic function of the wavelet transform, $*$ symbol corresponds to the complex conjugation, a_i is a parameter determined by the observation scale of investigated dependence in the $k-$ space, but not directly related to k_i. We should notice that the selection of specified function is one of the main difficulties of the wavelet signal filtering, which characteristics are insufficiently known. As the result, the knowledge of these characteristics would allow optimizing selection of the basic function using one or another criteria. However, in our studies, as noticed above, it was only

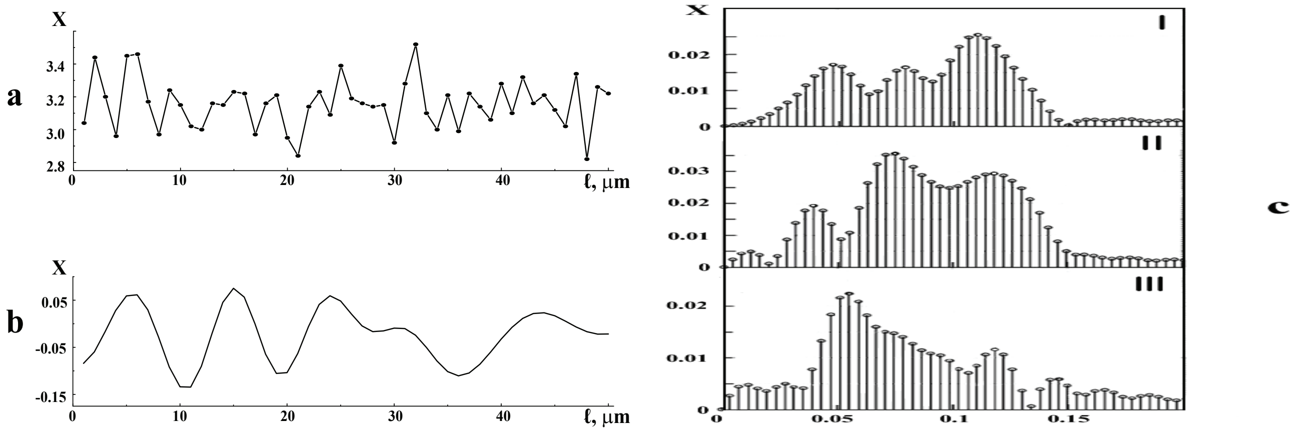

Fig. 2. Initial coordinate dependence of Zn mole fraction $x(\ell)$ in crystals (a) and result of its wavelet analysis (b); c – result of $x(\ell)$ dependence Fourier transform for wafer sections marked with Roman figures; numbers in parentheses are spatial periods expressed in μm corresponding to the selected maximums of transformed dependence.

known that the "composition signal" $x(\ell)$ of $Cd_{1-x}Zn_xTe$ crystals is periodic. The initial selection of ψ function was determined by the presence of sharp peaks in this signal (see. Fig. 2a). So we used Daubechies and Symlet wavelet function (both biquadratic). Further analysis was based on reaching minimum of a quadratic loss function obtained after the inverse wavelet transform of the "composition signal" to the source signal. It is ascertained that almost in all cases the lowest values of this function provides Symlet wavelet. So further only results obtained with this wavelet are given.

At the beginning of the computational procedure source data vector has multiplied by a quadratic matrix of wavelet transform. Resulting wavelet coefficients were divided into approximate $app(K,j)$ and detail $\det(K,j)$ components whose number was twice less than in the original data vector. K and j indexes determine the scale of the weight conversion function and its position on the axis lengths, respectively. For separating wavelet coefficients applied function «dwt» of MatLab environment, which realizes the algorithm discrete wavelet transform proposed by Mallat, was used [14]. Specified data vector multiplication and division operations have performed multiple components to achieve the maximum level of "composition signal" expanding m. As a result we received a set of wavelet coefficients that were used for the inverse wavelet transform with their additional weighting

$$x(\ell)=\sum_{j=0}^{N-1}\alpha(K)app(K,j)\varphi_K(\ell)+$$

$$+\sum_{K=0}^{m}\sum_{j=1}^{N-1}\beta(\mathrm{K})\det(\mathrm{K},\mathrm{j})\Psi_{K,j}(\ell)$$

where $\psi_{K,j}(\ell)$ is a basic function designated above ψ and $\varphi_K(\ell)$ is the corresponding scaling function, $\alpha(K)$ and $\beta(K)$ are weight coefficients for corresponding expanding level K. Relation $x(\ell)$ obtained as a result of described procession for one of examined wafers surface sections, as mentioned above is shown in Fig. 2b.

Stated above assumption about the presence of periodic components in investigated dependence and the possibility of their extraction by using wavelet filtering confirm the data shown in Fig. 3. This figure contains two wavelet spectrograms [10], each of them represents coefficient $W(k_i,\ell_j)$ dependence of value ℓ and level of expanding K. Spectrograms have obtained for the primary and wavelet filtered dependence $x(\ell)$ for the section indicated I in Fig. 1a. Dark areas on spectrograms correspond to positive and light ones to negative values of $W(k_i,\ell_j)$. This coefficient limits are allocated with shades of gray. Comparing the figure parts one to another one can see that region for which $K = 1 - 7$ have become more homogeneous as a result of filtering. This region corresponds to a fluctuating change of "composition signal". However, remaining part of the spectrogram has not experienced any change. It is important that at this part light and dark areas alternate in certain directions which could indicate the presence of periodic changes in solid solution composition.

With the purpose of determining periodic components in dependencies $x(\ell)$ for different sections filtered ones have been subjected to a Fast Fourier Transform (FFT). Results of this transform for three sections at one of investigated wafers (see. Fig. 1a) are shown in Fig. 2c. It can be seen that each of sections is characterized by own composition distribution (i.e., x) in the k – space.

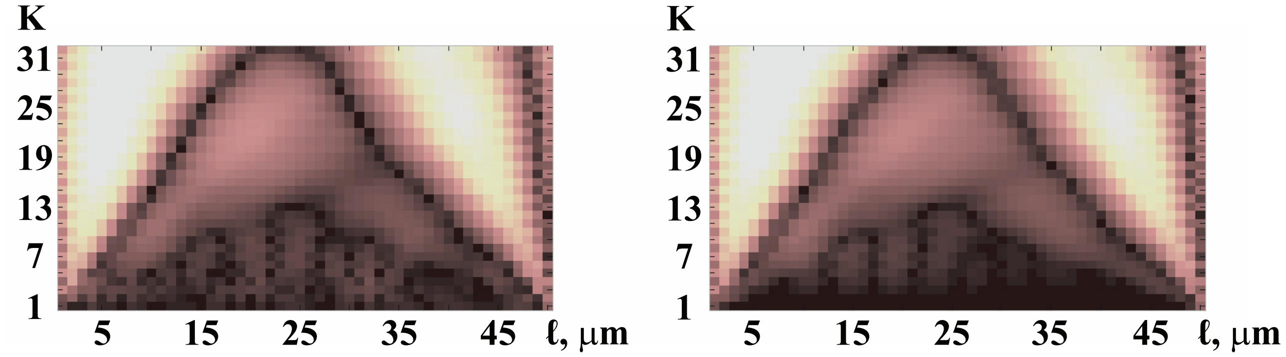

a

b

Fig. 3. $x(\ell)$ dependence wavelet spectrograms for one of crystal surface sections before (a) and after (b) wavelet filtration.

Moreover, such distributions have two or three dominant peaks (“composition harmonics”).

The fact that the amplitude of these harmonics is relatively small, taking into account Zn content measurement error given above is essentially important. It raises the question are whether detected periodic variations in the composition due to their smallness real. In our opinion, in favor of an affirmative answer to this question suggests not only described features of wavelet spectrograms (see. Fig. 3), but also the observation of “composition harmonics” on a number of sections oriented with its surface along growth direction on different samples. In view of it we should note that the analysis of other solid solution components content with method set above also showed the presence of harmonic components in changes of these magnitudes. And the greatest amplitudes of these harmonics for Cd and Te atoms were as a rule 2-3 times higher than for Zn atoms.

Among possible causes of observed self-organization composition in $Cd_{1-x}Zn_xTe$ crystals, obviously, should be excluded those are characteristic for the thin layers and are closely linked to their surface [4]. In addition, it is unlikely that mechanical stresses occurred due to heterogeneity play a key role in mentioned self-organization since the difference in lattice constants of ZnTe and CdTe crystals is about 6% [15]. Spinodal decomposition of the solid solution should also be excluded as another reason because according to [16], the critical temperature of such decomposition in $Cd_{1-x}Zn_xTe$ crystals with $x < 0.3$ is significantly below 300 K. Taking all this into account, we assume that the most likely cause of composition self-organization in investigated crystals are self-oscillating (auto-wave) processes in their growth. Similar processes were observed in growing crystals of different composition by various methods. Therefore it’s not surprising that different mechanisms of self-oscillations near the surface of the growing crystal are suggested. Although uncontrolled impurities can affect the growth of investigated crystals, but in our opinion auto-wave processes during crystallization none the less have a different nature. We mean transient convection currents in the melt, which basic conditions of occurrence are non-uniform temperature field and the large size of the growing crystal [18]. This assumption consists not only with considerable dimensions of investigated crystals (see. Fig. 1a), but also with observation of several “harmonics composition” on them (see. Fig. 2c). Mentioned work ascertained that in unsteady convection mode energy spectrum of temperature fluctuations has a discrete character. Convection currents distinction near different crystal zones seems to be natural. It can explain peculiarities of $x(\ell)$ dependencies in $k-$space for different ingot zones. Of course study of convection currents in specific thermal growth conditions of $Cd_{1-x}Zn_xTe$ crystals in connection with their composition peculiarities lays as separate problem.

Observation of dielectric properties anisotropy in crystals matches expressed assumption about their growth peculiarities. Fig. 1b illustrates this peculiarity of properties. It shows the typical dependences of anisotropy coefficients $K' = \frac{\varepsilon'_y}{\varepsilon'_z}$ and $K'' = \frac{\varepsilon''_y}{\varepsilon''_z}$ for real and imaginary components ε^* dependencies measured in the direction indicated by the subscript (see. Fig. 1a). Coefficients values are averaged over all samples of the same plate to eliminate possible influence on the measurement results of two-dimensional structural defects on the measurement results cause they have a random orientation and are clearly visible on the polished wafer surface. We notice that such defects are characteristic for melt-grown $A^{II}B^{VI}$ crystals with cubic modification [19]. As we can see from Fig. 1b, the direction of their growth is physically marked at electric polarization of investigated crystals in low-frequency region.

Conclusion

1.That way the wavelet analysis allowed to reveal the spatial ordering of $Cd_{1-x}Zn_xTe$ crystals composition which has a significant influence on their dielectric properties.

2.Investigation of such composition feature is important both for complete study of its connection with electric and other crystal properties and to improve the technology of their growth.

1. N.A. Bert, L.S. Vavilova, I.P. Ipatova et al. FTP, 33, 544 (1999).
2. I.V. Sabinina, A.K. Gutakovskiy, Yu. G. Sidorov et al. Letters to ZhETF, 34, 348 (2011).
3. P.V. Seredin, E.P. Domashevskaya, I.I. Arsent'ev et al. FTP, 47, 3 (2013).
4. Alex Zunger // MRS Bulletin, 22, 20 (1997).
5. V.K. Komar, S.L. Abashin, O.N. Chugai, et al. // Abstracts of the 16th International Conference on Crystal Growth (ICCG-16). PC 265 (2010).
6. T.E.Schlesinger, J.E. Toney, H. Yoon et al. // Mater. Sci. Engin. R., 32, 103 (2001).
7. H. Hermon, M. Schieber, R.B. James et al. // Nuclear Instruments and Methods in Physics Research. A., 410, 100 (1998).
8. V. Corregidor, E. Diéguez, J.L. Castaño et al. // Appl. Phys. Letters, 81, 5153 (2002).
9. P. Norton. Opto-Electronics Review, 10, 159 (2002).
10. N. M. Astafieva. UFN, 166, 1145 (1996).
11. I.M. Dryomin, O.V. Ivanov, V.A. Nechitailo. UFN, 171, 465 (2001).
12. V.A. Tkal, M.N. Petrov, N.A. Voronin. XIV National Conference on Crystal Growth (NKRK-2010), Heads of reports p.2, 327, Moscow (2010).
13. N.K. Smolentsev Osnovy teorii veivletov, Veivlety v MATLAB. M.: DMK Press, 2005, 304.
14. M. Misiti, Y. Misiti, G. Oppenheim, J-M. Poggi. Wavelet Toolbox For Use with MATLAB Version 2.2 (www.mathworks.com), 2002. 934.
15. P.I. Baranskiy, V.P. Klochkov, I.V. Potykevich. Poluprovodnikovaya elektronika. Svoistva materialov. Spravochnik. K.: Naukova dumka, 1975, 704.
16. S.-H. Wei, L.G. Ferreira, Alex Zunger // Phys. Rev. B., 41, 8240-8269 (1990).
17. V. N. Kanishchev. // ZhETF,144, 1165-1173 (2013).
18. Nataliya A., Verezub, Anatoly I. et al. // Book of Abstracts: 17th International Conference on Crystal Growth and Epitaxy (ICCG-17), 58-60 (2013).
19. S. P. Chumakova, N.A. Tikhomirova, A.V. Ginzberg et al. // Letters to ZhETF, 13, 1379-1384 (1987).

Вісник ХНУ, № 1158, серія «Фізика», вип. 22, 2015. с. 18-22

UDC 533.92

Calculation of the generator for induction discharge initiation

A.M. Deryzemlia, P.G. Kryshtal, V.I. Radchenko,
O.I. Yevsiukov, D.A. Khizhnyak, B.M. Shirokov

National Science Center "Kharkov Institute of Physics and Technology"
1 Akademicheskaya St. 61108 Kharkov, Ukraine

The upgraded RF generator operating at 880 kHz in wide ranges of radio-frequency power and gas pressure has been developed. The resonant circuits of the generator are calculated at 880 kHz. Real and imaginary components of the discharge system impedance versus the electron density are under consideration for the cylindrical inductively coupled plasma.

Keywords: RF generator, cylindrical inductively coupled plasma, silicon tetrachloride.

Представлено модернізований ВЧ генератор для збудження індукційного розряду, що працює на частоті 880 кГц в широкій області високочастотних потужностей і тисків газу. Проведено розрахунок резонансних кіл генератора на частоті 880 кГц. Розглянуто залежність дійсної і уявної складової імпедансу розряду від концентрації електронів для циліндричного індукційного розряду.

Ключові слова: ВЧ генератор, циліндричний індукційний розряд, тетрахлорид кремнію.

Представлен модернизированный ВЧ генератор для возбуждения индукционного разряда, работающий на частоте 880 кГц в широкой области высокочастотных мощностей и давлений газа. Проведен расчет резонансных кругов генератора на частоте 880 кГц. Рассмотрена зависимость действительной и мнимой составляющей импеданса разряда от концентрации электронов для цилиндрического индукционного разряда.

Ключевые слова: ВЧ генератор, цилиндрический индукционный разряд, тетрахлорид кремния

Introduction

At present plasma chemical processes are widely used in the world. The developing of discharge exciting sources is a main issue in organization of plasma-chemical processes, which must satisfy the requirements of the plasma-chemical system energy balance, maintenance of required gas and electron temperature, discharge sustaining in the predetermined pressure range when the partial pressure of initial reagents and pumping rates of the reaction products are changing.

There are various sources of discharge excitation. The induction high-frequency systems possess some comparative advantages among them. The coaxial disposition of the reactor and inductor simplifies the calculations of energy characteristics of plasma-chemical systems. Furthermore, the inductor situated outside the reaction chamber can slightly reduce the contamination of a final product in comparison with other excitation sources in which the plasma discharge is in contact with the structural elements of the plasma-chemical equipment.

The RF induction plasma sources are continuously improving in the direction of increasing the discharge energy input, pulsing and continuous lasing of the output signal, changing the continuous lasing frequency and pulse interval frequency, and increasing the efficiency of plasma chemical facilities. The high-frequency power, fed into the discharge, is absorbed in the skin layer. Therefore, to increase the plasma chemical system efficiency, the high-frequency exciting field should be sufficient for the electromagnetic energy release from the almost entire volume of a plasmoid.

In the plasma-chemical processes the use of the non-equilibrium plasma, characterized by the high electron energy at a relatively low gas temperature, occupies a special place that allows one to carry out chemical reactions for producing a final product and inhibits the reverse reaction [1], and also provides a possibility of carrying out chemical reactions, forbidden by thermodynamics, in equilibrium conditions.

Using of RF generators operating in the frequency range of 0.46÷2.0 MHz for induction discharge excitation, calculated in [2], shows that by changing the operating frequency from 13.56 MHz to the frequency 2.0 MHz the inductor power voltage is decreased in 3 times.

In addition, the application of RF generators for excitation of induction discharges, operating at low frequencies, allows one to minimize the loss in the inductor, as well as, in the circuits connected to it, and significantly simplifies discharge diagnosis.

The aim of the present study was the design modification of the commercial generator VChI-63/044, and its matching with the reactor inductor to carry out plasma-chemical investigations on the hydrogen reduction of silicon tetrachloride in the low-temperature non-equilibrium plasma.

Results and discussion

1. *Upgrading of the high-frequency generator VChI-63/044.*

The RF frequency generator VChI-63/044 operating in the pulse-periodic mode was upgraded to reach a continuous wave lasing at a frequency of 880 kHz. Changeover of the RF frequency generator to the continuous lasing mode has been performed by making a replacement of an adjustable thyratron rectifier by a non-adjustable diode one that appreciably improved the reliability and stability of the generator power source. The stable performance of the generator under various magnitudes of output power in a wide range of load parameters was ensured by dividing the matching circuits and power adjustment circuit. Continuous adjustment of the generator output power was carried out by the variable-ratio autotransformer set up at the power source input. The upgraded generator scheme is shown in Fig 1.

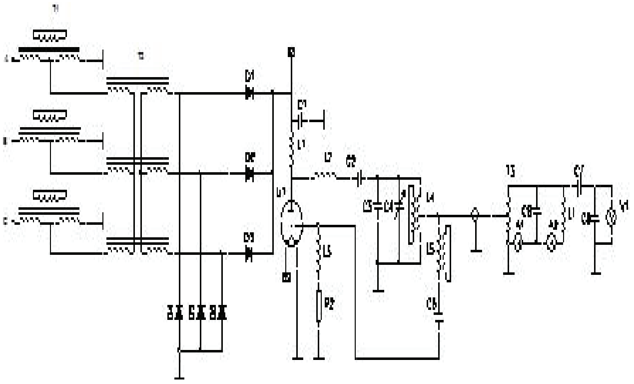

Fig.1. Schematic representation of the upgraded generator.

The generator is assembled on the GU-23-type lamp U1. Three-phase supply voltage of commercial frequency is fed via the adjustable autotransformer T1 of 25 kW, is increased by the high-voltage transformer T2 and then comes into the three-phase full-wave rectifier D1-D6. Each arm of the rectifier consists of twelve series-connected semiconductor diodes designed for the operational voltage of 1000V and 10A current and shunted by the 2W resistor with a resistance of 100 Ω.

The load circuit is formed by the inductor with an inductance of 6.5 μH and the capacitor C6 capacity of 5 nF. Harmonization of the generator with the load is carried out through the autotransformer T3. The autotransformer comprising 12 turns, of the 10 mm, copper pipe wound on the hull with diameter of 600 mm, has the inductance of 63 μH. The autotransformer design provides the step change of the turn ratio in the range from 0.08 to 1 by changing the number of turns in the primary circuit.

Measurements of voltage on the load circuit are carried out with the aid of a capacitance divider with a dividing coefficient of 1000:1. The current in the inductor and in the load circuit is measured with the aid of shielded Rogowski coils A1 and A2 respectively.

The parameters of the generator anode circuit were calculated by the framework of an equivalent circuit of the upgraded generator (Fig. 2), from the condition of resonance at the operating frequency and matching of the anode load equivalent resistance with a characteristic impedance of the cable. The coil with an average inductance value of 54 μH is used in the anode circuit of the generator. The anode circuit capacitance was calculated by the expression

$$C_A = \frac{1}{\omega^2 \cdot L_A}, \tag{1}$$

where ω is the generator operating frequency, L_A is the coil inductance of the anode circuit.

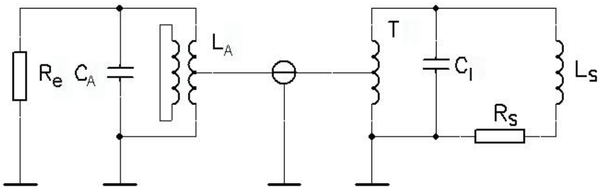

Fig.2. Equivalent circuit of the upgraded generator: R_e - the equivalent anode load resistance, L_A, C_A - anode circuit elements, T - matching autotransformer, C_l - capacitance of the load circuit, R_S - equivalent active resistance of the inductor with taken into account load influence, L_S - equivalent inductance of the inductor with taken in account load influence.

The estimated capacitance value for the frequency of 880 kHz is 606 pF. The plate circuit capacity is formed by both the capacitor battery of a fixed capacitance and the variable capacitor with a fluoroplastic dielectric of 20÷200 pF capacitance. The variable capacitor serves for fine resonance adjustment of the anode circuit.

The optimal value of the equivalent anode load resistance is determined from the expression:

$$R_e = \frac{U_{a\max}}{I_{a\max} \cdot a_1} - \frac{1}{S \cdot a_1}, \tag{2}$$

where $U_{a\ max}$ - maximum value of the anode voltage,

$I_{a\max}$ - maximum value of the anode current, a_1 - fundamental harmonic ratio, S - mutual conductance of the lamp.

At $U_{a\max}$=6.3 kV, the current value $I_{a\max}$ with maximum power 25 kW equals 4A. The fundamental harmonic ratio a_1 at cutoff angle of 70˚ equal to 0,436, the mutual conductance of lamp GU - 23÷48,5 mA/V. The calculated optimal value of equivalent resistivity of the anode load is 3564 Ω.

The characteristic anode circuit impedance $\rho = \sqrt{\frac{L_A}{C_A}}$ for a frequency of 880 kHz is 300 Ω, and its Q-factor is $Q = \frac{R_e}{\rho} \approx 12$. In order to match the equivalent resistance of the anode load with a cable having a characteristic impedance of 50 Ω, the coefficient of cable connection into the anode circuit $n = \sqrt{\frac{\rho_c}{R_e}}$ is 0.12.

To ensure the required connection coefficient values in the structure of generator VChI -63/044 coils, additional outlets for cable connections are provided.

2.Estimation of the RF plasma discharge impact on the inductor impedance.

The improved RF generator was tested on the experimental assembly with a cylindrical quartz discharge chamber. The quartz tube, surrounded by the inductor, consist of 6.5 turns with an inductance of 7.36 μH and resistance of 0.03 Ω. The influence of high-frequency discharge plasma on the inductor impedance was estimated using the transformer model of an induction RF discharge [1]. In transformer model the inductor itself serves as a primary winding, and the plasma, generated in its inside, forms a secondary winding consisting of a single turn, the radius of which is determined by the high-frequency plasma discharge parameters. The transformer model is schematically represented in Fig. 3a.

The secondary winding of the transformer is characterized by the plasma resistance R_2 and inductivity L_2. The plasma turn inductivity includes two components: geometrical or magnetic inductance L_2, determined by the turn geometry, and inductivity L_e characterizing the electron inertial properties. The inertial induction L_e is the result of a complex nature of the RF discharge plasma conductivity and is determined by the relation:

$$L_e = \frac{R_2}{\nu_{eff}}. \tag{3}$$

where V_{eff} is the effective electron collision frequency.

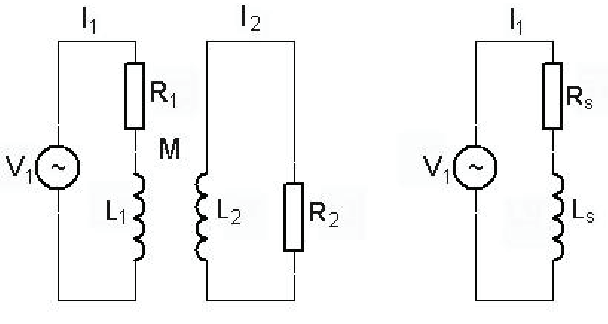

a b

Fig.3. a) Transformer model of the high-frequency discharge. b) Equivalent circuit of the high-frequency discharge in the transformer mode.

In the pressure range under consideration the collisional mechanism of energy input into the plasma discharge is implemented, and the electron-neutral collision frequency significantly exceeds both the stochastic collision frequency and the electron-ion collision frequency, that makes it possible to equate V_{eff} to the electron-neutral collision frequency V_{en}.

For the pressure range where $\frac{\nu_{en}}{\omega} \geq 10$ and $\nu_{en} \geq 5{,}5 \cdot 10^7 s^{-1}$ the inductance L_e is much lesser than L_2, that allows us to neglect the L_e contribution into the inductor-plasma system impedance.

The inductances L_1 and L_2 are related by the mutual inductance M**.** The coupling coefficient k is determined by the relation:

$$k = \frac{M}{\sqrt{L_1 \cdot L_2}} \tag{4}$$

The coupling coefficient k $(0 < k < 1)$ versus the electron concentration is shown in Fig. 4.

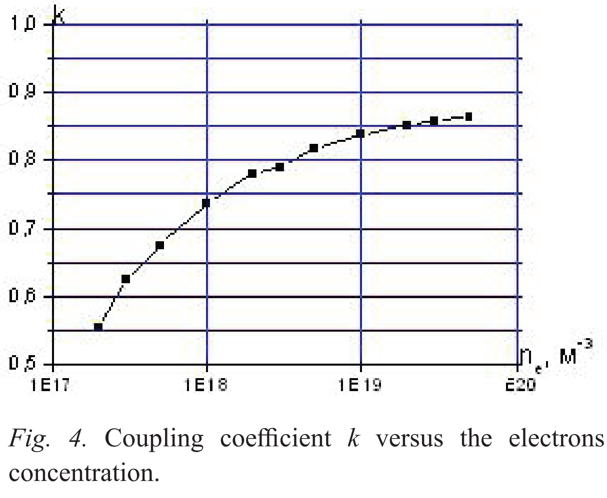

Fig. 4. Coupling coefficient k versus the electrons concentration.

The coefficient k monotonically increases with electron concentration increasing, asymptotically approaching to the theoretical maximum magnitude

$\mathrm{k} = \dfrac{\mathrm{R}^2}{\mathrm{B}^2}$, where R is the discharge chamber radius, B is the inductor radius.

Applying Kirchhoff's second law to the primary and secondary transformer windings we obtain

$$V_1 = j\omega L_1 I_1 + I_1 R_1 - j\omega M I_2 \quad (5)$$

$$V_2 = j\omega L_2 I_2 + I_2 R_2 \quad (6)$$

Considering that $V_2 = j\omega M I_1$, after simple transformations of equations (3) and (4), the inductor-plasma system impedance reduced to the transformer primary winding can be determined.

$$Z = \frac{V_1}{I_1} = R_1 + \frac{\omega^2 M^2}{R_2^2 + \omega^2 L_2{}^2} R_2 + \\ + j\left(\omega L_1 - \frac{\omega^2 M^2}{R_2^2 + \omega^2 L^2}\omega L_2\right) = R_s + jX_s \quad (7)$$

The equivalent circuit of the inductive RF discharge transformer model is shown in Fig. 3b. The real and imaginary components of the impedance inductor-plasma system versus the plasma electron concentration $\dfrac{\nu_{en}}{\omega} = 10$ are shown in Fig. 5.

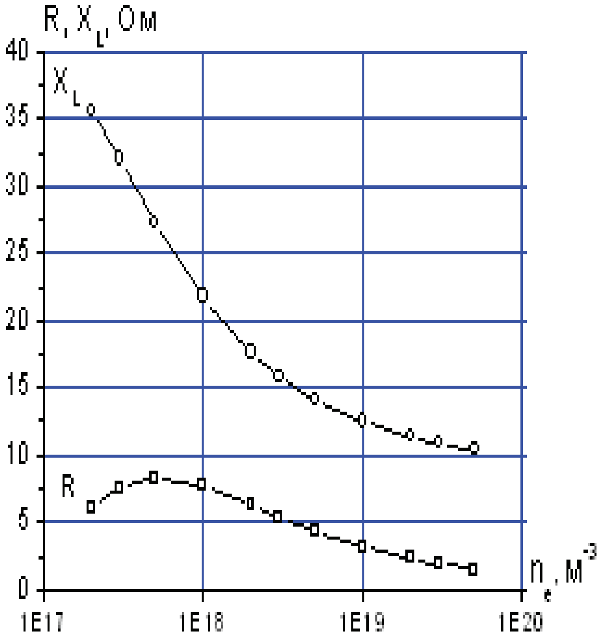

Fig.5. The real and imaginary components of the inductor-plasma system impedance versus the electron concentration for $\dfrac{\nu_{en}}{\omega} = 10$.

Assuming that the inputted induction RF discharge plasma power is absorbed in the skin layer of a depth δ, the plasma resistance can be determined from the expression

$$\mathrm{R}_2 = \frac{2\pi \cdot \mathrm{r}}{\sigma \cdot \delta \cdot \mathrm{h}}, \quad (8)$$

where σ is the real component of the complex conductivity of the high-frequency discharge plasma, δ - skin depth, h - discharge height, R - plasma turn radius equal to $r = R - \dfrac{\delta}{2}$ (R - discharge chamber radius).

The skin-layer depth is determined by the expression

$$\delta = \frac{c}{\omega_{pe}}\sqrt{\frac{2\nu_{eff}}{\omega}}, \quad (9)$$

where c is the light speed, ω_{pe} is the electron plasma frequency.

The plasma turn inductance is calculated by the relation

$$\mathrm{L}_2 = \frac{\mu_0 \pi \mathrm{r}^2}{\mathrm{h}}, \quad (10)$$

where μ_0 is the magnetic constant.

The mutual inductance M is determined from the expression

$$M = \frac{\mu_0 \pi r^2 n}{h}, \quad (11)$$

where n is the number of inductor turns.

It should be noted that by assessing the influence of the RF discharge plasma on the inductor impedance we have not considered the capacitive coupling between the inductor and the plasma, since at low frequencies it is not essential [3] and its influence on the inductor impedance can be disregarded.

In the model of the RF discharge transformer the generator power P_g can be considered as a sum of the power dissipated in the transformer primary winding (inductor) P_{in} and the power contributed to the plasma discharge P_d.

$$P_g = P_{in} + P_d = \frac{1}{2} I_1^2 (R_1 + R_2'), \quad (12)$$

where I_1 is the inductor current amplitude, and $R_2 = \dfrac{w^2 M^2 R_2}{R_2^2 + w^2 L_2^2}$ is the reduced active plasma resistance of the transformer primary winding. The efficiency of power transmission from the inductor to the plasma is determined by the relation [4]

$$\eta = \frac{P_d}{P_{in} + P_d} = \left(1 + \frac{R_1}{R_2'}\right)^{-1} . \qquad (13)$$

From the relation (13) it follows that with a fixed value of R_1 the value of $R_2^{/}$ will be an indicator of the efficiency of energy contribution into the plasma discharge, namely, high values of $R_2^{/}$ correspond to high values of η and conversely. The impedance components of the inductor-plasma system (Fig.5) and the mutual coefficient k (Fig.4) versus the electron concentration, and, consequently, the RF power absorbed in the plasma, indicate to the existence of optimal energy contribution modes in the induction RF discharge. The energy efficiency is determined by the discharge configuration and depends on the type and pressure of the operating gas. As the gas pressure increases, an optimal energy input range is shifted towards higher electron concentrations.

The generator testing has shown its stable operation. A HF discharge, excited in molecular hydrogen and mixtures of hydrogen with chlorosilane, was observed in the pressure range of 15-250 Pa. The power density fed into the discharge was varying in the range from 1 to 7.2 W/cm^2.

Investigations on the plasma-chemical hydrogen reduction of silicon tetrachloride were carried out. The reaction of plasma-chemical reduction was conducted in the reaction chamber at pressure of 60 Pa with the ratio H_2SiCl_4=5:1 (flow rate for H_2 - 6.5 l/h, for $SiCl_4$ - 1.3 l/h.) The power density, fed into the discharge, was 6.5 W/cm^2.. Polycrystalline silicon films with a thickness of 8.5–11.6 µm were obtained for deposition time of 60-80 minutes. [5]

Conclusions

1. Experiments conducted with a upgraded RF generator has shown a stable operation at a power density, fed into the discharge of 1 to 7.2 W/cm^2 in the broad range of varying power load parameters.
2. Plasma-chemical hydrogen reduction of silicon tetrachloride in the low-temperature non-equilibrium plasma was carried out. Polycrystalline films with thickness of 8.5-11.6 µm were obtained.

3. E.A. Kralkina. Inductive high-frequency low-pressure discharge and possibilities of optimizing the discharge-based plasma sources. Uspekhi Fizicheskikh Nauk, (2008), v.178, No 5, p.519-540 (in Russian),
4. Colpo P., Meziani T. and Rossi F. Inductively coupled plasmas: Optimizing the inductive-coupling efficiency large area source design. Journal of Vacuum Science and Technology (2005),v. 23, p.270-277.
5. Tuszewski M. Planar inductively coupled plasmas operated with low and high radio frequencies. IEEE Transactions on Plasma Science. (1999), v. 27, No 1, p.-68-69.
6. Piejak R.B., Godyak V.A. and Alexandrovich B.M. A Simple analysis of an inductive RF discharge // Plasma Sources Science and Technology. (1992), v.1, p. 179-186.
7. A.N. Deryzemlia, P.G.Kryshtal, D.G.Malykhin, V.I.Radchenko, B.M.Shirokov. Silicon hydrogen reduction from $SiCl_4$ in the induction HF discharge. Proceedings of the 7th International Symposium on the theoretical and applied plasma chemistry, 2-6 September 2014, Pless, Ivanov region, Russia. (in Russian).

Вісник ХНУ, № 1158, серія «Фізика», вип. 22, 2015. с. 23-30

UDK 539.374+669.715
PACS numbers: 62.20.Fe, 62.20.Hg

Mechanism of superplastic deformation of high-strength aluminum alloy 1933 with bimodal structure

A.V. Poyda[2], A.V. Zavdoveev[3,4], V.P. Poyda[1], V.V. Bryukhovetskiy[2], D.E. Milaya[1,2], R.V. Sukhov[1]

[1] V.N. Karazin Kharkov National University
Svoboda square, 4, Kharkov, Ukraine, 61077,
[2] Institute of Electrophysics & Radiation Technologies NAS of Ukraine
Chernyshevskaya St. 28, P.O. Box 8812, Kharkov, Ukraine, 61002
[3] Paton Electric Welding Institute of NAS of Ukraine
Bozhenko St., 11, Kiev, Ukraine, 03680
[4] Donetsk Institute for Physics and Engineering named after A.A. Galkin NAS of Ukraine
Nauky Prosp., 46, Kiev, Ukraine, 03028

The characteristics of the initial structural state and phase composition of industrial alloy 1933 are determined. The specific proportion of low-angle boundaries and high-angle boundaries is determined. The mechanism of superplastic deformation of aluminum alloy 1933 with a bimodal structure is considered. In the investigation of the deformation relief the fibrous structures are found, indirectly confirming the presence of a liquid phase during the mechanical tests. The effect of the inclusions of liquid phase, localized at the grain boundaries, on the implementation of deformation and accommodative mechanisms developing during their superplastic flow is analyzed.

Keywords: superplasticity, bimodal structure, grain boundaries, fibrous structures, partial melting.

Встановлено характеристики вихідного структурного стану і фазового складу промислового напівфабрикату сплаву 1933. Визначено питому частку малокутових і великокутових меж зерен. Розглянуто механізм надпластичної деформації алюмінієвого сплаву 1933 з бімодальною структурою. При дослідженні деформаційного рельєфу виявлені волокнисті структури, що опосередковано підтверджує наявність рідкої фази під час механічних випробувань. Проаналізовано вплив включень рідкої фази, локалізованих на межах зерен, на здійснення деформаційних і акомодацій механізмів, що розвиваються в ході їх надпластичної деформації.

Ключові слова: надпластичність, бімодальна структура, межі зерен, волокнисті структури, часткове плавлення.

Установлены характеристики исходного структурного состояния и фазового состава промышленного полуфабриката сплава 1933. Определена удельная доля малоугловых и большеугловых границ зерен. Рассмотрен механизм сверхпластической деформации алюминиевого сплава 1933 с бимодальной структурой. При исследовании деформационного рельефа обнаружены волокнистые структуры, что косвенно подтверждает наличие жидкой фазы во время механических испытаний. Проанализировано влияние включений жидкой фазы, локализованных на границах зерен, на осуществление деформационных и аккомодационных механизмов, развивающихся в ходе их сверхпластической деформации.

Ключевые слова: сверхпластичность, бимодальная структура, границы зерен, волокнистые структуры, частичное плавление.

Introduction

To show the effect of micro-grain structural superplasticity (SSP) of industrial aluminum alloys must have steady to coarsening ultrafine equiaxed grain structure [1-3]. It is considered that the smaller the initial grain size in the specimen, the greater the area of high angle intergranular (intergrain and interphase) boundaries per volume unit of its working part. Therefore, the greater the number of grains may be involved in the implementation of grain boundary sliding (GBS) - the main deformation mechanism of superplastic deformation (SPD) [1-3]. Such a structural state in multicomponent aluminum alloys with matrix structure can be obtained by carrying out of their thermomechanical processing. However, using of standard methods of heat treatment to the semifinished products of many commercial aluminum alloys is not always provides them uniform ultrafine equiaxed structures, so in the initial state they often have bimodal or varying grain size structure [1-4].

High-strength forging alloy 1933 of Al-Zn-Mg-Cu-Zr [5] is widely used in the aircraft industry. Large forgings, stampings and pressed strips for massive elements of the internal skeleton of the power of modern aircraft airframes are produced from it.

A significant disadvantage of this alloy as well as of other high-strength alloys of Al-Zn-Mg-Cu, is that the presence in its composition of high amounts of zinc, magnesium and copper to increase its strength, reduces its plasticity [6]. Low technological plasticity of the alloy 1933 greatly limits its use for the production of complex and thin-walled products needed for the aircraft industry. This disadvantage can be eliminated by the use of superplastic forming, which is a promising technology of materials processing by pressure based on the effect of SSP.

In [7-10] was shown that the alloy 1933 with an initial bimodal structure showed the effect of high-temperature structural superplasticity (HTSS). It is determined that during the SPD GBS developed intensively and occurred not only on ultrafine grain boundaries, but also on the boundaries of large poligonized grains parallel to the direction of strain. It is uncharacteristic for the existing classical conceptions about the development of GBS in terms of micro-grain SSP and can be connected with the presence on grain boundaries of small amounts of liquid phase.

In this paper in order to clarify the mechanism of SPD of alloy 1933, the characteristics of the initial structural state and phase composition of the alloy were studied and the attestation of its grain boundaries was performed.

Based on generalization of the results, obtained in the work, and accounting data available in the literature, the analysis of deformation and accommodative mechanisms of SPD of the alloy is performed.

Materials and methods of the experiment

Investigated in the paper alloy 1933 has such a chemical composition (1,6 – 2,2% Mg; 0,8 – 1,2% Cu; 0,1% Mn; 0,66 – 0,15% Fe; 0,1% Si; 6,35 – 7,2% Zn; 0,03 – 0,06% Ti; 0,05% Cr; 0,10 – 0,18% Zr; 0,0001 – 0,02% Be; base Al, % wt.) [5]. The main alloying elements in the alloy are magnesium, zinc and copper. They play a fundamental role in the partial melting of superplastic aluminum alloys and as a result, creating small amounts of viscous liquid phase at the grain boundaries during deformation [11-12].

Mechanical tests of the alloy specimens, prepared from industrial intermediates, held in air by stretching them in creep mode at constant flow stress according to the procedure described in detail in [13].

Grain structure, cavity morphology and morphology of fibrous in specimens were studied using light microscopy (MIM-6 with the digital camera Pro-MicroScan) and scanning electron microscopy (JEOL JSM-840), and standard techniques of quantitative metallography [14].

To determine the proportions of ultrafine and coarse grains, the grain boundary misorientation angles and to make quantitative assessment of their content in the alloy 1933 the electron backscatter diffraction analysis (EBSD) was used [15]. Investigations were performed using a scanning electron microscope JEOL JSM-6490LV, equipped with energy dispersive spectrometry INCA Penta FETx3 and by detector of backscattered electrons Nordlys S.

Analysis of the obtained structures was performed according to the procedure described in [15], using software HKL Channel 5, which is included in the set of technical documents to the microscope.

The surface of the working part of the specimens was subjected to grinding and to mechanical polishing. Surface finishing of sections for metallographic investigations was carried out using a diamond paste grit 1/0.

Specimens which were used for EBSD analysis were subjected to electropolishing. It was performed in a solution of such composition: 40 wt. % H_2SO_4, 45 wt. % H_3PO_4, 3 wt. % CrO_3, 11 wt. % H_2O [15]. Mode of operation: operating temperature 60-80°C, the anode current density, the voltage of 15-18 V, exposure – a few minutes.

To reveal the grain boundaries during the metallographic studies was used universal chemical etchant of such a composition: 17 ml HNO_3, 5 ml HF, 78 mL H_2O. In addition to the chemical etching for revealing of grain boundaries of the working part surface of the test specimens of alloy as the initial one, and superplastically deformed to a certain degree of deformation, strain relief method was used. To determine the contribution of grain boundary sliding (GBS) in the overall deformation and for studying of the kinetics of its development at different stages of SPD used a method of marker scratches. On the polished specimens using a diamond paste of dispersion 3 microns, the marker risks parallel to the axis of their subsequent direction of stretching were applied. Mechanical testing was carried out using specimens in a HTSP in the creep mode, which led to the formation on the surface of polished specimens of a deformation relief as a result of a small (3-5%) deformation. The views of it were studied.

The average grain size $\langle d \rangle$ was determined by light microscopy photomicrographs with use of random secant method [8]. Full statistical grain size distribution based on the data of EBSD analysis.

Results and Discussion

Figure 1, a shows a micrograph of a typical view of the initial microstructure of the specimen of 1933 alloy obtained using light microscopy techniques. It is seen that the microstructure of the alloy is bimodal. It consists of the regions containing a large number of fine recrystallized grains and ultrafine grains with $\langle d \rangle = 7 \pm 1$ *microns*, separated by high-angle boundaries (HAB, misorientation angle > 10°) of grains and contain some amount of coarse elongated poligonized grains with $\langle d \rangle = 50 \pm 1$ *мкм*, which are separated by low-angle boundaries (LAB, misorientation angle < 10°) of grains.

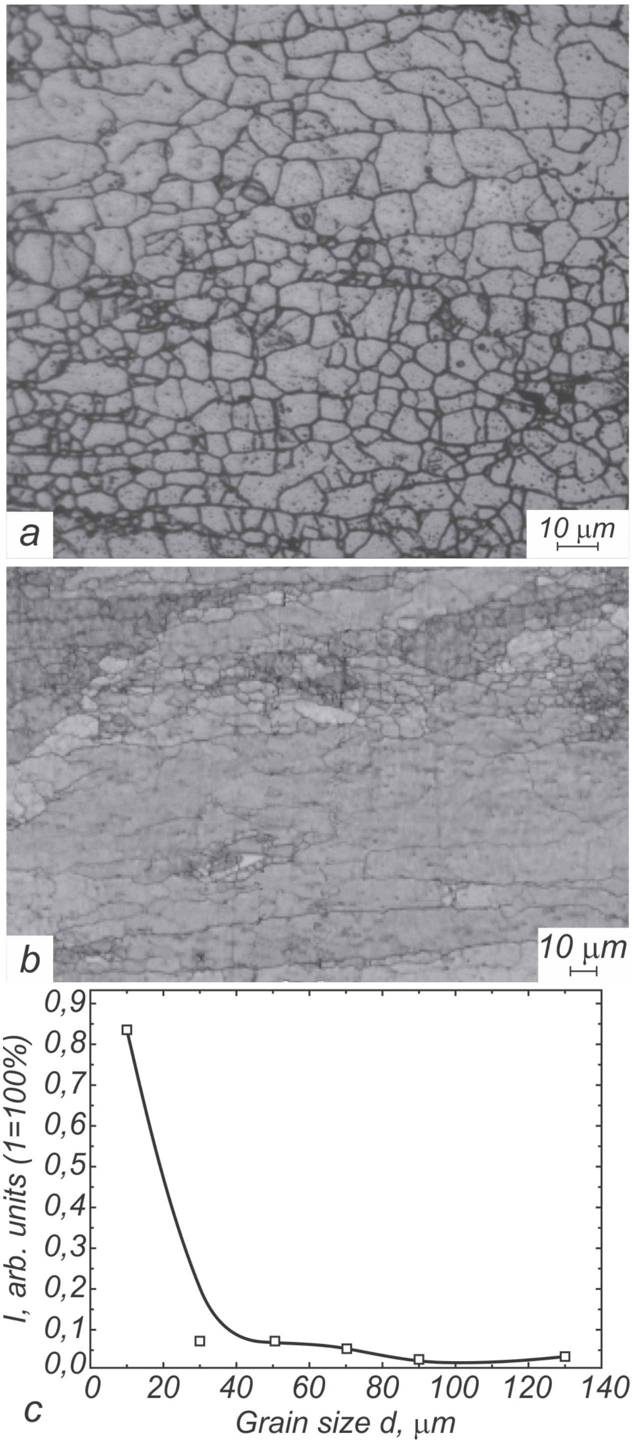

Fig.1. Typical views of the initial microstructure specimen alloy 1933: a – obtained by using light microscopy techniques; b – selected for EBSD analysis; c – the grains size distribution ⟨d⟩ for shown on Fig.1, b fragment of specimen of alloy 1933.

Data of metallographic investigations, obtained using light microscopy method, are qualitatively consistent with the data obtained as a result of EBSD analysis.

Figure 1, b shows the map of contrasts, which was used for quantitative metallographic analysis of the initial structural state of the alloy in the investigated part of the surface of the specimen of alloy 1933. It is seen that the original structure of the alloy is not uniform. It contains large elongated grains, which border on plots occupied by

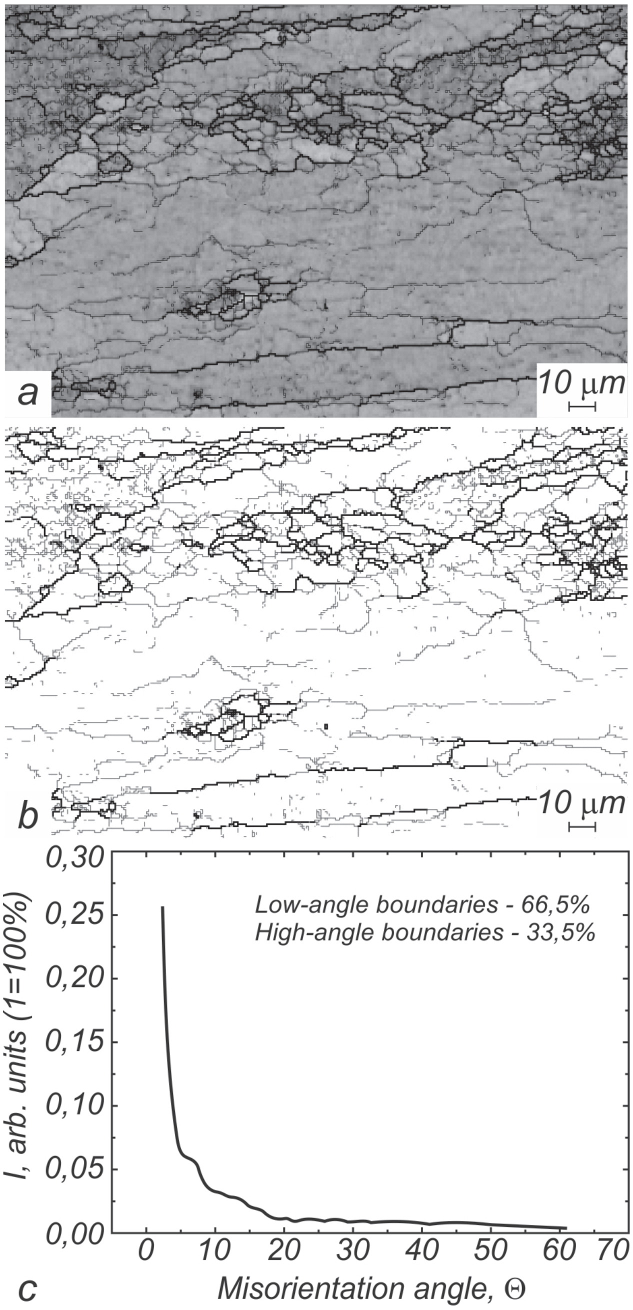

Fig.2. EBSD analysis maps: a – resulted from combination of contrasts map and misorientation angle of grain boundaries map; b – orientation angles of grain boundaries map; c – dependence of the relative amounts of different grain boundary misorientation angle from disorientation for the tested plot of the surface of alloy 1933 specimen.

small and ultra-fine grains.

Figure 1, c shows the distribution of the grain sizes by the magnitude for the investigated part of the alloy 1933 specimen. It is evident that in a bimodal structure identified on the surface of the investigated area, fine and ultra-fine grains dominate and the amount of large polygonized grains is much less.

Figure 2, a shows a fragment of the microstructure, obtained as a result of overlapping of contrasts maps and maps of misorientation angle of grain boundaries, and figure 2, b is a map of orientation angle of grain boundaries. These maps were used to determine the specific proportion of LAB grains and HAB grains for the tested plot of the specimen surface of the alloy 1933.

In Figure 2, *c* the quantitative distribution of the grain boundaries by misorientation angle is represented. It was built as a result of accounting of all attested grain boundaries existing in the studied area of specimen of alloy 1933. When building this relationship was usually to attribute to the LAB grains those grain boundaries, which have misorientation angle below 10°, and to attribute to the to HAB - those grain boundaries, which are misoriented above 10° [15]. It was found that the specific proportion of LAB grains for the tested area is 65.5% and the specific proportion of HABs grains is 35.5%. These data strongly suggest that the original structure of the specimens of alloy 1933 is not fully recrystallized, and that in it there is a developed substructure.

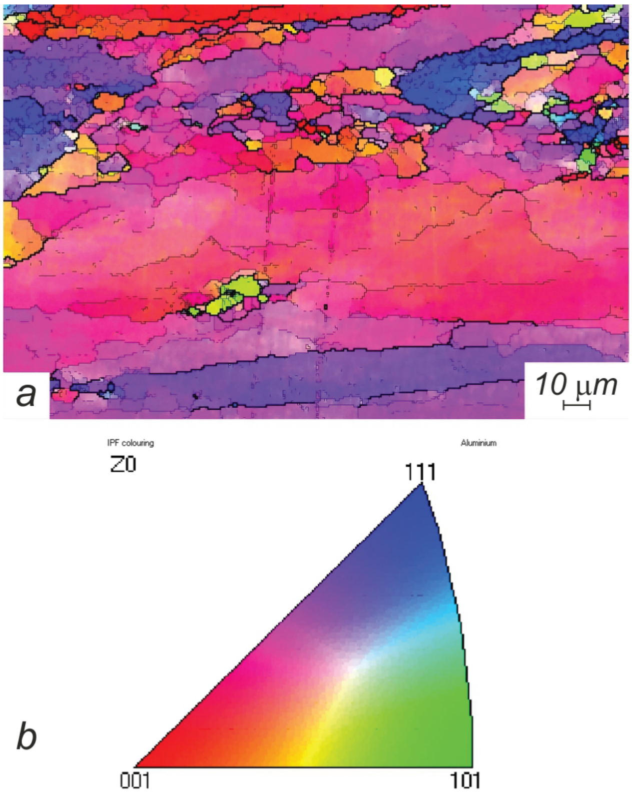

Fig.3. a – orientations of grains map in the investigated area of alloy 1933 specimen; b – image legend for this orientations map.

Figure 3, *a* shows a map of grains orientations in the investigated area of specimen of alloy 1933, and in Figure 3, *b* - the image of the legend to it, which was built in the space of inverse pole figures. It is seen that the orientation of the grains in this area are distributed inhomogeneously. For ultrafine grains are prevalent orientations tending to an orientation (111) and (001), and for large polygonized grains, prevailing is orientation, tending to the orientation (001). On the orientations map is also present a number of grains painted in green. Their orientation tends to orientation (101).

Let us analyze the phase composition of alloy 1933 specimens. According to the phase diagram of Al-Mg-Cu-Zn, [6], zinc, magnesium and copper under conditions close to equilibrium form with aluminum and between each other solid solutions and various intermetallic compounds: $MgZn_2$ (η-phase), Al_2CuMg (S-phase), $Mg_3Zn_3Al_2$ (T-phase), which play a significant role in the hardening of the alloy 1933 when heat treated. In addition to these phases in composition of the alloy 1933 in conditions close to equilibrium, must be present fine particles of phase $ZrAl_3$, which play an important role in the occurrence of dynamic recrystallization and serve to inhibit grain growth during SPD of aluminum alloys [1-3]. As a result of diffracometric research of initial specimen of the alloy 1933 [7-9], it was found that the intensive diffraction peaks on the diffractogram correspond to the aluminum based solid solution (α_{Al}-phase). It also revealed a low-intensity diffraction peaks corresponding η-phase ($MgZn_2$) и T-phase ($Mg_3Zn_3Al_2$). This indicates that the amount of η-phase and T-phase in the initial specimen of the alloy is not significant. S-phase and phase $ZrAl_3$, which, undoubtedly, are present in the initial specimens of the alloy 1933, were not found by the methods of diffraction. Since the crystallization of alloy ingots of 1933, like other alloys of the Al-Mg-Cu-Zn, takes place in conditions far from equilibrium, so in the structure of the alloy may be present intermetallic particles, which come in various nonequilibrium structural components characteristic of the alloys of this system [6].

As a result of energy dispersive X-ray microanalysis of the initial microstructure of the alloy 1933 the concentration of aluminum, zinc and magnesium at the grain boundaries and in the middle of grain was determined [10]. It is determined that the concentration of zinc and magnesium which is responsible for reducing the temperature of the partial melting of superplastic aluminum alloys [11,12] on individual grain boundaries is higher compared with their average concentration in the material and in the middle of the grains.

The previously mentioned indicates that in the specimens ща 1933 alloy prepared for mechanical testing, most of the alloying elements (Mg, Zn) is in the solid solution based on aluminum. Only in some parts of the grain boundaries, there is an increased concentration of alloying elements.

It was determined [7-10] that during heating of alloy 1933 specimens to a test temperature, partial melting of the alloy takes place. It results in the appearance of metastable viscous liquid phase at grain boundaries.

As a result of mechanical tests carried out in creep mode at a constant flow stress, it was found that the optimal conditions for occurrence of the effect of HTSP for alloy 1933 are as follows: temperature T = 520°C, flow stress σ = 5,5 MPa. Maximum relative elongation of specimen to failure δ, superplastically deformed under T = 520°C, σ = 5,5 MPa and true strain rate $1{,}2\cdot10^{-4}$ s^{-1} was observed as 260% [7-10].

As a result of detailed studies of typical views of deformation relief which formed on the surface of the working part of superplastically deformed alloy 1933specimens, performed using optical and scanning electron microscopy fibrous structures (see. Fig.4), localized in the cavities and microcracks were found. The formation and development of such structures shows convincingly that the alloy 1933 during SPD was in a solid-liquid state due to partial melting.

The ends of the fibers (see. Fig.4) are connected to the inner surfaces of grains in cavities formed during the separation during of grains, when grains separated one from each other by boundaries during GBS, approximately perpendicular to the strain direction. The number of fibers in cavities is different. It appears to depend on the amount of liquid phase inclusions localized at the grain boundaries, which surround the grain boundary cavities.

As a result of energy dispersive X-ray microanalysis of the chemical composition of the material that makes the fibrous structure formed during SPD of 1933 alloy specimens, was determined [10], that the concentration of Mg in them is increased in comparison with the average concentration in the alloy. This result agrees with the data on the chemical composition of the fibers obtained by the authors of works [16,17] in the study of the structural state of the specimens of aluminum alloys Al-Mg-Cu-Zn, showed HTSP in a solid-liquid state.

On the surface of the fibers and grains to which they are connected, friable oxide films were found. This suggests that during SPD of 1933 alloy specimens tested at a temperature T=520°C in its working part the dynamic oxidation of the inclusions of liquid material that was present in small amounts at the grain boundaries and at the sliding grain boundary edges intensively occurred.

These thermal studies, which were aimed at investigation of the probable causes of the kinetics of partial melting of the alloy 1933 [9] in the presence of superplastically deformed at T = 520 ° C specimens of fibrous structures which comprised an increased concentration of magnesium strongly indicate that this alloy shown HTSP in solid-liquid state.

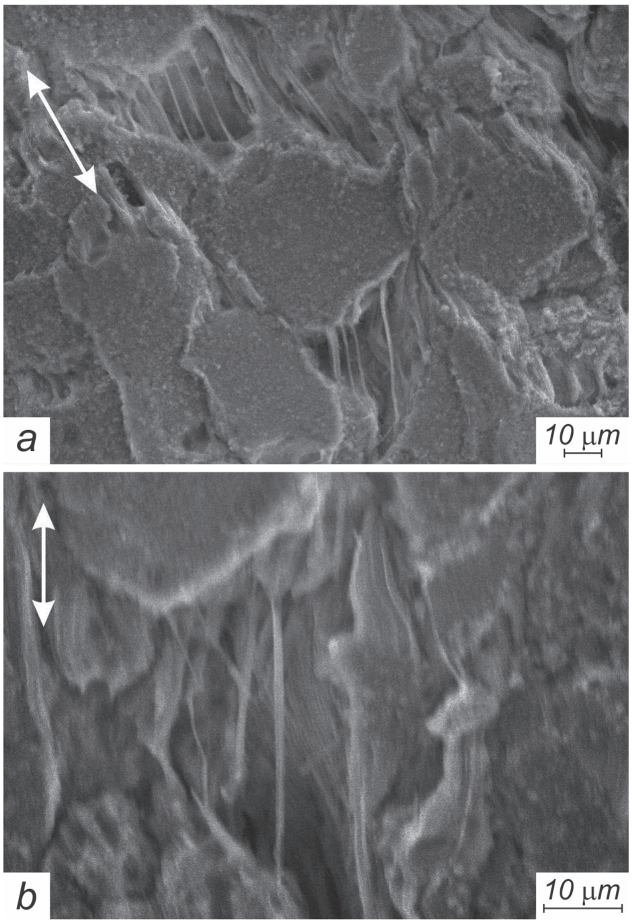

Fig.4. The deformation relief of alloy 1933 specimens, deformed to failure under the optimal conditions of high-temperature superplasticity. Scanning electron microscopy. Arrows indicate the tensile direction of specimens.

Let us analyze the influence of the structural state and phase composition of the alloy 1933 on the development of deformational and accommodative mechanisms of its SPD.

Analysis of the specific views of deformation relief formed on the surface of superplastically deformed specimens, typical views of which are shown in Figure 5, and the use of previously obtained data on the contribution of GBS to the local deformation of its specimens [8-9] provides a basis to offer a qualitative description of the development of deformational and accommodative mechanisms of SPD of alloy 1933 with a bimodal structure.

We can assume that during superplastic flow of specimens of the alloys 1933, at the same time take place three main deformation mechanisms: GBS, intragranular deformation carried out due to sliding and climbing of lattice dislocations and diffusion creep.

In [18,19] considered the effect of the presence of a bimodal structure on the development of SPD of aluminum alloy 01570C specimens (Al − 5,0% wt. Mg − 0,18 % wt. Mn − 0,2 % wt. Sc − 0,8 % wt. Zr). It

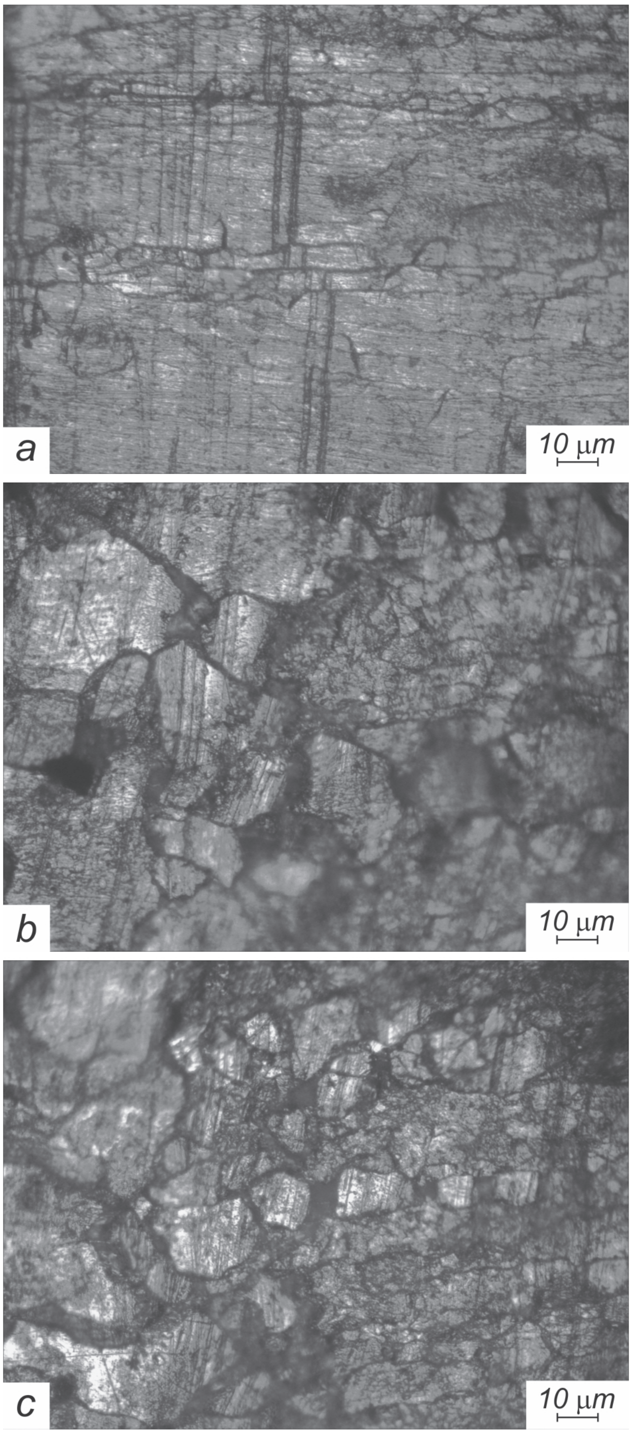

Fig.5. Characteristic views of deformation relief formed on the surface of the working part of specimens of alloy 1933, deformed to failure under the optimal conditions of high-temperature superplasticity. The tensile direction is horizontal. Light microscopy.

is suggested that in the process of dynamic loading of the specimen initially large grains begin to deform. In this case intense flows of lattice dislocations generate, they fall on the HABs grains in a fine-grained structure, transfer them to a non-equilibrium state. This enables the development of GBS in the fine structure part of the alloy. Streams of lattice dislocations from volume of coarse grains activate the overwhelming number of HABs grains. Under the influence of the dislocation stream excess nonequilibrium volume of HABs grains increases, and as a result, the diffusion processes in such boundaries are significantly more active, which leads to faster diffusion of HABs and the intensive development of GBS [1,18,19].

We can assume that in the specimens of studied 1933 alloy intragranular deformation of the alloy, which is used to create nonequilibrium state of HABs grains by applying stress to the specimen starts to be implemented simultaneously in large elongated polygonized grains, and in the fine and ultrafine grains in which the external stress in according to the Schmidt law, reaches a critical shear stress.

In [8,9], it was found that GBS in the specimens of alloy 1933 intensively take place at the grain boundaries, which consist of areas occupied by the solid and liquid phases.

Apparently, intense GBS on solid areas of HABs of ultrafine and fine grains takes place on the same micro-processes that are active in terms of manifestation of micro-grain SSP [1,2]. However, in consideration of deformation mechanisms of alloy 1933 is necessary to take into account that in specimens of aluminum alloys, superplastically deformed at high homologous temperatures, GBS may be further intensified by the separation of grain boundary dislocations from the impurity atoms on the atmospheres of ultrafine grain boundaries [20], as well as by substantially increasing diffusion processes at the boundaries of coarse grains [21].

Apparently, intense GBS occurring on the solid parts of HABs boundaries of large and of ultrafine grains, accompanied by the development of viscous flow in those areas of HABs and LABs of all the grains that contain a viscous liquid phase, which is a liquid-solid suspension. As a result, as shown in [9,10], GBS can intensively develop not only on the HABs of fine and ultrafine grains but also on LABs of coarse grains, including polygonized grains oriented parallel to the axis of tension of the specimen.

It was determined [9,10], that the contribution of GBS to the local deformation of the specimen due to the implementation of GBS in different parts of their working part is different. As shown estimate calculations [9,10], its values are within the range of ≈ 50% and ≈ 80%.

As shown in [22], the liquid phase, which borders with potential stress concentrators (intermetallic particles, triple junctions of grains and other structural inhomogeneities, which are available on the grain boundaries), promotes relaxation of local stresses arising during the GBS.

When at the intercrystalline boundaries there are areas occupied by the liquid-solid phase, the GBS on such boundaries can be facilitated as compared with sliding on “solid” boundaries.

In the specimens of investigated alloy 1933, this process will be implemented under the action of shear stresses due to relative displacement of the layers of liquid-solid phase enriched by surface active elements, since, as specified in [22], in a case if the liquid phase is in the form of a film between the crystallites, the deformation capacity of the material shearing increases, and its peel strength is retained.

To ensure the stability of the SPD during superplastic flow of investigated specimens of alloy 1933, in their working part must the effectively different accommodative mechanisms within the grains and at their sliding boundaries must take place, as well as in the area of contact between the liquid and solid phases. Accommodation of GBS can be effectively implemented with the active development of lattice and grain boundary diffusion in the solid phase and diffusion in the liquid phase. Active implementation of accommodative processes in the specimens of investigated alloy 1933 superplastically deformed in a solid-liquid state, promotes the effective stress relaxation in difficult for GBS areas of grain boundaries. As a result of a coherent implementation of the above-mentioned deformational and accommodative processes in the working part of the specimens of studied in this paper alloy 1933 with a bimodal structure the intensive rearrangement of grains with grain boundary cavities takes place, which is accompanied by viscous flow of liquid-solid phase localized at grain boundaries.

It is determined that at the early stages of superplastic flow in the working part of the alloy 1933 specimens, under the influence of normal stress on the HABs grains perpendicular to the tension direction of specimens begin to form wedge-shaped cracks. In those areas of the working part of specimens in which a partial melting of the alloy did not take place or the amount of liquid phase was small, it entirely dissolved in solid phase to the beginning of deformation. Wedge-like cracks during GBS were transformed into individual grain boundary cavities, developing in accordance with the mechanism proposed in [23] for micro-grain SSP, which took place in the solid phase.

Those wedge-like cracks that were formed by the mutual sliding of grains, boundaries of which contained inclusions of liquid-solid phase will also be transformed into the individual grain boundary cavities. Fibrous structures begin to form and develop during this. The edges of the grains, perpendicular to the strain axis of the specimen, i.e., walls of the cavities and cracks in this case act as a sort of “holders” to which fibers formed as a result of viscous flow of liquid-solid material is “attached”. Further development of cavities and cracks occur mainly due to GBS, which is carried by grains adjacent to cavities with a speed of grain boundary shift through solid sections of the boundaries, the growth rate of the fibrous structures during SPD of specimens of the alloys is probably close in magnitude to the rates of the disclosure of long grain boundary in which they are formed. As follows from data presented in [24], the growth rate of deformational cavities and the local rate of SPD associated with the presence and participation of these cavities in the deformation process, on average is about twice higher than the overall rate of SPD of specimen. Obviously, that the same in order of magnitude is the rate of development of fibrous structures during SPD, i.e. the rate of so-called “microsuperplasticity” [25].

This work is done with partial support by the target complex program “Fundamental Problems of Creation of New Nanomaterials and Nanotechnologies”, project №62/15-N.

Conclusions

1. The initial structural state of industrial alloy 1933, which showed the effect of high-temperature structural superplasticity in a solid-liquid state is investigated. It is shown that the original structure of the alloy 1933 is bimodal.

2. The specific proportion of grain boundaries of different misorientation in the initial specimens of alloy 1933, prepared for mechanical testing is determined. It is found that the specific proportion of the low-angle boundaries of grains is 65.5%, while the proportion of high-angle boundaries of grains is 35.5%.

3. The influence of the initial structural state and phase composition of alloy 1933 on the development of grain-boundary sliding and other mechanisms of its superplastic deformation, carried out on grain boundaries of different misorientation, as well as in the core of ultrafine and coarse grains during high-temperature superplasticity is analyzed.

4. The mechanism of grain boundary sliding in the alloy 1933 with a bimodal structure, intensively carried out on high-angle boundaries of fine and ultra-fine grains, as well as on low-angle boundaries between coarse, including polygonized grains oriented parallel to the tensile axis of the specimen is considered.

1. I.I. Novikov, V.K. Portnoy. Sverkhplastichnost metallov i splavov s ultramelkim zernom. M.: Metallurgiya, (1981), 168s.
2. O.A. Kaybyshev. Sverkhplastichnost promyshlennykh splavov. M.: Metallurgiya, (1984), 264s.
3. Superplastic Forming of Structural Alloys, Ed. by N.E. Paton and C.H. Hamilton. The Metallurgical Society of AIME, San Diego, California, (1982), 312p.
4. V.N. Shcherba. Pressovanie alyuminievykh splavov. M.: Intermetinzhiniring, (2001), 768s.
5. V.M Beleckii, G.A. Krivov. *Alyuminievye splavy (sostav, svoistva, tehnologiya, primenenie) spravochnik* / Pod obshei redakciei akademika RAN I.N. Fridlyandera. K.: Kominteh. 2005, 315p.
6. V.I. Elagin. V.V. Zakharov, M.M. Drits. Struktura i svoystva

splavov sistemy Al-Zn-Mg. M.: Metallurgiya (1982), 224s.

7. D.E. Pedun, V.P. Poyda, T.F. Sukhova, A.P. Samsonik, V.V. Litvinenko, E.L. Spiridonov. *Visnyk KhNU, seriia «Fizyka»*. **V.16**, №1019, 63 (2012).
8. D.E. Pedun, V.P. Poyda, V.V. Bryukhovetskiy, A.V. Poyda, A.P. Kryshtal', T.F. Sukhova, A.L. Samsonik, V.V. Litvinenko, E.K. Spiridonov. *Metallofizika i noveyshie tekhnologii*, **V.34**, №10, 1397 (2012).
9. V.P. Poyda, D.E. Pedun, V.V. Bryukhovetskiy, A.V. Poyda, R.V. Sukhov, A.L. Samsonik, V.V. Litvinenko. *FMM*, **V.114**, №9, 779 (2013).
10. D.E. Pedun, V.P. Poyda, V.V. Bryukhovetskiy, A.V. Poyda, R.V. Sukhov, A.P. Kryshtal'. *Visnyk KhNU, seriia «Fizyka»*, **V.18**, №1075, 55 (2013).
11. M. Mabuchi, H.G. Jeong, K. Hiraga, K. Higashi. *Interface Sci.* **V.4**, №3 – 4, 357 (1996).
12. I.I. Novikov, V.K. Portnoy, V.S. Levchenko, A.O. Nikiforov. *Mater. Sci. Forum.* **Vol.243 – 245**, 463 (1997).
13. V.P. Poyda, R.I. Kuznetsova, T.F. Sukhova, N.K. Tsenev and others. *Metallofizika*, **V.12**, №1, 44 (1990).
14. S.A. Saltykov. Stereometricheskaya metallografiya. M.: Metallurgiya, (1976), 272 s.
15. V.N. Varyukhin, E.G. Pashinskaya, A.V. Zavdoveev, V.V. Burkhovetskiy. Vozmozhnosti metoda difraktsii obratnorasseyannykh elektronov dlya analiza struktury deformirovannykh materialov. K.: Naukova dumka, (2014) 101s.
16. C.L. Chen, M.J. Tan. *Mater. Sci. and Eng*. A., **298,** 235 (2001).
17. W.D. Cao, X.P. Lu, H. Conrad. *Acta. Mater*., **44**, №2, 697 (1996).
18. T.G. Karnavskaya, E.V. Avtokratova, A.M. Bragov, M.V. Markushev, O.Sh. Sitdikov, V.N. Perevezentsev, M.Yu. Shcherban'. *Pis'ma v ZhTF*. **V.38**, V.13. 48 (2012).
19. O.E. Mukhametdinova, E.V. Avtokratova, O.Sh. Sitdikov, M.V. Markushev *Vestnik Tomskogo GU*. **V.18**, I.4. 972 (2013).
20. R.O. Kaybyshev, F.F. Musin. O «subsolidusnoy» sverkhplastichnosti. *DAN*, **V.373**, №2, 185 (2000).
21. M.Yu. Gryaznov, V.N. Chuvil'deev, V.E. Kuzin, M.M. Myshlyaev, V.I. Kopylov. *Fizika tverdogo tela*. *Vestnik Nizhegorodskogo universiteta im. N.I. Lobachevskogo*. №6 (1). 49 (2011).
22. Higashi K., Nieh T.G., Mabuchi M., Wadsworth J. *Scripta Met. et Mater.*, **V.32**, N7. 1079 (1995).
23. R.I. Kuznetsova. *FMM*, **V.45**, I.3, 641. (1978).
24. R.I. Kuznetsova, V.V. Bryukhovetskiy, V.P. Poyda, T.F. Sukhova. Metallofizika i noveyshie tekhnologii. **V.17**, №8, 64 (1995).
25. W.J.D. Shaw., *Materials Letters*, **4**, 1 (1985).

Вісник ХНУ, № 1158, серія «Фізика», вип. 22, 2015. с. 31-34

PACS: 61.10.Nz, 61.05.-a, 61.14.-x.

Computer indexing Laue diffraction pattern, the determination of the crystallographic orientation of the grains relative to the main directions in the crystal and the Schmid factor for all slip systems

T.R. Zetova, E.V. Ftemov, A.G. Tonkopryad, E.E. Badiyan

Department of Physics, Department of Solid State Physics,
Kharkov National University, 4 Svoboda Sq., 61077 Kharkov, Ukraine
Evgeny.E.Badiyan@univer.kharkov.ua

We describe a technique of computer indexing Laue patterns, determining the crystallographic orientation of the single-crystal sample (or a single grain of a polycrystal) relative to the main directions in the crystal, and Schmid factors for all systems sliding without the use of construction of a stereographic projection of the normals to the reflecting planes.

The basic algorithm of this procedure is to define and build a system of unit vectors of the normals to the Laue diffraction pattern, and according to the terms of her shooting, similar to the definition of the radius vector to the crystallographic orientation of the crystal planes known, combining them into a single computer center and a reversal of these systems relative to each other before the match First the radius vector with a portion of the latter. Thus, the indices of the reflecting planes are determined to Laue spots. After the Laue diffraction pattern indexing program to determine the crystallographic orientation of the studied sample and Schmid factor values for all slip systems.

Keywords: computer technique, the unit vectors, crystallographic orientation, Schmid factor.

Описана комп›ютерна методика індиціювання лауеграмми, визначення кристалографічної орієнтації монокристалічного зразка (або окремого зерна полікристала) щодо основних напрямків у кристалі і факторів Шміда для всіх систем ковзання без використання побудови стереографічної проекції нормалей до відбиваючих площин.

Основним алгоритмом цієї методики є визначення та побудова системи одиничних векторів нормалей до відбиваючих площин за даними лауеграмми і умов її зйомки, аналогічні визначення системи радіус– векторів до кристалографічних площин відомої орієнтації кристала, суміщення їх в один центр і комп›ютерне розвертання цих систем відносно один одного до збігу перших радіус векторів з частиною останніх. Таким чином, визначаються індекси відбиваючих площин для лауеграмми. Після індіціювання лауеграмми програма дає можливість визначити кристалографічну орієнтацію дослідженого зразка та значення фактора Шміда для всіх систем ковзання.

Ключові слова: комп›ютерна методика, одиничні вектори, кристалографічна орієнтація, фактор Шміда.

Описана компьютерная методика индицирования лауэграмм, определения кристаллографической ориентации монокристаллического образца (или отдельного зерна поликристалла) относительно основных направлений в кристалле и факторов Шмида для всех систем скольжения без использования построения стереографической проекции нормалей к отражающим плоскостям.

Основным алгоритмом этой методики является определение и построение системы единичных векторов нормалей к отражающим плоскостям по данным лауэграммы и условиям ее съемки, аналогичные определения системы радиус – векторов к кристаллографическим плоскостям известной ориентации кристалла, совмещение их в один центр и компьютерный разворот этих систем относительно друг друга до совпадения первых радиус векторов с частью последних. Таким образом, определяются индексы отражающих плоскостей для лауэпятен. После индицирования лауэграммы программа позволяет определить кристаллографическую ориентацию исследованного образца и значения фактора Шмида для всех систем скольжения.

Ключевые слова: компьютерная методика, единичные вектора, кристаллографическая ориентация, фактор Шмида.

Introduction

It is well-known, that all crystaline bodies due to their structure are anisotropic, i.e. their physical properties depend on crystallographic direction. In most cases, it concerns mechanical properties. That is why, while researching pattern of development of plastic deformation and determining mechanical features of monocrystalline samples or separate grains of polycrystalls, the main condition is determining of their crystallographic orientation. For this reason, as a rule, a well-known X-ray Laue method is used[1]. The deciphering of lauegram, where each reflex (laue – spot) is a reflection of definite crystallographic plane with indexes (hkl), allows to determine crystallographic orientation of monocrystaline sample for separate grains of polycrystal in relation to the main directions in the crystal (for cubical crystals this is [001], [110], [111]).

Traditional and single method [2,3] of deciphering of lauegrams included building stereographic projection of normals to reflected planes with known indexes (according to the lauegram) and its comparison to similar stereographic projections of normal to planes with known indexes, built in advance, for crystals with different crystallographic orientation. This method is pretty demanding and not always gives unambiguous results.

Lately appeared the works [4], where the method that eliminates the building of stereographic projection of normals to reflections planes is described. The algorithm of this methodology is geometrical determination of angles between reflecting planes, taking into account the conditions, received with the help of lauegram, and their comparison with the angles between the directions of crystal bar with known indexes. This methodology greatly simplifies the procedure of indexing of lauegram, but it does not allow to completely automatize the method of determining crystallographic orientation of researched sample – monocrystalline.

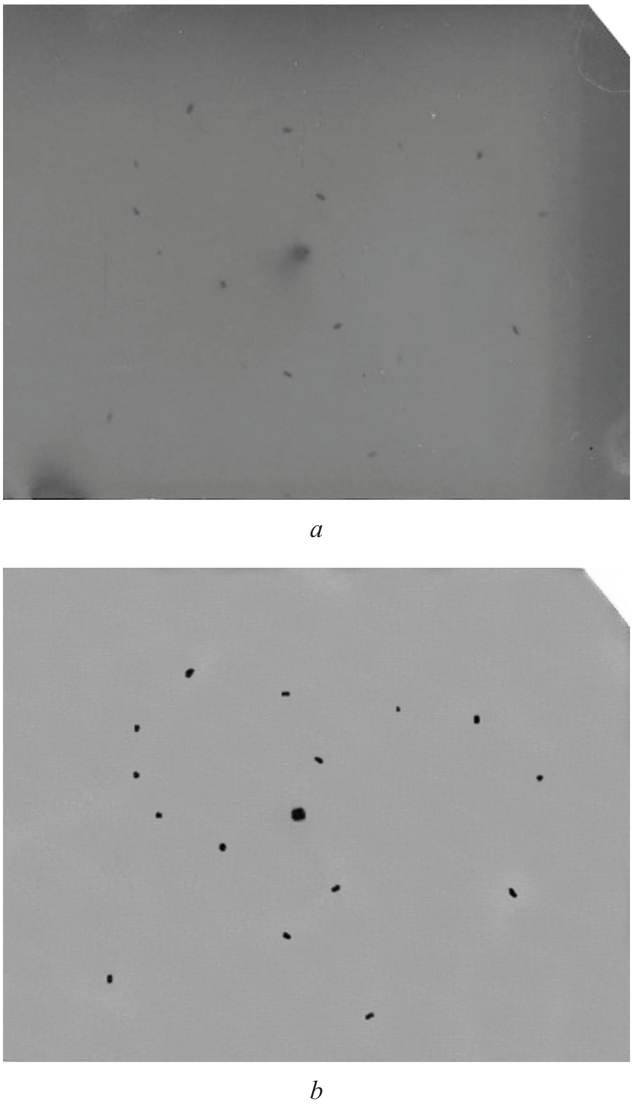
a

b

Fig. 1. Images of scanned (a) and edited (b) lauegram, received from one of grains of polycrystalline.

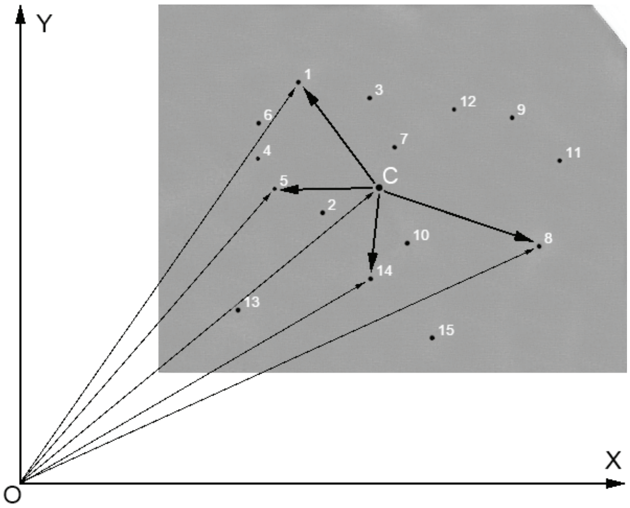

Fig. 2. The graph of building radius – vectors $\overrightarrow{on}$, $\overrightarrow{oc}$, $\overrightarrow{cn}$.

The aim of this article is to review and approbation algorithm of the method of indexing of lauegram and determining the crystallographic orientation of grain in relation to the main directions in the crystal and Shmidt`s factor for all glide systems.

Results and discussion

The algorithm of the method of indexing of lauegram and determining the crystallographic orientation of grain in relation to the main directions in the crystal and Shmidt`s factor for all glide systems.

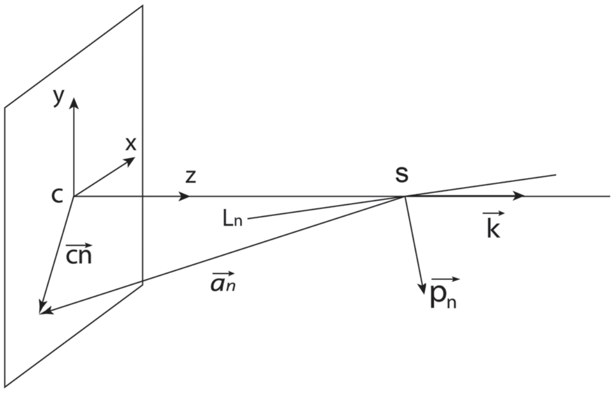

Fig. 3. The graph of building single vectors of normal $\vec{P}_n$ to reflecting planes: S- sample; Ln – reflecting plane, $\vec{k}$ – is unit vector of the axis Z.

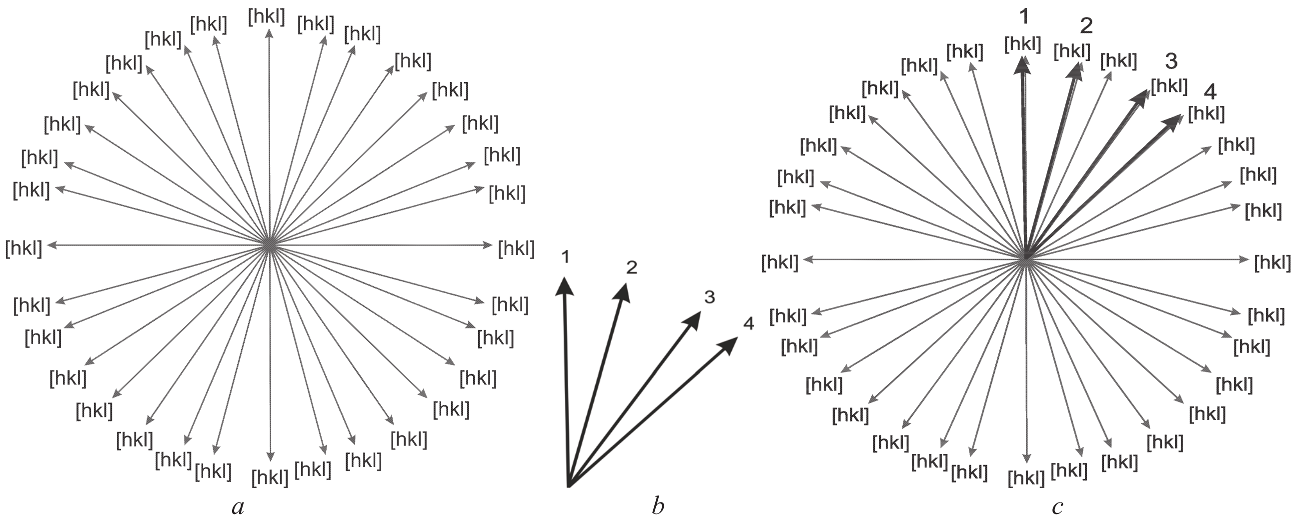

Fig. 4. Single radius – vector of normals to crystallographic planes with given indexes $\vec{P}_{hkl}$ (a), reflecting planes $\vec{P}_n$ (based on data from lauegram) (b) and results of their comparison (c).

Above is shown the description of computer method, which allows in automatic mode to index lauegram, determine crystallographic orientation of the sample relative to the main directions in the crystal and the number of Shmidt`s factor for all glide systems.

The preparatory stage of this method is scanning of obtained lauegram, its editing to determine weak reflexes and storing it in one file. In figure 1, as example, the lauegram before (a) and after (b) editing is shown.

Further, the orthogonal system of numbers is presented of axis XYZ, where X – is direction of axis of stretching (the bottom part of the film), Z – is the direction, opposite the X-Ray bunch and the numbering of the reflexes of lauegram (n) and its center (c) is made (Fig.2).

The next stage is determining the radius – the vector of laue spots $\overrightarrow{on}$ and $\overrightarrow{oc}$, the vectors $\overrightarrow{cn}$ ($\overrightarrow{cn} = \overrightarrow{on} - \overrightarrow{oc}$), and their coordinates (Fig. 2) and determining single vectors of normals to surrounding planes ($\vec{P}_n$) for laue spots. The diagram of this determining is shown in figure 3.

From the figure we can see that if the distance sample–film (H) is known, the unit vector of normal to reflecting plane Ln can be determined by the following method:

$$\vec{P}_n = \frac{1}{\left|\frac{\overrightarrow{a_n}}{a_n} + \vec{k}\right|}\left(\frac{\overrightarrow{a_n}}{a_n} + \vec{k}\right), \qquad (1)$$

where $\overrightarrow{a_n} = \overrightarrow{cn} - H \cdot \vec{k}$, $\vec{k}$ – is unit vector of the axis Z, n – is the number of laue spots.

Determination of similar unit radiuses-vectors for planes with known indexes (hkl) for researched crystal is made by the formula:

$$\vec{P}_{hkl} = \frac{1}{\sqrt{h^2 + k^2 + l^2}} \begin{bmatrix} h \\ k \\ l \end{bmatrix}, \qquad (2)$$

where h, k, l = 0, ±1,±2,…,±n.

The last stage of this method is graphic building of unit radiuses – vectors $\vec{P}_n$ and $\vec{P}_{hkl}$ (Fig. 4.a, b, c) with common center.

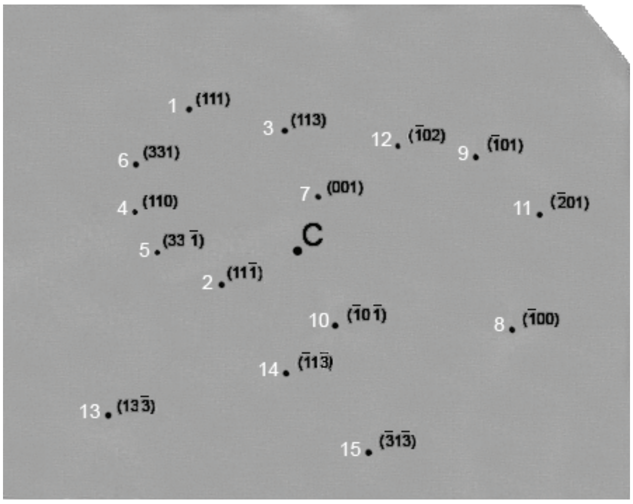

Fig. 5. Results of indexing of lauegram.

Computer program allows to find optimal common place of specters of vectors $\vec{P}_n$ and $\vec{P}_{hkl}$ in the space, which leads to co-inciding of vectors $\vec{P}_n$ with part of vectors $\vec{P}_{hkl}$, so that it allows each laue spot to allocate indexes to reflecting plane (hkl) (Fig. 5).

If on the lauegram there are no reflexes from crystallographic planes, normals, to which they are the main crystallographic directions, they are determined based on the results of indexing of the lauegram, taking into account known angle correlation in crystalline bar between directions. Determining of vectors $\vec{P}_{100}$, $\vec{P}_{110}$, $\vec{P}_{111}$ in the system X,Y,Z, connected to the crystal allows to determine angle correlation between X,Y,Z and $\vec{P}_{100}$, $\vec{P}_{110}$, $\vec{P}_{111}$ (table 1).

Table 1

	[100]	[110]	[111]
X	32	24	20
Y	19	28	31
Z	24	35	23

Finally, using the correlation for determining Shmidt`s factor (m = cosα·cosφ, where α – is the angle between direction of axis of stretching and glide plane, φ – angle between normal to glide plane and direction of axis of stretching) (Fig. 6) can be determined Shmidt`s factor for all glide systems (table 2): $(\bar{1}11)[0\bar{1}1]$, $(\bar{1}11)[101]$, $(\bar{1}11)[\bar{1}\bar{1}0]$, $(\bar{1}\bar{1}1)[1\bar{1}0]$, $(\bar{1}\bar{1}1)[101]$, $(\bar{1}\bar{1}1)[011]$, $(111)[\bar{1}01]$, $(111)[0\bar{1}1]$, $(111)[1\bar{1}0]$, $(1\bar{1}1)[\bar{1}01]$, $(1\bar{1}1)[011]$, $(1\bar{1}1)[\bar{1}\bar{1}0]$.

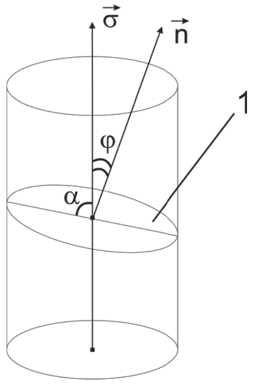

Fig. 6. The graph of determining Shmidt`s factor: 1 – glide plane (one of the planes {111}); $\vec{\sigma}$ – axis of stretching of sample; $\vec{n}$ – normal to the glide plane, φ – angle between the normal to the glide plane and direction of axis of stretching, α – angle between the direction of the axis of stretching and glide plane.

It should be mentioned, that offered method does not require difficult process of building and using stereographic planes.

Table 2

Glide systems	**1**	**2**	**3**	**4**	**5**	**6**
Shmidt`s factor	0,46	0,37	0,35	0,30	0,27	0,21
Glide systems	**7**	**8**	**9**	**10**	**11**	**12**
Shmidt`s factor	0,17	0,16	0,09	0,06	0,05	0,01

Conclusion

1. Computer method is developed, which allows to index lauegram, determine crystallographic orientation of monocrystallines (separate grains of polycrystalline) relative to the main directions in the crystal and Shmidt`s factor for all glide systems.

2. The main algorithm of this program is determining and building the system of single radiuses – vectors of normal to reflection planes (based on data of lauegram), system of similar vectors for crystals with known orientation and combination of their centers.

3. Computer program allows to determine the optimal common place of specters of these vectors in the space, which leads to maximal co-incidence of vectors, so that it allows to each laue spot to allocate indexes to reflection plane.

1. Гинье А. Рентгенография кристаллов, 1963.
2. Уманский Я. С., Скаков Ю.А. , Иванов А.Н., Расторгуев Л.Н. Кристаллография, рентгенография и электронная микроскопия, Металлургия, 1982.
3. Миркин Л.И. Рентгеноструктурный анализ. Индицирование рентгенограмм, 1981.
4. Бадиян Е.Е., Тонкопряд А.Г., Шеховцов О.В., Шуринов Р.В. Вісник ХНУ, № 558, серія «Фізика», вип. 6, 2002, с. 91 – 94.

Вісник ХНУ, № 1158, серія «Фізика», вип. 22, 2015. с. 35-38

PACS: 61.72.Cc, 61.72.Mm, 61.72.Ff, 61.72.Hh, 68.35.Gy

The technique of simultaneous investigation of the laws of occurrence and development of rotational and translational modes in situ during plastic deformation of the samples

K.S. Kazachkova, R.V. Shurinov, E.E. Badiyan

Department of Physics, Department of Solid State Physics,
Kharkov National University, 4 Svoboda Sq., 61077 Kharkov, Ukraine
Evgeny.E.Badiyan@univer.kharkov.ua

The described technique, allowing in situ in the process of plastic deformation of samples at the same time monitor the emergence and development of translational and rotational modes. The first method uses a technique of producing color cards orientation and imaging them colors. In the second - the effect of laser diffraction on quasi-periodic deformation relief in the form of slide steps. The color orientation maps allow to determine the characteristics of the substructure with a linear resolution ~ 1 micron and angular ~ 10 seconds.

Using the laser technique makes it possible is to follow the emergence and development of sliding and determine characteristics such as sliding direction and its change in the deformation of the sample, the minimum distance between slip lines characterizing the intensity of slip and slip lines degree of curvature that characterizes the strengthening investigated sample.

Keywords: color orientation map, rotational mode, translational mode, the plastic deformation.

Описана методика, що дає можливість in situ в процесі пластичного деформування зразків одночасно стежити за виникненням і розвитком ротаційної і трансляційній мод. У першому випадку використовується методика отримання кольорових орієнтаційних карт і візуалізації на них відтінків кольорів. У другому - ефект дифракції лазерного випромінювання на квазіперіодичному деформаційному рельєфі в вигляді сходинок ковзання. Кольорові орієнтаційні карти дозволяють визначити характеристики субструктури з лінійною роздільною здатність ~ 1 мк, і кутовим ~ 10 сек.

Використання лазерної методики дає можливість є простежити за виникненням і розвитком ковзання і визначити такі характеристики як напрямок ковзання і його зміна в процесі деформування зразка, мінімальна відстань між лініями ковзання, що характеризує інтенсивність розвитку ковзання, а також ступінь викривлення ліній ковзання, що характеризує зміцнення досліджуваного зразка.

Ключові слова: колірні орієнтаційні карти, ротаційна мода, трансляційна мода, пластична деформація.

Описана методика, позволяющая in situ в процессе пластического деформирования образцов одновременно следить за возникновением и развитием ротационной и трансляционной мод. В первом случае используется методика получения цветовых ориентационных карт и визуализации на них цветовых оттенков. Во втором – эффект дифракции лазерного излучения на квазипериодическом деформационном рельефе в вид ступенек скольжения. Цветовые ориентационные карты позволяют определить характеристики субструктуры с линейным разрешением ~ 1 мк, и угловым ~ 10 сек.

Использование лазерной методики позволяет проследить за возникновением и развитием скольжения и определить такие характеристики как направления скольжения и его изменение в процессе деформирования образца, минимальное расстояние между линиями скольжения, характеризующее интенсивность развития скольжения, а также степень искривления линий скольжения, характеризующих упрочнение исследуемого образца.

Ключевые слова: цветовые ориентационные карты, ротационная мода, трансляционная мода, пластическая деформация.

Introduction

It is well known that the mechanical properties of crystalline samples are structurally highly sensitive. The mechanical characteristics of the sample under study depend not only on the initial structure and substructure, but also on the nature of change in the process of plastic flow. Plastic deformation of crystalline samples is characterized by two modes - translational and rotational. In the first case, as a result of plastic deformation of the elementary event - slip dislocations on the sample surface at the exit site of dislocation occurs in the form of steps relief whose shape, size, number, orientation, and other parameters can judge and the mechanism of occurrence of plastic deformation. Similarly, in the second case, when the plastic deformation is characterized by a rotary mechanism, there is a reversal of certain parts of the sample, which can significantly change not only share in the plastic deformation of the translation mode, but also to make an independent contribution (in some cases substantial) in the plastic deformation of the entire sample .

In recent years, developed a number of techniques [1, 2, 3, 4], that allow using color maps to determine the orientation and orientation substructural characteristics of the sample and monitor in situ for their change in the course of its deformation. Using the method of imaging hues [5, 6] it is possible to determine the parameters of the linear substructural ~1 micron resolution and angular ~10 seconds.

The traditional method of determining the translational component of plastic deformation based on a study of the strain relief in the form of steps slip occurring on the polished surface of the sample [7].

Experimental studies patterns of plastic deformation of polycrystalline samples made in recent years have shown that it is impossible not only to determine and predict the occurrence and sequence of deformation modes, thus characterize a pattern of plastic deformation in the whole sample. The main reason is the lack of experimental techniques which allow the process of plastic deformation synchronously follow the emergence and development of shear and rotation deformation modes.

The simultaneous use methods of obtaining color orientation maps and thus define substructural characteristics and their changes in the process of deformation of the sample to the entire working surface of the sample and methodology of the study of deformation structures in the form of sliding steps will enable to trace the origin and development of different modes of plastic deformation, to determine the role of each of them in the plastic deformation of the whole of the sample and eventually to describe the mechanism of plastic deformation of the specimen.

Aim of this study was to develop a technique for the simultaneous investigation of translational and rotational fashion plastic deformation of the sample in situ during its deformation.

Description of the experimental setup

Scheme of the experimental setup is shown in Fig. 1. On the base plate (3) of the deforming device at different sides test sample installed two devices: one for registration color orientation maps, another - for the registration in situ during the plastic deformation of the diffraction pattern formed by diffraction of the laser radiation on elements of the strain relief arising on the surface of the sample during its plastic deformation. For experimental studies it is necessary that one of the working surfaces of the sample (1) was polished, to identify the strain relief on it and recording the diffraction patterns on this relief by laser using a web camera (4), the other for the purpose of chemically etched identifying on it a quasiperiodic relief with which the interaction of white light leads to the effect of diffraction of [2] and, consequently, to the appearance of color orientation maps recorded by using a Web camera (10). Due to the fact that the size of the laser beam on the sample surface are insignificant (2×2 mm^2) in the installation has a device (8) for scanning the laser beam across the sample surface. The scanning speed was 10 mm / sec. Special screen (6) is transparent to the laser radiation (λ=630 nm) allows to record diffraction patterns with a digital camera. Voltage measuring deformation unused specially made elastic element (9) with adhesive on it, and strain gauges connected in a bridge circuit. The deformation of the sample was carried out using a special loading device, which was the ultimate force ~5 kg. The rate of deformation of the sample - $\sim 10^{-5}$ c^{-1}. All information about the sample in the form of color orientation maps, laser diffraction patterns and the deformation curve in coordinates $\sigma = \sigma(\varepsilon)$ synchronous recorded with a PC with a period of 0,01 seconds.

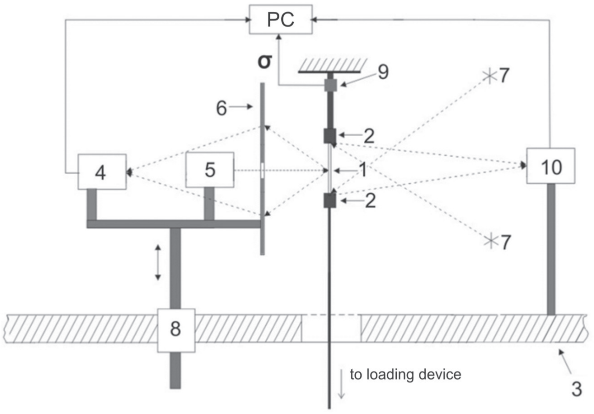

Fig. 1. The experimental setup.

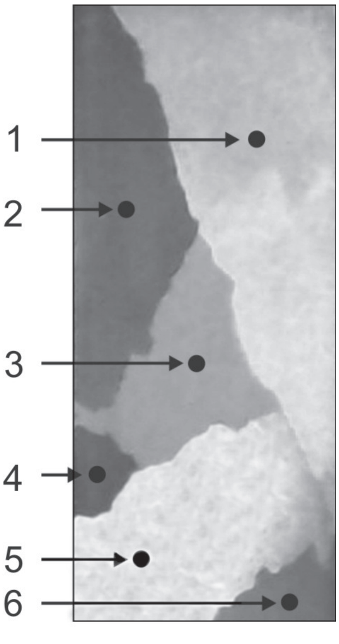

Fig. 2. The color orientation map of the surface of the individual grains of the polycrystalline sample aluminum after deformation by 17%.

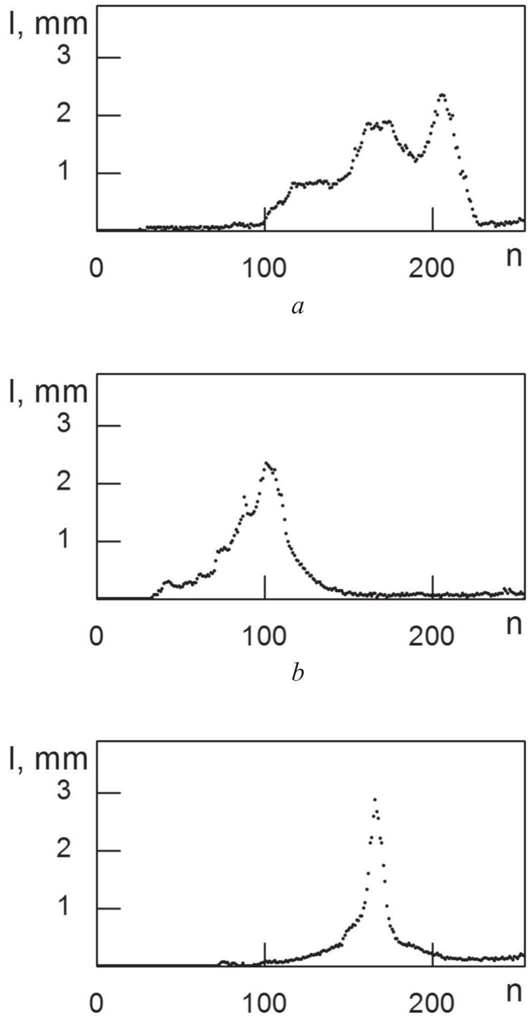

a b c

Fig. 3. Distribution of the elements of the substructure in various size grains of a polycrystalline sample after 17% deformation (a - grain 1, b - grain 2, c - 3 grain).

Research results and their discussion

As an example, in Fig. 2. Bring the color orientation map of the surface of the individual grains of a polycrystalline sample of aluminum after deformation by 17%.

Color image of the surface of the grains uniform, which indicates the presence in the sample of the substructure elements [3]. Fig. 3. provide information on the distribution of elements of the substructure for the size of the sample before and after the deformation of 17%, obtained using the method of visualization [5] The colors in the COM. From Fig. 3 that when the deformation of 17% in the 1-st (a) and 2-nd (b) the grain is its division into blocks with a decrease in the average block size, and expanding the range of their disorientation. In the 3-rd grain (c) in the process of deformation of the sample, and the average size of the block range of misorientation not changed. This grain is in the process of plastic deformation unfolding as a whole.

Distribution curves subgrain size and crystallographic orientation to third grain deformation to the sample and after deformation of 17% are shown in Fig. 3 c.

Thus, effects rotation of the first and second grain manifested in a change in orientation of the sample during deformation substructure elements, their crushing and spreading of these changes, and the third average grain size subgrain disorientation and their spectra remain practically unchanged. In the process of deformation of the grain subgrain orientation change occurs, leading to a change in the orientation of the grain as a whole.

Here, in Fig. 4 shows typical laser diffraction patterns obtained from the grains mentioned above, after the deformation of the sample by 17%.

For grain 1 with a well-developed structure of a rotary slip traces are found almost, so there is no diffraction pattern (Fig. 3 a). On the surface of grain 3 after the deformation of the sample at 17% deformation relief formed in the form of steps at the exit site slip dislocations. This is evidenced by the form of the diffraction pattern resulting from the interaction of the laser beam with the relief (Fig. 3 c). Analysis color maps of the orientation obtained from the surface of the grain, showing that the effect of grain in the crushing process of deformation of the sample takes place.

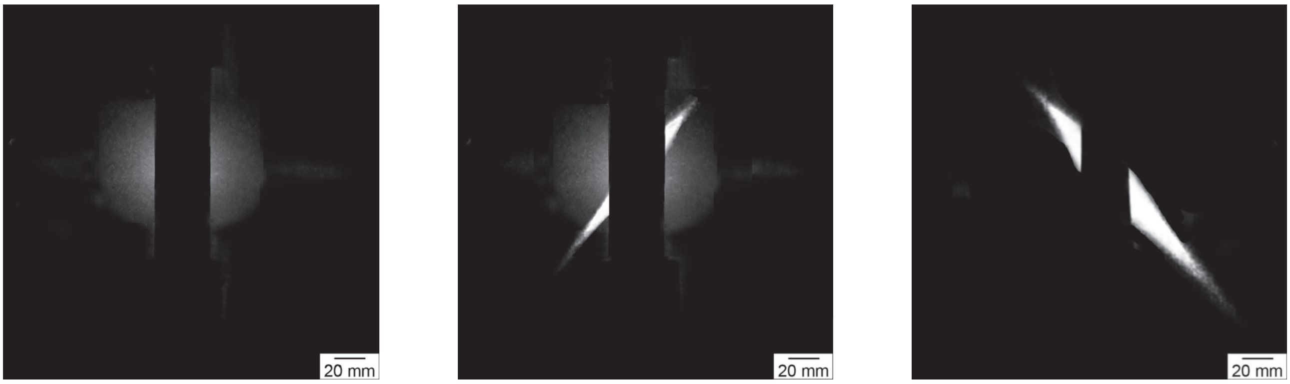

a b c

Fig. 4. Laser diffraction patterns from the surface of the grains of the polycrystalline sample 1,2,3 after deformation by 17%.

Conclusions

1.The technique allows to simultaneously investigate the emergence and development of translational and rotational deformation modes of the sample in situ in the process of deformation has been proposed.

2.Using a laser technique [8] allows not only to register the occurrence of strain relief, but also the character of its development in the process of deformation of the sample. By the form of the diffraction pattern can determine the direction of the slide and the change in the deformation process. The shape and size of the diffraction pattern (in view of its reflexes) can be defined such substructural characteristics of plastic flow [8] as the minimum distance between slip lines, characterized by intensive development of plastic deformation and the character of the curvature of the slip lines defining the pattern of hardening of the sample.

1. Patent 89743 UKRAINE, the IPC G01B 11/16. E.E. Badiyan, A.G. Tonkopryad, O.V. Shekhovtsov, R.V. Shurinov; The applicant and patent owner V.N. Karazin KNU. - № a 2009 06455; appl. 22.06.09; publ. 25.02.10, Bul. №4.
2. E.E. Badiyan, A.G. Tonkopryad, O.V. Shekhovtsov, R.V. Shurinov. Functional Materials, 3, 3, 411, 2006
3. E.E. Badiyan, A.G. Tonkopryad, O.V. Shehovtsov, R.V. Shorinov, T.R. Zetova. Inorganic Materials, 15, 1663 (2011).
4. E.E. Badiyan, A.G. Tonkopryad, O.V. Shehovtsov, R.V. Shorinov, T.R. Zetova. Factory Laboratory. Diagnosis materials, 76, 8, 34, (2010).
5. Patent 104249 UKRAINE, the IPC (2013.01), G01N 21/00, G01N 33/20 (2006.1). E. E. Badiyan, A. G. Tonkopryad, O. V. Shekhovtsov, R. V. Shurinov, T. R. Zetova, K. S. Kazachkova; The applicant and patent owner V.N. Karazin KNU. – № a 2012 14845; appl. 24.12.12.; publ.10.01.14, Bul. №1.
6. E. E. Badiyan, A. G. Tonkopryad, O. V. Shekhovtsov, R. V. Shurinov, T. R. Zetova, K. S. Kazachkova. Functional Materials, 21, 3, 307 (2014).
7. G.A. Malygin. Solid State Physics, 43, 2, 248 (2001).
8. E. E. Badiyan, A. G. Tonkopryad, O. V. Shekhovtsov, R. V. Shurinov, T. R. Zetova, K. S. Kazachkova. Functional Materials, 22, 3 (2015).

Вісник ХНУ, № 1158, серія «Фізика», вип. 22, 2015. с. 39-41

пакс

Material fast transport in nano-crystals of (AB_{n-x})-type ionic compounds

Y.I. Boyko, V.V. Bogdanov

Karazin Kharkiv National University
yuri.i.boiko@univer.kharkov.ua
bogdanov@karazin.ua

The effectiveness of material transport by the mechanism of single-file diffusion in comparison with the conventional mechanism of the classical diffusion of atoms is discussed. The conditions under which the single-file diffusion can provide fast mass transport are considered. The analysis and assessment made indicate that the diffusion of atoms along one-dimensional vacancy clusters formed in the (AB_{n-x})-type ion nano-crystals, may have a much faster mass transport compared to transport by the classical diffusion mechanism of atoms, which is defining for massive crystals.

Keywords: single-file diffusion, one-dimensional vacancy clusters, (AB_{n-x})-type ion nano-crystals.

Обговорюється ефективність транспорту речовини механізмом однофайлової дифузії у порівнянні з механізмом звичайної класичної дифузії атомів. Розглянуто умови, за яких однофайлова дифузія може забезпечити прискорений масоперенiс. Проведений аналіз та оцінка свідчать про те, що дифузія атомів вздовж одномірних вакансійних кластерів, що формуються в іонних нано-кристалах типу AB_{n-x}, може характеризуватися значно швидшим перенесенням речовини порівняно з перенесенням звичайним класичним механізмом дифузії, який є визначальним для масивних кристалів.

Ключові слова: однофайлова дифузія, одномірні вакансійні кластери, іонні нано-кристали типу AB_{n-x}.

Обсуждается эффективность транспорта вещества механизмом однофайловой (одноканальной) диффузии по сравнению с механизмом обычной классической диффузии атомов. Рассмотрены условия, при которых однофайловая диффузия может обеспечить ускоренный массоперенос. Проведенный анализ и сделанная оценка свидетельствуют о том, что диффузия атомов вдоль одномерных вакансионных кластеров, формирующихся в ионных нано-кристаллах типа AB_{n-x}, может характеризоваться значительно более быстрым переносом вещества по сравнению с переносом обычным классическим механизмом диффузии, который является определяющим для массивных кристаллов.

Ключевые слова: однофайловая диффузия, одномерные вакансионные кластеры, ионные нано-кристаллы типа AB_{n-x}.

Introduction

Nano-crystals – are the crystals with the linear size of $\leq 1-10$ nm. As the experimental and theoretical studies demonstrated the nano-crystals physical properties are radically different from those of usual size scale crystals [1–3].

The special properties of nano-crystals are caused by the fact that in comparison with bulk crystals the very important changes occurs in the nano-crystals structure and in its electron energy spectrum. The main reason for these changes is the fact that the surface atoms of crystal and the atoms of subsurface layer by thickness of $\delta \approx 3a$ (a – the lattice parameter) have the number of nearest neighbors (the number of particles of the first and of the subsequent coordination spheres) reduced in comparison with those in bulk of crystal. An elementary estimate shows that if the crystal size is $d \approx 10\delta \approx 10$ nm, the number of atoms that are “feeling” the absence of half of the space is $\approx 50\,\%$ of the total atoms number.

The natural consequence of change in the number of surrounding atoms (the coordination number change) is that the “surface” and “near-surface” atoms are have to displace to new positions. This changes their oscillations parameters, charge state, polarization and thus changes the nature of their interaction. In (AB_{n-x})-type ionic crystals due to changes in the valence of ions and due to additional polarization in the surface layers of nano-crystals the specific transitional structures or so-called layered lattices are formed [4]. These structures are characterized by the appearance of a covalent component of the chemical bond between the layers of ions. Herewith very important is the fact that the rearrangement of the crystal lattices is accompanied by the crystal stoichiometry violation.

So formation of a layered crystal structure entails a change in valence of the ions. This in turn results to appearance of the excess (non-stoichiometric) vacancies in the corresponding sub-lattice due to the necessity to satisfy the condition of electrical neutrality of the crystal as a whole. Conglomerations of the stoichiometric vacancies form one-dimensional channels (clusters), which in the case of nano-sized crystals can penetrate through them. A typical example of ionic crystals in which by decrease their linear size to the value of ≤ 10 nm were experimentally observed all the above mentioned changes in the structure, are the crystals of cerium oxide CeO_2 [5, 6].

One-dimensional vacancy clusters penetrating nano-crystal cause the possibility of an unconventional material transport mechanism – the mechanism of so-called single-file diffusion [7, 8].

In this work, we assessed the efficiency of material transport by the mechanism of single-file diffusion in comparison with the conventional mechanism of the classical diffusion of atoms, which is determining for the massive crystals. The conditions under which the single-file diffusion can provide fast mass transport are considered.

Classical and single-file diffusion of atoms in crystals

It is known that the basis of description of the traditional (classical) mechanism of atoms diffusion in crystals is the model of random walks. According to this model, atoms jumps during their thermal migration occur independently from each other, i. e. there is no correlation between them: next jump of the atom does not depend on what was the previous jump. All directions of the subsequent jump are equiprobable [9]. In this model, the radius-vector of the average displacement of a large number of atoms equal to zero: $\langle X(t)\rangle = 0$, and their mean square displacement is not zero: $\langle X^2(t)\rangle \neq 0$. For one-dimensional diffusion of atoms in crystals in the framework of the classical model the Einstein – Smoluchowski ratio is valid:

$$\langle X^2(t)\rangle = 2Dt. \qquad (1)$$

Here D – diffusion coefficient of atoms characterizing the material transport efficiency, t – time of diffusion.

It should be noted that if one compares the distance of the atom diffusion displacement from an initial position

$$L_d = \sqrt{2Dt} \qquad (1a)$$

with a total length L, which it passes during the same time, it appears that $L_d \ll L$. This inequality indicates the low efficiency of random walks (of chaotic motion) by diffusion mass transferring mechanism and explains why so small the penetration depth of the diffusing material is even after long diffusion annealing.

In the case of the single-file diffusion unlike the above-described mechanism, thermal chaotic migration of atoms is limited to "one-dimensional" channel in which an atom can move in one direction only and diffusing particles can not bypass each other. The mean square displacement for this diffusion mechanism is described by the following formula [6]:

$$\langle X^2(t)\rangle = 2Ft^{1/2}, \qquad (2)$$

where F – mobility – parameter characterizing the movement of atoms in the single-file diffusion. By itself, the parameter F can't be used to characterize the effectiveness of the mass transport. However, if we use the random walk model applied to a single particle that is moving in one direction and that is not experiencing any interaction with other particles (an analogue of the single-channel or single-file diffusion), the mean square displacement can be described by the following equation [10]:

$$\langle X^2(t)\rangle = \lambda \langle X(t)\rangle. \qquad (3)$$

$\langle X(t)\rangle$ – the average displacement of atom in one dimensional channel, λ – the average distance between neighboring diffusing atoms. Considering that in the case of single-file diffusion: $\langle X(t)\rangle = \sqrt{2D_{sf}t}$ (similarly to the relation (1a)), and using (2) we have:

$$D_{sf} = 2F^2/\lambda^2. \qquad (4)$$

D_{sf} parameter has the dimension of the diffusion coefficient and can be used to characterize the effectiveness of the atoms transport by the single-file diffusion mechanism.

Comparative evaluation of effectiveness of the considered above two diffusion mechanisms of atoms in crystals

For a quantitative estimation of the effectiveness of mass transport by the classical diffusion mechanism and by the single-file diffusion mechanism let's consider the dimensionless ratio:

$$\chi = D_{sf}/D = 2F^2/\lambda^2 D. \qquad (5)$$

Substituting in the equation (5) reasonable values of quantities: $\lambda \approx 0{,}5$ nm, $D \approx 10^{-12}\, m^2/s$ (for ionic crystals at the premelting temperatures [9]), as well as the experimentally found value of the mobility factor: $F \approx 10^{-12}\, m^2/s^{1/2}$ [6], we have: $\chi \approx 10^7$.

Conclusions

The analysis and assessment made indicate that the diffusion of atoms along one-dimensional vacancy clusters formed in the (AB_{n-x})-type ion nano-crystals, may have the much faster mass transport compared to the transport by the classical diffusion mechanism of atoms, which is defining for massive crystals.

In fact, this result suggests that in the case of single-file diffusion the length of the diffusion path of atom along the vacancy cluster L_d approaches the value of its total path L, i. e. $L_d \approx L$. As it already was mentioned, for the classical diffusion of atoms based on the random walk model the inequality $L_d \ll L$ takes place.

The described effect of accelerated material transport in the ionic nano-crystals, in the structure of which there are vacancy clusters, must occur in the greater extent, the smaller is the homologous temperature, i.e. the smaller is the value of D; also the more the density of diffusing ions is in cluster, i.e. the smaller is the value of λ (see Relation (5)).

1. S. A. Nepijko, Fizicheskie svojstva malyh metallicheskih chastits, Naukova dumka, Kiev, (1985), 246 s.
2. Yu. I. Petrov, Fizika malyh chastits, Nauka, Moskva, (1982), 275 s.
3. I. D. Morohov, L. I. Trusov, V. N. Lapovok, Fizicheskie Yavleniya v ultradispersnyh sredah, Energoatomizdat, Moskva, (1984), 223 s.
4. R. Evans, Vvedenie v kristallohimiyu, Goshimizdat, Moskva, (1948), 367 s.
5. F. Esch, S. Fabris, L. Zhou and al., Science, v. 309, P. 752 – 755, 2005.
6. K. Hahn, J. Karger, V. Kukla, Physical Review Letters, v. 76, № 15, P. 2762 – 2765, 1996.
7. S. Nedea, A. Jansen, J. Lukkien, P. Hilbers, Physical Review, v. E -67, P. 1 – 8, 2003.
8. R. Macey, R. Oliver, Biophysical Journal, v. 7, P. 546 – 554, 1967.
9. B. S. Bokshtein, S. Z. Bokshtein, A. A. Zhuhovitskij, Termodinamika i kinetika diffusii v tverdyh telah, Metallurgiya (1974), 280 s.
10. K. Hahn, J. Karger, J. Phys. A, v. 28, P. 3061 – 3067, 1995.

Вісник ХНУ, № 1158, серія «Фізика», вип. 22, 2015. с. 42-44

УДК 539.4
PACS: 62.20.F-

Reorientation in alkali-halide single crystals under mechanical stress in an initial stage of high-temperature creep

V.I. Kibets[1], O.I. Kovtun[2], D.V. Matsokin[1], V.P. Matsokin[1], I.N. Pakhomova[1]

[1]V. Karazin Kharkov National University,
4 Svobody sq., 61022, Kharkov, Ukraine
e-mail: matsokin@univer.kharkov.ua
[2] Physikalisches Institut der Universität Heidelberg,
Im Neuenheimer Feld 226, 69120 Heidelberg, Germany

Structural changes in KCl and NaCl single crystals were investigated at the initial stage of the high-temperature creep during impeded motion of dislocation in easy-slip systems. The main features of the formation of dislocation structures were studied at the initial stage of rotational deformation, marked by the development of reorientation bands in single crystals. The subsequent process of rotational deformation was also analyzed, as the reorientation bands enlarge and merge and hence, single crystals become polycrystals.

Keywords: dislocation, rotational deformation, single crystal, polycrystal, reorientation band, kink band.

Досліджено структурні зміни в монокристалах KCl і NaCl на початковій стадії високотемпературної повзучості в умовах, коли в системі легкого ковзання рух дислокацій ускладнено. Вивчено особливості формування дислокаційних структур на самому початковому етапі ротаційної деформації, коли зароджуються смуги переорієнтації в окремих областях монокристала, зростання і злиття яких призводить до перетворення монокристалла в полікристал.

Ключові слова: дислокації, ротаційна деформація, монокристал, полікристал, смуги переорієнтації, смуга скиду.

Исследованы структурные изменения в монокристаллах KCl и NaCl на начальной стадии высокотемпературной ползучести в условиях, когда в системе легкого скольжения движение дислокаций затруднено. Изучены особенности формирования дислокационных структур на самом начальном этапе ротационной деформации, когда зарождаются полосы переориентации в отдельных областях монокристалла, рост и слияние которых приводит к превращению монокристалла в поликристалл.

Ключевые слова: дислокации, ротационная деформация, монокристалл, поликристалл, полосы переориентации, полоса сброса.

The transformation of single crystals to polycrystals due to reorientation of large areas during rotational deformation can occur at different load regimes in crystals with different bond types and unit cell types [1, 2].

What happens at the initial stage of reorientation band formation is unclear. Simple structure of reorientation band consists of two edge dislocation walls with antiparallel Burger's vectors [3, 4]. This structure indicates an already formed kink band, but not the process of its forming. The only explanation of such structure is a so-called "mechanical polygonisation," which sometimes occurs during the low-temperature deformation [3]. This model has a defect: the probability that such dislocations form a band is rather small.

The reorientation of crystal areas causes the significant decrease of internal stresses. The formation of reorientation band effects a dip on strain hardening curve $\sigma(\varepsilon)$. However, the formation of reorientation bands at the initial stage of fragmentation during the rotational deformation is hardly studied [4]. The purpose of this investigation was to explore a surface relief forming of single crystals at an initial stage of high-temperature creep, forming of dislocation structure at these conditions and influence of such dislocation structures on the rotation deformation.

In this paper, the structural changes in single crystals with NaCl-type lattice are investigated at the initial stage of reorientation during high-temperature creep when dislocation glide (motion) is impeded.

Experimental technique

The performed experiments used alkali halide single crystals NaCl and KCl shaped as rectangular prisms with an initial dislocation density $\rho \sim 10^5\ \text{cm}^{-2}$ and average linear size of the blocks $l \cong 10^{-3}\ \text{m}$.

Single crystals were compressed uniaxially in the direction <111> at temperature range from 0.6 to 0.92 T_{melt} in the creep mode. Because of the orientation of the compression, the reduced shear stresses in all primary slip

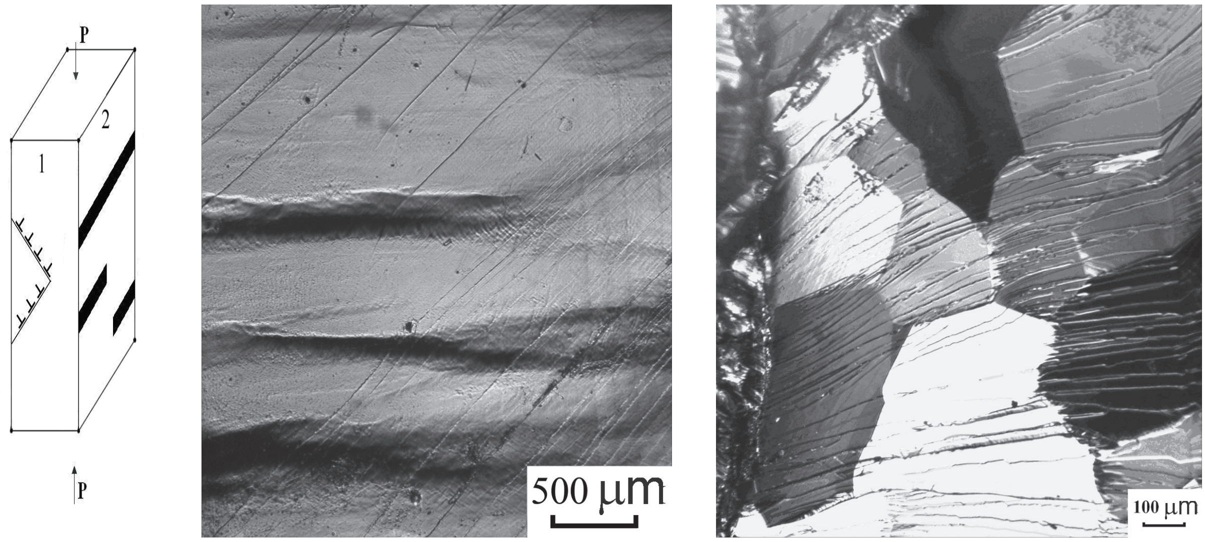

a *b* *c*

Fig 1. a – scheme of deformation; b – the initial stage of the reorientation bands formation in NaCl. T=625°C, $\sigma=0.6$MPa, t=5 min, c – KCl T=650°C, $\sigma=0.8$MPa, t=30 min.

systems $\{110\}<110>$ were zero.

Substructure evolution

The dislocation structure was visualized by selective etching.

Single crystals became polycrystals at high temperature and high level of external stresses during creep at relative deformation $\varepsilon > 0.1$ due to the formation of sets of reorientation areas [5, 6]. The angles between these areas reach several degrees.

During the initial stage of deformation of single crystal prisms the reorientation bands started to form on the crystal sides which were parallel to the compression vector and have greater area (surface "2" on Fig 1a).

Initially the reorientation bands were perpendicular to the direction of external uniaxial compression. Before forming of the reorientation band, the surface relief became striped ("crumpled"). With the increase of deformation the reorientation bands became wider, merged together and changed their orientations (Fig 1c). As a result of deformation, the dislocation structures of single crystals on surfaces "1" and "2" were significantly altered (Fig. 1 a).

On surface 1, one can see the set of etching pits forming the rectangular cells (Fig 2a). The orientation of etch pits rows is <110>. Hence, they denote the formation of the low-angle boundaries composed of edge dislocations. Two sets of dislocation boundaries indicate that the deformation process is provided by dislocations of two perpendicular slip systems $\{110\}$. During deformation the dislocation structures transform into the typical for the high temperature creep block structures with big blocks and arbitrarily oriented block boundaries. The arbitrary orientation of boundaries indicates the presence of dislocations of two

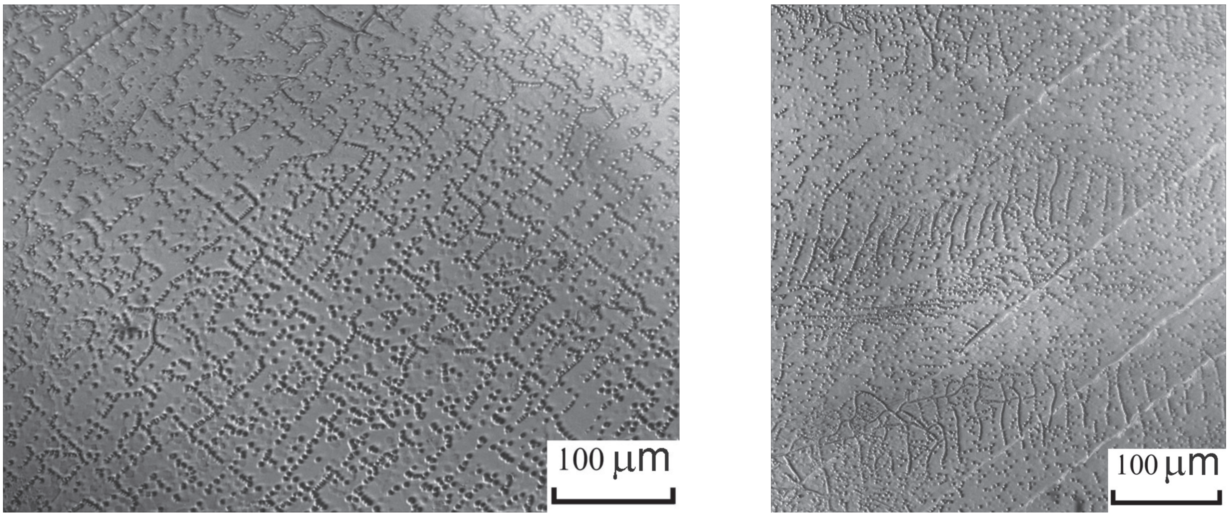

a *b*

Fig. 2. Dislocation structures of NaCl single crystals, T=625°C, $\sigma=0.6$MPa, t=5 min, a – surface "1", b – surface "2".

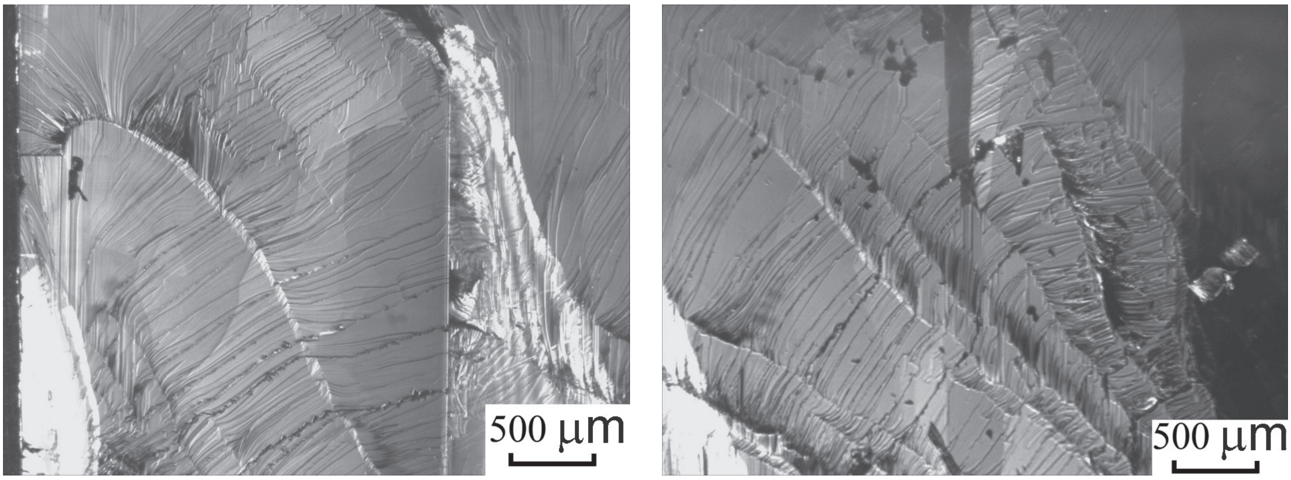

a *b*

Fig. 3. The cleavage steps on surface “2” in NaCl single crystal. T=600°C, $\sigma = 0.4$MPa, t=30 min..

slip systems in each boundary.

On the surface of type “2,” the dislocation structure is quite different. Along with the chaotically distributed dislocations, there are periodic rows of etch pits in <100> direction. Such areas indicate reorientation bands beginning to form. These periodic rows of etch pits consist of screw dislocations. This fact is confirmed by three experimental evidences. The first of which is the direction of these short rows. Second, these rows disintegrated into chaotically distributed dislocations, as pile-ups of screw dislocations with the same Burger’s vectors are unstable. Third, the analysis of cleavage steps on surface of deformed crystal confirms the presence of screw dislocations.

The alkali-halide crystals with NaCl-type lattice are such, that if we apply external concentrated force, the crystal cleaves out along the planes with minimum surface energy {100}. Since the splitting forms two free surfaces, it requires high energies. Thus the cleavage cannot instantly occur in the whole crystal. The cleavage spreads from one point to another in the form of crack, which starts in the place of the force application.

In a single crystal without dislocations, the cleavage surfaces have to be perfectly smooth on atom level. In real single crystals, the cleavage surface consists of the system of cleavage steps formed during the crack propagation through the rows of screw dislocations. If the crack crosses the twist boundary consisting of at least two screw dislocation systems with different Burgers vectors, numerous cleavage steps appear. Such cleavage steps can merge, thus forming either higher steps or merging creeks that spread in the direction of crack propagation.

If after the crack has crossed the boundary and only orientation of cleavage steps is changed, the nonappearance of new steps implies that this boundary is the tilt boundary, consisting of edge dislocations. An increased amount of cleavage steps indicates the twist boundary consisting of screw dislocations. In all crystals we can see both types of dislocations, particularly in the areas of reorientation band formation (Fig. 3).

Conclusions

Actively discussed in literature, simple dislocation structure of reorientation bands indicates the collective nature of evolution of dislocation structure during the formation and motion of such reorientation bands. It was shown before reorientation band forming, the surface relief becomes striped. The dislocation structures were completely different on surfaces “1” and “2”. They depend on nucleation of dislocations in different slip systems.

In high temperature creep experiments under the condition of formation of new dislocations in crystal, a high amount of dipoles of partial disclinations develop. Thus, we can infer that partial disclinations carry the rotational deformation.

1. V.V.Rybin. Big plastic deformations and fracture of metals. Moscow. Metallurgiya, (1986), 224 p. (in russian).
2. V.A. Likhatchev, V.E.Panin, E.E.Zasimchuk et. al. Cooperative deformation processes and deformation localization. Kyiv. Naukova dumka, (1989), 320 p. (in russian).
3. Friedel, Jacues. Dislocations. Addison-Wesley, Reading, MA, (1964), 491 p.
4. V.I.Vladimirov, A.E.Romanov. Disclinations in crystals, Leningrad. Nauka, (1986), 224 p. (in russian).
5. V.P.Matsokin, I.N.Pahomova. Functional Materials. V.13, N 4, 600 (2006).
6. D.V.Matsokin, I.N.Pakhomova, V.P.Matsokin. Powder Metallurgy and Metal Ceramics, V. 47, N 11-12, 646 (2008).

Вісник ХНУ, № 1158, серія «Фізика», вип. 22, 2015. с. 45-47

PACS: 74.72.-h

Fluctuation conductivity of hafnium doped $YBa_2Cu_3O_{7-\delta}$ ceramic

S.V. Savich, A.V. Samoilov, A.L. Samsonik,
V.N. Sukhov, K.V. Tiutierieva, R.V.Vovk

Kharkiv National University
Svobody Sq. 4, 61022 Kharkiv, Ukraine
Ruslan.V.Vovk@univer.kharkov.ua

The conductivity of Hf doped $YBa_2Cu_3O_{7-\delta}$ ceramics was studied in the thesis. It was shown that the introduction of Hf additive leads to the increase of the amount of scattering effective centers of normal carriers. Excessive conductivity of the studied samples near T_c is satisfactorily described by a theoretical model of Aslamazov-Larkin. At the same time Hf additive leads to a significant increase in the absolute value of $\xi_c(0)$ and the shift of 3D-2D crossover point with regard to the temperature.

Keywords: $YBa_2Cu_3O_{7-\delta}$ ceramics, doping, fluctuation conductivity, the coherence length, 3D-2D crossover.

В работе исследована проводимость керамик $YBa_2Cu_3O_{7-\delta}$ допированных Hf. Показано, что внесение примеси Hf приводит к возрастанию числа эффективных центров рассеяния нормальных носителей. Избыточная проводимости исследованных образцов вблизи T_c удовлетворительно описывается теоретической моделью Асламазова-Ларкина. При этом добавка Hf приводит к значительному возрастанию абсолютного значения величины $\xi_c(0)$ и смещению по температуре точки 3D-2D кроссовера.

Ключові слова: кераміки $YBa_2Cu_3O_{7-\delta}$, допування, флуктуаційна провідність, довжина когерентності, 3D-2D кросовер.

У роботі досліджена провідність керамік $YBa_2Cu_3O_{7-\delta}$ допованих Hf. Показано, що внесення домішки Hf призводить до зростання числа ефективних центрів розсіювання нормальних носіїв. Надлишкова провідність досліджених зразків поблизу T_c задовільно описується теоретичною моделлю Асламазова-Ларкіна. При цьому добавка Hf призводить до значного зростання абсолютного значення величини $\xi_c(0)$ і зміщення по температурі точки 3D-2D кросовера.

Ключевые слова: керамики $YBa_2Cu_3O_{7-\delta}$, допирование, флуктуационная проводимость, длина когерентности, 3D-2D кроссовер.

A characteristic feature of HTSC, compounds of the 1-2-3 system, is relative simplicity of full or partial substitution of components by their isoelectronic analogues [1]. As it was established in a number of studies [2] such substitution often facilitates slowing of the aging processes in the compounds of such a type and improving of the stability of their technological characteristics. Most clearly it is demonstrated in the case of ceramic samples, which are also currently the most functional in terms of their practical application [3].

At the same time this kind of substitution often leads to the significant evolution of specific physical phenomena observed in the HTSC - materials with regard to the normal (non-superconducting) condition. The latter refers to the pseudogap (PG) and fluctuation (FC) abnormalities, transitions of the metal-insulator type, incoherent electric transport, anisotropy of some physical characteristics, and etc. [4]. According to the modern concepts [4] these unusual phenomena may serve as a key to understanding of the microscopic nature of the high-temperature superconductors, which remains unknown despite the 29-year history of intense experimental and theoretical research.

Taking into consideration the abovementioned the influence of Hf impurities on the fluctuation conductivity in HTSC – YBaCuO ceramics at the near critical temperatures – was investigated in the study.

Samples of $YBa_2Cu_3O_{7-\delta}$ ceramics were synthesized by interaction of Y_2O_3, $BaCO_3$, and CuO (all OS grades) compounds taken in the respective molar ratios in the temperature range 750-900^o C. The obtained powder was pressed under pressure of 4 ton/cm^2 into the disks of 20x4 mm size and sintered at the temperature of 950-970°C within 5 hours followed by cooling to the room temperature with intermediate dwell of 2-3 hours at the temperatures of 890 and 530°C. The obtained tablets represented superconducting ceramics with rhombic symmetry of lattice and T_c~90 K. For obtaining samples with addition of hafnium the starting material was added with a various quantity of weight % of Hf_2O_3. Modes of production and saturation with oxygen were the same as for the undoped ceramics.

X-ray studies of the structure and phase composition of the samples of $YBa_2Cu_3O_{7-\delta}$ ceramic depending on

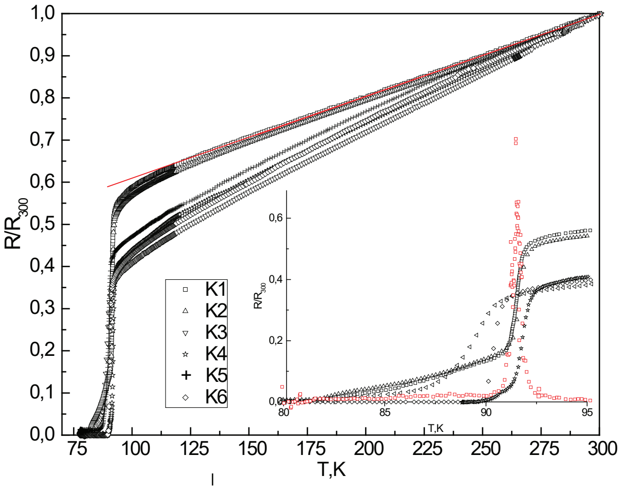

Fig. 1. Dependence of reduced electrical resistance $R/R_{300}(T)$ of ceramic samples with the addition of K1 hafnium. The inset shows the transition to the superconducting state in the coordinates of $R/R_{300}(T)$ and $d(R/R_{300}(T))/dT$ - T in the area of superconducting transition of one sample. Numbering of the curves in the inset corresponds to the numbering in the Fig.

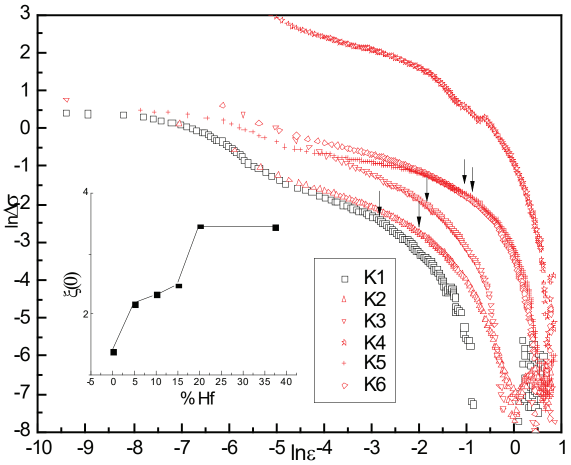

Fig. 2. Temperature dependences of the excess conductivity for K1 - K6 samples in lnΔσ-lnε. Designation of the curves corresponds to the designations in the Fig.1. Straight lines show an approximation to the inclination angle $tg\alpha_1 \approx -0.5$ (3D - mode) and $tg\alpha_2 \approx -1.0$ (2D - mode). Arrows show the point of 2D-3D crossover. The inset shows the dependences of coherence length $\xi_c(0)$ on the percentage of hafnium in the samples.

the hafnium additions were carried out on the DRON-3 X-ray diffractometer in Cu-Kα-radiation. Profiles of X-ray diffraction peaks were built by manual scanning with intervals of angles of 2θ=0,1° in the background and with intervals of 2θ=0,02° at maximum. Analysis of the obtained diffractograms showed that the initial sample had an orthorhombic structure of perovskite type with the following lattice parameters: a=3.8348Å, b=3.8895Å, c=11.6790Å, which corresponds to the literature data. With increasing content of Hf_2O_3 hafnium oxide additives the intensity of X-ray diffraction peaks corresponding to the initial structure is reduced and diffraction peaks corresponding to the orthorhombic structure perovskite of type appear on diffractograms X-ray but with higher parameters of lattice.

For resistive studies the pieces of rectangular shape were sawed from the “tablets”. Contacts were applied by rubbing of ceramic India into the surface followed by soldering of copper conductors to these sites. The electrical resistivity was measured by standard 4 contact procedure with direct current up to 10 mA. The sample temperature was determined by platinum thermal resistor.

Temperature dependences of the stated electrical resistance of $R/R_{300}(T)$ samples are shown in Figure 1. Resistive transitions into the superconducting state of the same samples are shown in the inset. It appears that the dependences are quasimetallic. The parameters of the studies samples are shown in the table. According to the literature data the high values of T_c=92.1 K critical temperature correspond to the oxygen content $\delta \le 0.1$ [5].

As we can see from the Figure 1 $R/R_{300}(T)$ deviation from linear dependence take place with the decrease of temperature below a certain characteristic value of T* which shows the appearance of a certain excess conductivity, which according to the theoretical concepts [6] near T_c is conditioned by processes of fluctuation pairing of the carriers. Their contribution to the conductivity at $T>T_c$ for two (2D) and three-dimensional (3D) cases is determined by the following power dependence (6):

$$\Delta\sigma_{2D} = \frac{e^2}{16\hbar d}\varepsilon^{-1}, \tag{1}$$

$$\Delta\sigma_{3D} = \frac{e^2}{32\hbar\xi_c(0)}\varepsilon^{-1/2}, \tag{2}$$

where $\varepsilon=(T-T_c)/T_c$, e - electron charge, $\xi_c(0)$ - is coherence length along the c axis at T→0 and d - is a characteristic size of a two-dimensional layer. In our case T_c was determined at the maximum point in the dependences of $d(R/R_{300})/dT$ in the area of superconducting transition (Fig. 1 Inset).

The temperature dependence of the excess conductivity is usually determined by the equation:

$$\Delta\sigma = \sigma - \sigma_0, \tag{3}$$

where $\sigma_0=\rho_0^{-1}=(A+BT)^{-1}$ is the conductivity determined by interpolation of the linear section of ρ(T) to the zero value of the temperature and $\sigma=\rho^{-1}$ is an experimentally determined value of conductivity in the normal condition.

Fig. 2 shows the temperature dependences of Δσ(T) in ln Δσ– lnε coordinates. It can be seen that near T_c these curves are approximated satisfactorily by straight lines with a slope of tg α1~0.5 corresponding to the exponent parameter of —1/2 in the equation (2), which obviously

Table

Samples	% Hf	T_c, K	T*, K	Δ^*_{ab}, meV	Ln(ε_0)	ε_0	$\xi_c(0)$, Å
K1	0	91,47	154	0,1006	-2,87	0,0567	1,39297
K2	5	91,62	160	0,06776	-1,98	0,13807	2,17372
K3	10	89,5	165	0,0675	-1,84	0,15882	2,33134
K4	15	91,65	250	0,05647	-1,714	0,18014	2,48294
K5	20	90,17	240	0,0306	-1,05	0,34994	3,4606
K6	37,5	90,38	237	0,03897	-1,06	0,34646	3,44334

evidences about 3D character of the fluctuation conductivity in this temperature interval. Upon further temperature increase the rate of Δσ decrease substantially increases (tg α2~1) which in its turn can be interpreted as an indication for change of fluctuation conductivity dimensionality. As it follows from Eqs. (1) and (2) at the point of 2D-3D crossover:

$$\xi_c(0)\varepsilon_0^{-1/2} = d/2\,. \tag{4}$$

In this case having determined ε_0 value and using literature data on the dependence of the interplane distance on δ [7] (d ≈ 11.7 Å) it may be possible to calculate the values of ξc(0). The concentration dependences of the coherence length $\xi_c(0)$ are shown in the inset to the Figure 2.

The made calculations showed that with introduction of Hf additives a change in the value of coherence length from $\xi_c(0)$=1,39Å in YBaCuO to $\xi_c(0)$=3.44Å in Hf doped samples takes place by 37.5% and 3D-2D crossover point significantly shifts with regard to the temperature (see Table and Fig. 2).

In conclusion, we briefly resume the main results obtained in this paper. Excessive conductivity Δσ(T) of Hf-doped YBaCuO samples in the case nearing T_c is satisfactorily described in the framework of a theoretical model of Aslamazov-Larkin. Doping of YBaCuO single crystals by hafnium leads to a more than twofold increase in the absolute value of $\xi_c(0)$ and significant shift of 3D-2D crossover point with regard to the temperature.

1. D. M. Ginsberg (ed), Physical properties high temperature superconductors I. – Singapore: Word Scientific, 1989.
2. D. A. Lotnyk, R. V. Vovk, M. A. Obolenskii, A. A. Zavgorodniy, J. Kovac, V. Antal, M. Kanuchova, M. Sefcikova, P. Diko, A. Feher, and A. Chroneos. Evolution of the fishtail-effect in pure and Ag-doped MG-YBCO. J. Low Temp. Phys., 161, 387-394, 2010.
3. Z. Li, H. Wang, N. Yang, X. Jin, and S. L. J. Chin. Ceram. Soc., 18, 555-560, 1990.
4. J. Ashkenazi, J. Supercond. Nov. Magn. 24, 1281 (2011).
5. P. Schleger, W. Hardy, and B. Yang. Thermodynamics of oxygen in $YBa_2Cu_3O_x$ between 450^{0}C and 650^{0}C. Physica C, 176, 261-273, 1991.
6. L. G. Aslamasov and A. I. Larkin. The influence of fluctuation pairing of electrons on the conductivity of normal metal. Phys. Lett. A, 26, 238-239, 1968.
7. G. D. Chryssikos, E. I. Kamitsos, J. A. Kapoutsis, A. P. Patsis, V. Psycharis, A. Koufoudakis, C. Mitros, G. Kallias, E. Gamari-Seale, and D. Niarchos. X-ray diffraction and infrared investigation of $RBa_2Cu_3O_7$ and Rc L_5PrC $h_5Ba_2Cu_3O_7$ compounds (R=Y and lanthanides). Physica C, 254, 44-62, 1995.

Вісник ХНУ, № 1158, серія «Фізика», вип. 22, 2015. с. 48-50

PACS 05.70.-a; 05.60.-k
UDC 536.79, 538.93, 53,043

Special features of low temperature gases separation using peltier elements and mixture throttling

M.M. Zholonko, V.I. Unrod

Cherkasy State Technological University
bul. Shevchenko, 460, Cherkasy, Ukraine, 18006
zholonko@yahoo.com

It was examined special features of Peltier elements using for gas mixture separation into components and low temperature cryogenic liquids obtaining in low-powered production using Joule-Thomson effect in the second stage of cooling. It was carried out the measurements of necessary heat, electricity and cooling flows for components separation of the air and hydrogen-oxygen mixtures in order to obtain liquid nitrogen, oxygen and hydrogen with a help of specially made investigation equipment.

Keywords: gas separation by cooling, Peltier element, throttling, liquid nitrogen, oxygen, hydrogen.

Розглянуті особливості використання елементів Пельтьє для розділення суміші газів на компоненти та одержання низькотемпературних кріорідин в малопотужних виробництвах з використанням ефекту Джоуля-Томсона на другому ступені холоду. За допомогою створеного дослідного обладнання проведені вимірювання необхідних потоків тепла, електроенергії та охолоджувача для розділення на компоненти повітря і водньево-кисневої суміші з метою отримання рідких нітрогену, оксигену та гідрогену.

Ключові слова: розділення газів охолодженням, елемент Пельтьє, дроселювання, рідкі нітроген, оксиген, гідроген.

Рассмотрены особенности использования элементов Пельтье для разделения смеси газов на компоненты и получения низкотемпературных криожидкостей в маломощных производствах с использованием эффекта Джоуля-Томсона на второй ступени холода. С помощью созданного исследовательского оборудования проведены измерения необходимых потоков тепла, электроэнергии и хладагента для разделения на компоненты воздуха и водородно-кислородной смеси с целью получения жидких азота, кислорода и водорода.

Ключевые слова: разделение газов охлаждением, элемент Пельтье, дросселирование, жидкие азот, кислород, водород.

One of the main methods [1] of industrial gas separation into components with high purity is low temperature method, based on the using of boiling temperatures differences in the liquid state of different substances, which is caused by the nature of intermolecular interactions [2,3]. Other (non-cryogenic) methods are also often used, for example membrane one, where there are conditions for small size molecules moving through a small hole or cavity fiber, adsorption method (carbon nanotubes are especially promising today [4]), and space division method with a space separation of mixture on electrodes [5]. Last one is used in water electrolysis (Figure 1) when oxygen is evolving at the anode and hydrogen – at the cathode.

This method is more effective using the electrode plates placed in opposite one to another, between which transparent membranes for ions are fixed. Gases evolving at the electrodes go up under Archimedes force to different capacities (figure 1). However, the existing of the membranes and separated capacities for gases withdrawal to different capacities make process of separation more difficult and slower. Therefore, for big capacities, at first the gas mixtures are obtained, and then the separation is caring out, for example, using low temperatures [6].

The aim of this study was to examine the possibility of cryogenic separation of gas mixture into components in low-powered unit using deep cooling process without gas-expansion machines in conditions of limited element base. Low temperatures are easy to get using Peltier semiconductor elements when it is enough low power for heat flow withdrawal [7].These are machineless devices in the form of the plate, one side of which is heating by current and requires heat withdrawal, and another one is cooling. In this case the temperature differences between the surfaces can reach more than 50 K. Peltier elements cascade connection is applied too [8]. During a parallel connection increases the cooler capacity while in sequential case it will be for the temperature difference. These plates using experience proves that in the two-stage sequential connection they can create low temperatures with the

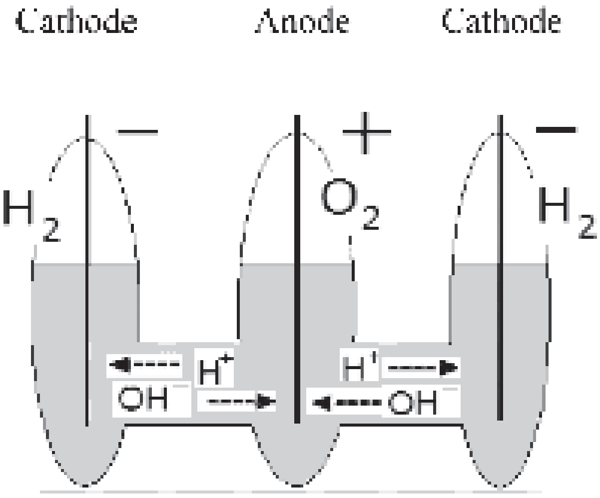

Fig.1. Diagram of non-cryogenic manner of gases separation during water electrolysis without low temperature using in consideration of product stoichiometry (double volume of H_2 for one volume of O_2).

difference of over 100 K and operate in a stable mode.

However, Peltier elements are the most effective under the normal conditions and with a few sequential cascades [8], but lower temperatures obtaining for the accumulation of elements in cascade leads to bigger thermal losses and total thermal resistance of the bridge. There is reduction of unit efficiency at low temperatures. In low-powered scheme, shown in figure 2, Joule-Thomson effect of gas throttling through a porous baffler from 1.5 MPa pressure to atmospheric pressure was applied to further mixture temperature reducing [2]. Because of Peltier elements, the temperature of hydrogen that needed to be cooled was becoming less than inversion temperature. For oxygen it reaches 893 K, and for hydrogen is 204.6 K.

Thus, Peltier elements using two-stage sequential diagram make possible in both cases to get mixture temperature reducing at first stage of cooling. It should be mention that oxygen liquefies at 90.2 K and solidifies at 54.4 K. Hydrogen liquefies at 20.4 K and solidifies at 13.8 K. Therefore, to separate oxygen from nitrogen or hydrogen for Peltier elements with throttling on the second stage is not a technical problem (nitrogen liquefies at temperature of 77.4 C and solidifies at 63.15 K). This process is more complicated for hydrogen. Especially difficult is to liquefy helium as the temperature must be 4.2 K. Helium solidifies only when at 2 K temperature is creating additional 3.76 MPa pressure for the main isotope ^{4}He and for ^{3}He at 1.0 K and 87 MPa [10].

In the diagram (figure 2) was shown the additional temperature reduction and throttling of mixture conducted after using semiconductor elements. The mixture was separated by the pressure expansion from 1.5 MPa to normal one. It was in Dewar vessel. The general scheme of unit was shown in figure 2. Compressed gas mixture for cooling was moving sequentially through two radiators. Then gases reach cold side of Peltier bridge, hot side of which was cooling by running water or gas. Following temperature reducing of gas mixture was in the heat-transfer apparatus, where counter cold flow of gases from Dewar vessels that have been not liquefied during throttling in a cryostat returned to the balloon.

Starting of liquid oxygen selection from the air or detonating mixture could be observed in Dewar translucent glass vessel. Cessation of oxygen accumulation in the vessel indicates its selection completion. Then, in the

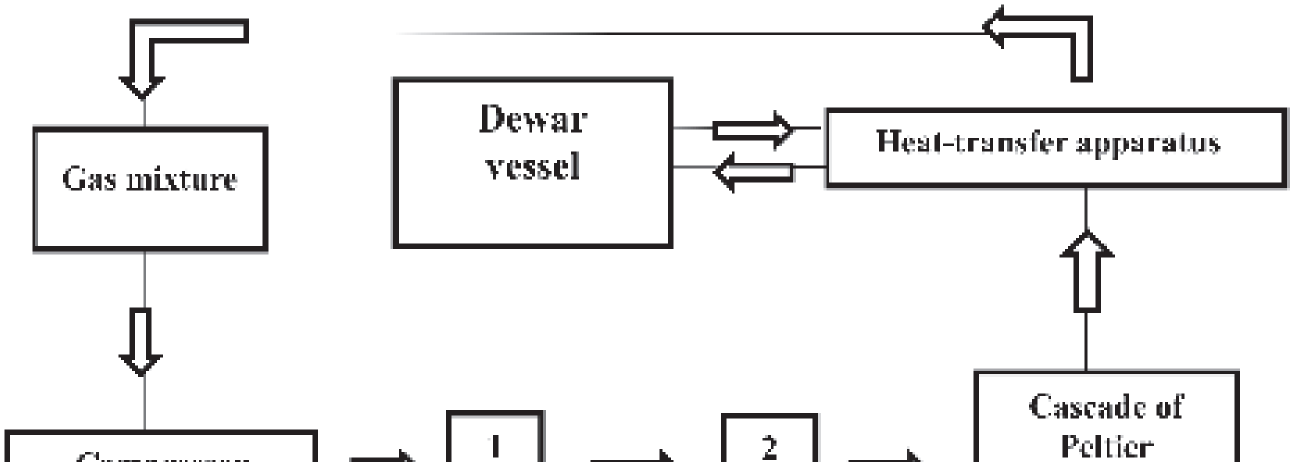

Fig.2. The scheme of low temperature separation of gases from gas mixture: 1 - radiator with air cooling and drier; 2 - radiator with dry or ordinary ice cooling and decarbonifier (water solution of NaOH). It was used Peltier TES1-12706 elements with power 53 V (size 40x40 mm^2). In Dewar translucent glass vessel we can obtain gases mixture separation due to one of the components liquefaction.

first case, nitrogen is extricating with argon in the balloon (argon concentration increases in dozens of times from 1%). If the mixture is detonating it will be undiluted hydrogen. However, some little residual concentration of oxygen remains in the balloon. Table 1 shows the ratio of gas components of air that successively transfer into the liquid during throttling.

Hydrogen in the separation process of detonating mixture begins to liquefy [10] if it has been cooled before throttling by liquid nitrogen or oxygen and if thermal insulation was provided. Getting of liquid hydrogen provides an opportunity to study and to use new application of superconductivity of magnesium diboride MgB_2 (2001, transition into a state of superconductivity occurs at 39 K [11]).We can get liquid helium from liquid hydrogen by throttling without which fundamental low-temperature researches are almost impossible today. Liquid hydrogen is very important today as the most powerful and the most ecological fuel, which is used for solving current problems of energy, environment and materials science [12, 13] and for creation of rocket fuels for near space [14].

As a result of done work with using Peltier semiconductor elements and method of throttling (Joule-Thomson effect) was created a low-powered unit for the air and hydrogen liquefaction, which allowed to conduct low temperature researches and to teach undergraduates and graduate students.

Table 1.

The mean air composition in normal environment conditions.

Components of the air	Concentration by capacity %	Concentration by weight %	List number
Nitrogen	78,2	75,5	[9]
Oxygen	20,9	23,2	[9]
Inert gases	0,9	1,3	[9]

1. Receiving and production of industrial gases (http: //www.dpairgas.com.ua/).
2. I.K. Кікоіn, A.K. Кікоіn. Physics of Molecules. Moscow: Physmathlit, 1963, 500 p.
3. Physics of Cryocrystals, V.G. Manzhelii, Yu. A. Freiman, M.L. Klein, and A.A. Maradudin (eds.), AIP Press, New York (1996).
4. P.N. Diachkov. Carbon nanotubes: structure, properties and applications. Moscow: Binom, 2006, 293 p.
5. L.M. Yakimenko, I.D. Modilevskaya, Z.A. Tkachek. Water Electrolysis. Moscow: Chemistry, 1970, 264 p.
6. Verkin B.I. Cryogenics. Kiev: Naykova dymka, 1985, 180 p.
7. S.G. Kalashnikov. Electricity. Moscow: Physmathlit, 2003, 624 p.
8. A.L. Vainer. Cascade thermoelectric coolers. Moscow: Soviet Radio, 1976, 136 p.
9. N.L. Glinka. Common Chemistry. Leningrad: Chemistry, 1977, 718 p.
10. V.B. Sokolov. Helium (article in Book of Chemistry). Moscow: Soviet entsyclopedia, v.1, 1988, 623 p.
11. E.E. Shpilrain, S.P. Malishenko, G.G. Kuleshov (common editor V.A. Legasov). Introduction in hydrogen energetics. Moscow: Energoatomizdat, 1984, 264 p.
12. V.I. Unrod. Introduction in nanomaterial science and technologies. Cherkasy: Chabanenko publishing, 2013, 262 p.
13. M.M. Zholonko. Manned investigation of Venus by the hydrogen balloons. Cherkasy: Shityuk publishing, 2013, 208 p.
14. B.V. Balmont, A.S. Karpov, R.K. Ivanov. About problems and future way of Russian air- space project "Air Start", December, 2012 (http://www.eurasian-defence.ru).

Вісник ХНУ, № 1158, серія «Фізика», вип. 22, 2015. с. 51-57

PACS 05.45.Xt, 74.50.+r, 85.25.Cp
УДК: 537.312.62

Resonant modes in the system of two wide interacting Josephson junctions

Alexander Grib

Physics Department, Kharkiv V. N. Karazin National University, Svobody sq. 4, 61022, Kharkiv, Ukraine

Zero-field steps and Fiske steps in IV-characteristics of the stack of two inductively coupled wide Josephson junctions with normal edges were investigated numerically. It was found that inductive coupling of junctions leaded to splitting of each of the step in two steps. Dependences of frequencies of steps on the parameter which characterizes inductive coupling of junctions obeyed the relation obtained for frequencies of inductively coupled resonance contours. Dependences of amplitudes of split Fiske steps on applied external magnetic field were calculated and compared with the theory.

Keywords: Josephson junctions, high-temperature superconductors, Fiske steps, resonant modes.

Сходинки нульового поля та сходинки Фіске на вольт-амперних характеристиках пачки з двох індуктивно з’єднаних між собою широких джозефсонівських контактів з нормальними краями були досліджені чисельно. Знайдено, що індуктивний зв’язок привів до розщеплення кожної сходинки на дві сходинки. Залежності частот сходинок від параметру, який характеризує індуктивний зв’язок між контактами, підкоряються співвідношенню, що було отримано для частот індуктивно з’єднаних резонансних контурів. Розраховані та порівняні з теорією залежності амплітуд розщеплених сходинок Фіске від прикладеного зовнішнього магнітного поля.

Ключові слова: джозефсонівські контакти, високотемпературні надпровідники, сходинки Фіске, резонансні моди.

Были исследованы численно ступеньки нулевого поля и ступеньки Фиске на вольт-амперных характеристиках пачки, состоящей из двух индуктивно связанных между собой широких джозефсоновских переходов с нормальными краями. Было найдено, что индуктивная связь переходов привела к расщеплению каждой ступеньки на две. Зависимости частот ступенек от параметра, который характеризует индуктивную связь переходов, подчиняются соотношению, которое было получено для частот индуктивно связанных резонансных контуров. Рассчитаны и сравнены с теорией зависимости амплитуд расщеплённых ступенек Фиске от приложенного внешнего магнитного поля.

Ключевые слова: джозефсоновские переходы, высокотемпературные сверхпроводники, ступеньки Фиске, резонансные моды.

Introduction

The problem of the adequate description of IV-characteristics of intrinsic Josephson junctions in high-temperature superconductors includes the development of different types of the interaction between junctions such as the inductive coupling of intrinsic junctions [1, 2] and resistive shunting of neighbor junctions [3, 4]. On the other hand, these inductive and resistive couplings produce new effects which can be responsible for the appearance of coherent emission in the stack of intrinsic Josephson junctions without applied external magnetic field [5]. It was found [5] that coherent emission appeared in the vicinity of steps in IV-characteristic. The origin of this effect is the subject of the contemporary investigations [6]. We found recently that the IV-characteristic of the wide Josephson junction with the normal edges revealed so-called zero-field steps [7]. These zero-field steps appear in the IV-curve when the edges of the stack are in the normal state due to diffusion of the oxygen out of the stack. The physical origin of the formation of the zero-field step consists in the interaction of the ac Josephson current with excitations of the electromagnetic field which are introduced into the junction through normal edges [8]. Voltages which correspond to these steps are equal to

$$V_s = \frac{\Phi_0 \bar{c} s}{D}, \tag{1}$$

where D is the width of the junction, Φ_0 is the quantum of magnetic flux, $\bar{c}$ is the velocity of light in the junction and s is an integer. These voltages correspond to even Fiske steps:

$$V_p = \frac{\Phi_0 \bar{c} p}{2D}, \tag{2}$$

where p is an integer, so $p = 2s$. Fiske steps appear when external magnetic field is applied in parallel to the junction [9]. Their origin is connected with the interaction of the ac Josephson current and the standing-wave electromagnetic fields in the junction. However, steps which appear due to the process of the propagation and the reflection of electromagnetic excitations are observed without applied external magnetic field. Therefore they are called as zero-field steps.

In the present paper zero-field steps in IV-characteristics of the stack of two Josephson junctions with normal edges are investigated numerically at different values of the parameter which characterizes inductive coupling between junctions. Inductive coupling is introduced similarly to the model developed in Refs. [1, 2]. We show that the coupling leads to the split of zero-field step. We also investigate the influence of coupling on the first and the second Fiske steps.

The model

The stack of wide Josephson junctions is presented in Fig. 1a, and the high-frequency scheme of the stack is shown in Fig. 1b. Each of the wide junctions is divided into n ‘elementary junctions’ with critical currents $I_{ci,j}$, where i=1,2 is the number of the wide junction in the stack, j = 1…n is the number of the ‘elementary junction’. It is supposed that the dc bias current I_b feeds each of the ‘elementary junctions’ independently. For the use of visual aids, two wide junctions in the high-frequency scheme are fully separated, though in the equivalent high-frequency scheme one can connect each pair of inductances L_f in 'elementary cells' into one common mutual inductance and connect also each 'elementary junction' in the upper wide junction with the corresponding 'elementary junction' in the lower wide junction by the current line. According to the resistively and capacitively shunted model [10], each of the ‘elementary junctions’ has the resistance $R_{i,j}$, the capacitance C and the source of the Josephson current $I_{Ji,j} = I_{ci,j}\cdot\sin\varphi_{i,j}$ with φ_{ij} is the difference of the phase of the order parameter across the junction (Fig. 1b). We assume that the critical voltage is equal to $V_c = I_{ci,j}R_{i,j}$ = const for all ‘elementary junctions’. 'Elementary junctions' are divided by the distance $\zeta = \sqrt{cCL}$, where L is the inductance of the 'elementary cell' between junctions. To model normal edges of the stack, each edge of the wide junctions is connected to the contour which contains the resistance $R_{ei,j}$, the capacitance $C_{ei,j}$ and the inductance $L_{ei,j}$ (Fig. 1b). These additional contours introduce electromagnetic excitations in the stack. To show main features of our model, we assume the simplest case when $R_{ei,j}$ = const., $C_{ei,j}$ = const. and $L_{ei,j}$ = const., i.e. all resistances $R_{ei,j}$ are the same for all edges etc. Then the full system of equations which describe the high-frequency scheme of the whole stack of junctions with boundary conditions include current conservation conditions for junctions, Kirchhoff rules and flux quantization conditions:

$$\frac{\Phi_0 C_{i,j}}{2\pi}\frac{d^2\varphi_{i,j}}{dt^2} + \frac{\Phi_0}{2\pi R_{i,j}}\frac{d\varphi_{i,j}}{dt} + I_{ci,j}\sin\phi_{i,j} = I_b - I^R_{i,j} + I^R_{i,j+1} \ , \ i = 1{,}2, \ j = 2 \ldots n-1, \tag{3}$$

$$\frac{\Phi_0 C_{i,n}}{2\pi}\frac{d^2\varphi_{i,n}}{dt^2} + \frac{\Phi_0}{2\pi R}\frac{d\varphi_{i,n}}{dt} + I_{ci,n}\sin\varphi_{i,n} = I_b - I^R_{i,n} + \frac{dq_{i,n+1}}{dt} \quad i = 1{,}2\,, \ j = 1, \tag{4}$$

$$\frac{\Phi_0 C_{i,n}}{2\pi}\frac{d^2\varphi_{i,n}}{dt^2} + \frac{\Phi_0}{2\pi R}\frac{d\varphi_{i,n}}{dt} + I_{ci,n}\sin\varphi_{i,n} = I_b - I^R_{i,n} + \frac{dq_{i,n+1}}{dt} \ , \ i = 1{,}2\,, \ j = n, \tag{5}$$

$$L_{ei,j}\frac{d^2 q_{i,j}}{dt^2} + R_{ei,j}\frac{dq_{i,j}}{dt} + \frac{q_{i,j}}{C_{ei,j}} = \mp\frac{\Phi_0}{2\pi}\frac{d\varphi_{i,j\pm1}}{dt} \ , \ i = 1{,}2\,, \ j = 0, n+1, \tag{6}$$

$$LI^R_{1,j} - L_f I^R_{2,j} + \left[\Phi_e + \frac{\Phi_0}{2\pi}\left(\varphi_{1,j-1} - \varphi_{1,j}\right)\right] = 0 \ , \ j = 2 \ldots n, \tag{7}$$

$$-L_f I^R_{1,j} + LI^R_{2,j} + \left[\Phi_e + \frac{\Phi_0}{2\pi}\left(\varphi_{2,j-1} - \varphi_{2,j}\right)\right] = 0 \ , \ j = 2 \ldots n\,, \tag{8}$$

where I^R_{ij} is the current in the loop between two ‘elementary junctions’, Φ_e is magnetic flux created by the external applied magnetic field, L_f is the mutual inductance between two adjacent cells of the ‘elementary stack’. Note that additional contours at edges have numbers j = 0 and j = n+1 for each wide junction (see Eq. (6)).

Now we describe the set of parameters which was defined for the solution of the described above system of equations. At first, the width D, the length W, density of the critical current J_c, critical voltage V_c and inductance of the wide junction per unit of length L_{ul} were set the same for all wide junctions. The length of the junction W was introduced formally because our model was one-dimensional. Then wide junctions were divided into n cells with the length $\zeta = D/n$, so the

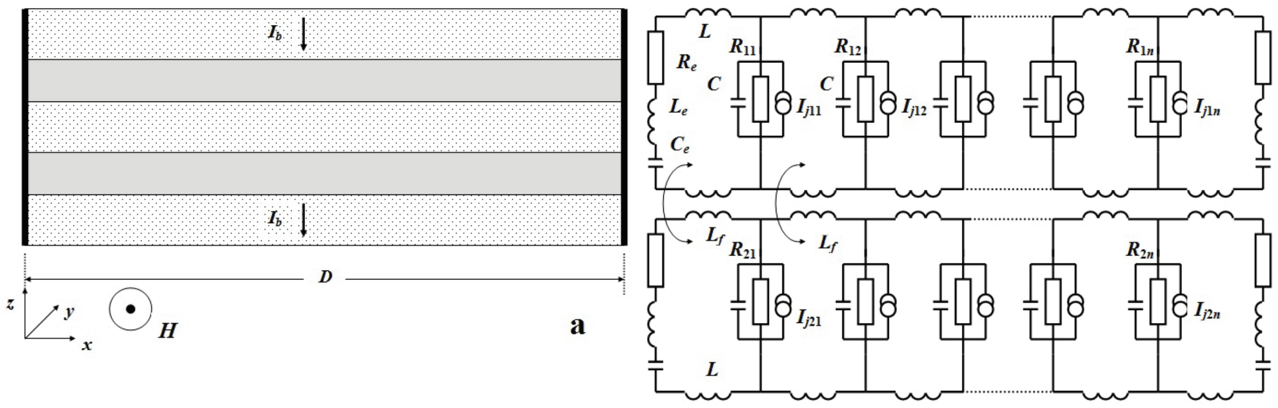

a *b*

Fig.1. (a)- the stack of two wide Josephson junctions. Insulator is shaded. Black solid lines at ends of the stack symbolize the $R_eL_eC_e$-shunting. (b)- the electrical scheme of the stack of two inductively coupled junctions.

critical current and the resistance of each 'elementary junction' were calculated as $I_{ci,j} = I_c = J_c \cdot W \cdot \zeta$ and $R = V_c/I_c$. The inductance of each 'elementary cell' and the capacitance of the 'elementary junction' were calculated as $L=L_{ul}\cdot\zeta$ and $C = \zeta^2/\left(\bar{c}^2 L\right)$ [11, 12]. The value of mutual inductance between 'elementary junctions' in the stack was defined as $L_f = \alpha L$, where α is dimensionless parameter. Then Eqs. (3)-(8) were solved for different bias currents. IV-characteristics were obtained in calculations. The normalized to the quantity of wide junctions voltage over the stack was calculated as $V = \frac{\Phi_0}{2\pi}\frac{1}{2n}\left\langle \sum_{j=1}^{n}\left(\sum_{i=1}^{2}\frac{d\varphi_{i,j}}{dt}\right)\right\rangle$, where the sign $\langle \ldots \rangle$ means full averaging over the large interval of time [7, 10]. Values of parameters were chosen as follows: $D = 70\cdot10^{-6}$ m, W=$300\cdot10^{-6}$ m, J_{ctot}= 10^5 A/m^2, V_c = 4.74 mV, L_{ul}=$7\cdot10^{-9}$ H/m, $\bar{c} = 6.708\cdot10^7$ m/sec [5], β_C = 68.4, n = 20. The Josephson depth of penetration of magnetic field in the single junction was equal to $\lambda_J = 55\cdot10^{-6}$ m. For boundary conditions we chose values of $R_{ei,j}$= 600 Ohm, $L_{ei,j}$ = 0.23 pH, $C_{ej,i}$ = 0.011 pF for both junctions with i = 1,2 and both boundaries with j = 0 and j = n+1.

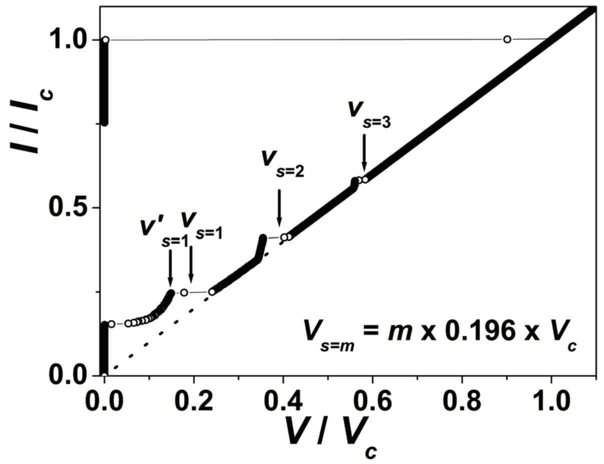

Fig. 2. Zero-field steps in the normalized IV-curve of the single wide Josephson junction. The interval between steps is $V_s = 0.199\cdot V_c$. Positions of voltages $v_s = V_s / V_c$ of zero-field steps are marked by arrows. The voltage $v'_{s=1} = V'_{s=1}/V_c$ corresponds to the highest visible value of the current in the first step. The dotted line $I_b/I_c=V/V_c$ is the Ohm law which determines the hysteretic branch. Parameters of the junction (see the section 2): D= $150\cdot10^{-6}$ m, $\lambda_J = 36\cdot10^{-6}$ m, $W = 300\cdot10^{-6}$ m, $L_{ul} = 8\cdot10^{-9}$ H/m, n = 30, J_c = $\cdot10^5$ A/m^2, V_c = 4.736 mV, $L_{e0} = L_{en+1}$ = $3.7\cdot10^{-13}$ H, R_{e0}=R_{en+1}= 600 Ohm, C_{e0}= C_{en+1}= $1.5\cdot10^{-14}$ F.

Results and Discussion

Steps in IV-characteristics obtained in the range of the resistively shunted model have some particularities. As an example, let us consider the IV-curve of single wide Josephson junction which contains zero-field steps (Fig. 2) [7]. All of them are situated in intervals of jumps of voltages which appear due to the instability of the IV-curve (voltages at the step and at the hysteretic branch correspond to the same value of the current). Experiments on junctions with the overlap geometry [13] prove this result. Therefore, instead of V_s, we consider the abscissa V'_s of the highest point of the visible part of the step (see Fig. 2). It is possible if we are interesting not in the exact value of V_s but in the change of V_s in some process (like the dependence of V_s on α) supposing that the difference $V_s - V'_s$ remains constant.

IV-characteristics of the stack of junctions are shown in Fig. 3a,b for $\alpha = 0$ and $\alpha = 0.3$, correspondingly. The step is seen at $V'_{s=1}$= $0.392\cdot V_c$ in Fig. 3a, whereas in Fig. 3b there are the zero-field step at $V'_{s=1,d}$ = $0.335\cdot V_c$ and the zero-field step at $V'_{s=1,u}$ = $0.474\cdot V_c$. Two wide junctions in the stack do not interact with each other at $\alpha = 0$.

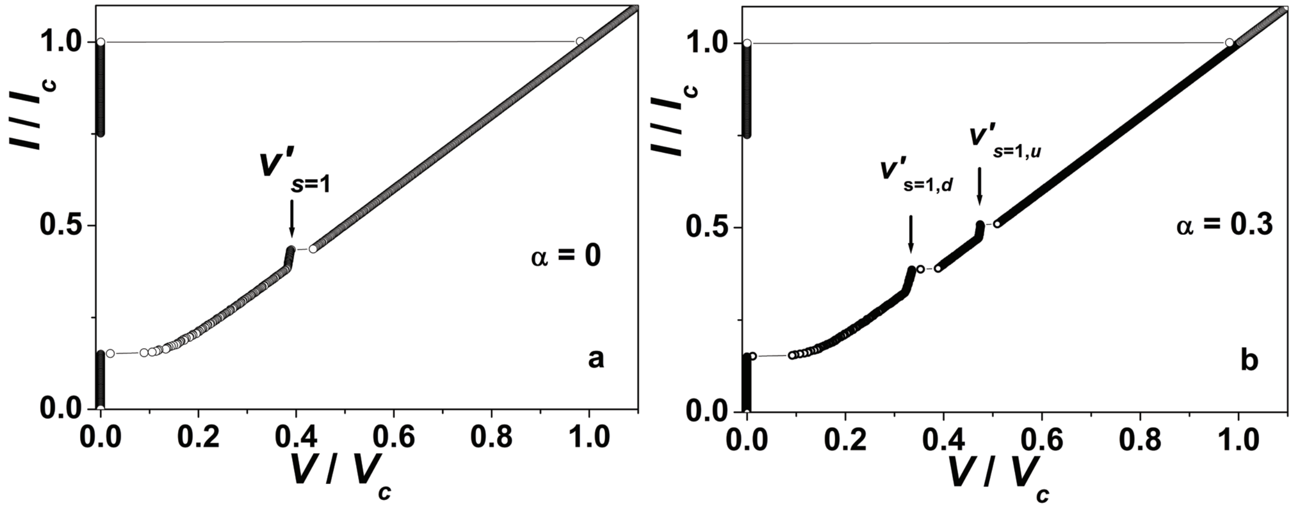

a *b*

Fig.3. IV-characteristics of the stack of two wide junctions without the inductive coupling of junctions (a) and with inductive coupling of junctions (b). The parameter of coupling is equal to $\alpha = 0$ for (a) and $\alpha = 0.3$ for (b). Arrows mark the value of $v'_s = V'_s / V_c$ in (a) and $v'_{s,d} = V'_{s,d} / V_c$, $v'_{s,u} = V'_{s,u} / V_c$ in (b).

However, at $\alpha = 0.3$ there is inductive coupling between junctions. We can conclude that the inductive interaction leads to the split of the zero-field step into two steps. This conclusion is in agreement with the well-known split of resonant frequencies of two inductively coupled resonant contours. In Fig. 4 positions of zero-field maxima are plotted as a function of the parameter α. These plots can be approximated with the good accuracy (solid lines in Fig. 4) by functions

$$V'_{s=1,d} = \frac{V'_{s=1}}{\sqrt{1+\alpha}} \quad \text{and} \quad V'_{s=1,u} = \frac{V'_{s=1}}{\sqrt{1-\alpha}}, \qquad (9)$$

which are well known from the theory of inductively coupled resonance contours. We would like to emphasize that voltages $V_{s=1,d}$ and $V_{s=1,u}$ correspond to some resonant frequencies of the stack of two interacting wide junctions but they do not correspond to any resonant frequencies of the separate wide junctions. This effect is quite similar to the formation of frequencies of normal vibrations in the system of interacting oscillators and, as far as we know, it is obtained here for the first time.

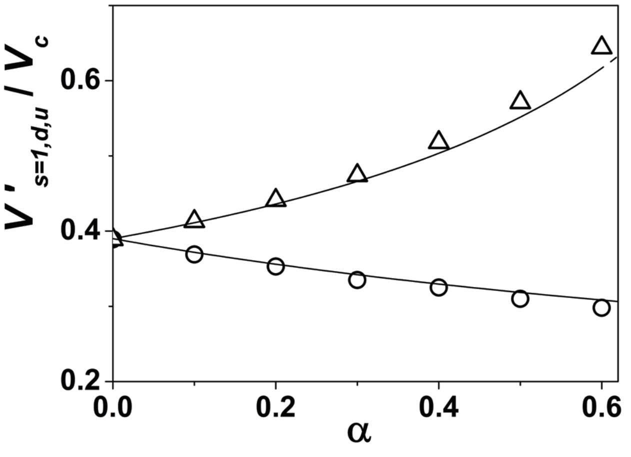

Fig. 4. Dependences of $V'_{s=1,d} / V_c$ (circles) and $V'_{s=1,u} / V_c$ (triangles) on the parameter α. Solid lines are approximations by Eqs. (9).

The found effect of the split of the zero-field step in the stack of two interacting wide junctions can be generalized to the stack which consists of many junctions. In this case the interval of voltages of zero-field steps forms a band, and voltages inside this band correspond to frequencies of vibration modes in the whole stack. Bands can overlap each other. To investigate the formation of bands one should apply another model for 'elementary junctions', because in the ranges of the resistively and capacitively shunted model the band is situated in the interval of the jump of voltage. However, in the present paper we investigate the interval $0 \le \alpha \le 0.6$ at which the overlap is absent (Fig. 4).

The example of the influence of applied external magnetic field on IV-characteristics of the stack of two non-interacting junctions ($\alpha = 0$) and interacting junctions ($\alpha = 0.3$) is shown in Fig. 5a, b. The external applied field $B = 44.2$ G corresponds to the value of Φ / Φ_0 = 1.3 in the stack of two intrinsic junctions of the high-temperature superconductor $Bi_2Sr_2CaCu_2O_8$ mesa with the width 70 micrometers. In the following consideration we will use values of the normalized magnetic flux $\phi = \Phi / \Phi_0$ instead of magnetic field. Four Fiske steps at $V'_p = p \cdot 0.199 \cdot V_c$ are clearly seen in the IV-curve of the stack with $\alpha = 0$ (Fig. 5a). The position of the second Fiske step coincides with the position of the zero-field step

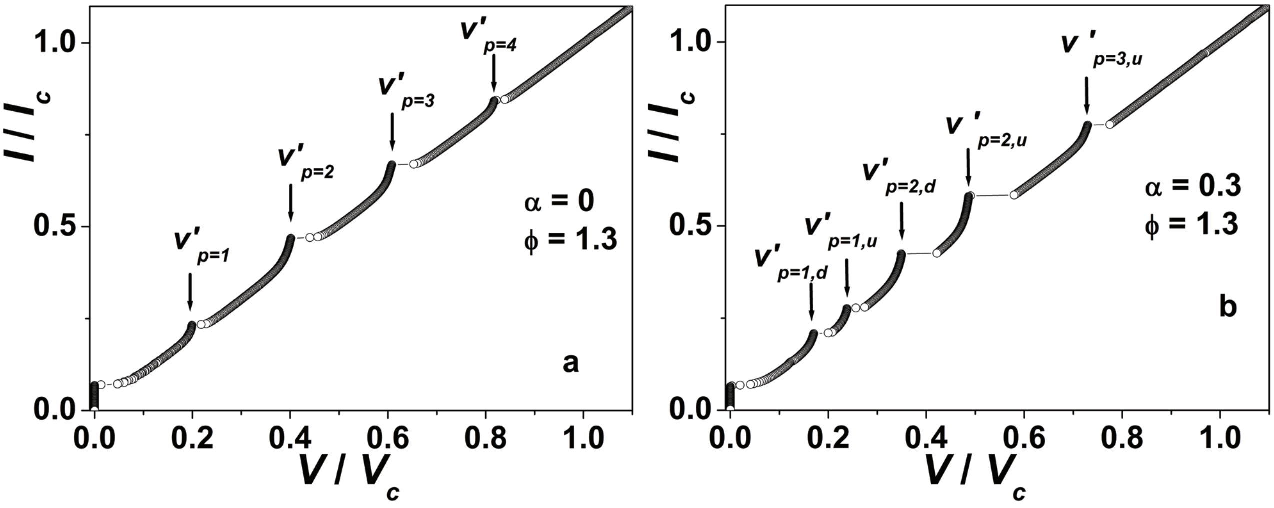

a *b*

Fig. 5. IV-characteristics of the stack of two wide junctions in magnetic field which corresponds to $\phi = 1.3$ for $\alpha = 0$ (a) and $\alpha = 0.3$ (b). Arrows mark values of $v'_p = V'_p / V_c$ in (a) and $v'_{p,d} = V'_{p,d} / V_c$, $v'_{p,u} = V'_{p,u} / V_c$ in (b) for different *p*.

in Fig. 3a. In the IV-characteristic of the stack with inductive coupling between junctions ($\alpha = 0.3$) each of the Fiske steps V'_p is split in two steps at voltages $V'_{p,d}$ and $V'_{p,u}$ like the zero-field step considered above. The first Fiske step $V'_{p=1} = 0.199 \cdot V_c$ splits to the lower step at $V'_{p=1,d} = 0.170 \cdot V_c$ and the upper step $V'_{p=1,u} = 0.238 \cdot V_c$ etc. We can conclude that the inductive interaction between junctions leads to the split of the Fiske steps too.

It is necessary to determine if amplitudes of these split steps obey the usual dependences of Fiske steps on applied external magnetic field. Therefore we calculated IV-characteristics at different values of the normalized magnetic flux and determined the dependence of the maximum Josephson current I_m of the stack on the value of ϕ. The dependence $I_m(\phi)$ is shown in Fig.6a by circles. This dependence has the usual Fraunhofer form (solid curve in Fig. 6a). We obtained also dependences of amplitudes of Fiske steps on ϕ. As we noted above, the application of the resistively shunted model for the description of wide Josephson junctions gives the possibility to determine only bottom parts of Fiske steps, so the height of the step can not be determined exactly. However, we can expect that the behaviour of remaining parts of steps obey the physical processes which take place when external magnetic field is applied to the system. Taking into account this consideration, we determined amplitudes of the first and the second Fiske steps $I^{F1,2} / I_c$ straightforward from IV-characteristics, plotted these amplitudes as functions of normalized magnetic flux and fitted obtained plots in ranges of the theory of Fiske steps by standard equations [9,14]:

$$I^{Fp}(\varphi) = I_c J_0\left(\frac{a}{2}\right) J_1\left(\frac{a}{2}\right) F_p(\varphi), \tag{10}$$

$$F_p(\varphi) = \frac{2}{\pi} \frac{\varphi\left|\sin\left(\pi\varphi - \pi\left(p/2\right)\right)\right|}{\left|\varphi^2 - p^2/4\right|}, \tag{11}$$

where *p* is the number of the Fiske step and $J_p(a/2)$ are Bessel functions of the *p*-th order. The parameter *a* is the root of the following equation [9]:

$$J_0\left(\frac{a}{2}\right) = \frac{a}{Z_p F_p(\phi)}, \tag{12}$$

where $Z_p = \left(\frac{D}{\lambda_J}\right)^2 \frac{Q_p}{\pi^2 p^2}$, Q_p is the quality factor for the *p*-th resonance. The plot of dependences $I_d^{F1}(\phi)/I_c$ and $I_u^{F1}(\phi)/I_c$ for both split steps is shown in Fig. 6b. The values of the amplitude of the upper step I_u^{F1} / I_c can not be determined in some interval of ϕ around the first maximum of $I_u^{F1}(\phi)/I_c$ (see Fig. 6b, triangles) because voltage jumps from the lower step to the hysteretic IV-curve. It is seen from Fig. 6b that the plot of the amplitude of the lower step I_d^{F1} on ϕ is satisfactory described by theoretical equations (10)-(12) (solid line in Fig. 6b). Because we can approximate only the part of the step, the found value of Q_1 = 37 can be treated only as a fitting parameter.

Amplitudes of split second Fiske steps on normalized

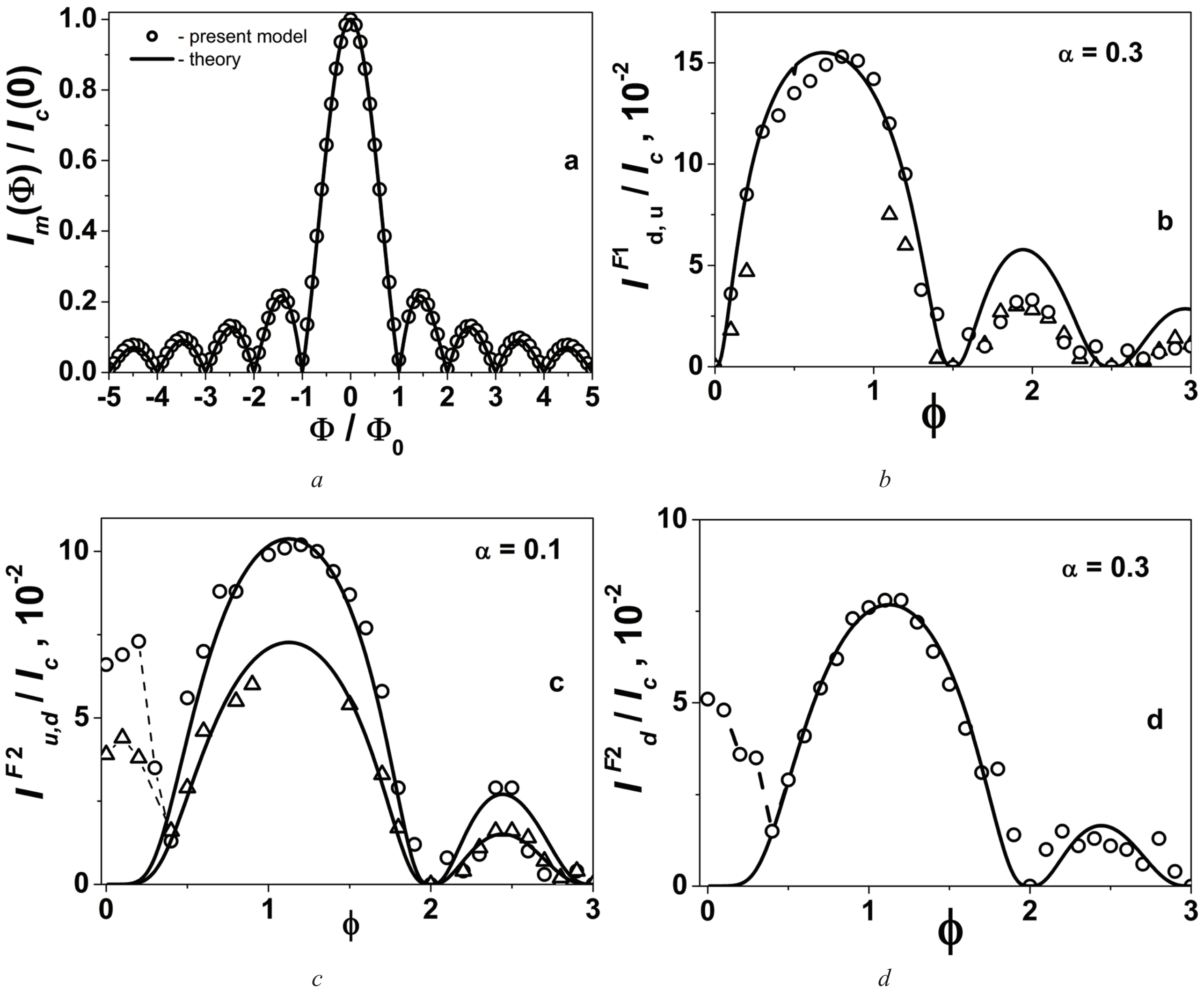

a *b*

c *d*

Fig. 6. (a) - the dependence of the normalized maximal Josephson current I_m / I_c on the normalized magnetic flux Φ / Φ_0 for the whole stack of two wide junctions; (b) - dependences $I_d^{F1}(\phi)/I_c$ and $I_u^{F1}(\phi)/I_c$ for the stack with $\alpha = 0.3$. Circles and triangles correspond to the lower and the upper step, correspondingly; (c) - dependences $I_d^{F2}(\phi)/I_c$ and $I_u^{F2}(\phi)/I_c$ for the stack with $\alpha = 0.1$. Circles and triangles correspond to the lower and the upper step, correspondingly; (d) - the dependence of $I_d^{F2}(\phi)/I_c$ for the stack with $\alpha = 0.3$. Solid lines in plots (b)-(d) are approximations by Eqs. (10)-(12).

magnetic flux are plotted in Fig. 6c for the system with $\alpha = 0.1$ and in Fig. 6d for the system with $\alpha = 0.3$ (in this plot only data for the lower step are shown). It is seen that in all cases maxima of dependences $I_d^{F2}(\phi)/I_c$ and $I_u^{F2}(\phi)/I_c$ for both lower and upper steps are satisfactory described by Eqs. (10)-(12) with $Q_2 = 97$ for the upper steps and $Q_2 = 110$ for the lower steps besides the interval $0 \le \phi \le 1/2$ (see Figs. 6c, d). The obtained in our model dependences $I_d^{F2}(\phi)/I_c$ and $I_u^{F2}(\phi)/I_c$ deviates drastically from the dependence predicted by Eqs. (10)-(12) in this interval of ϕ. The amplitude of the step decreases to some non-zero value and then at $\phi \ge 0.5$ it increases again according to the predicted behaviour of the second Fiske step. This deviation was found in the experiment with the single Josephson junction which revealed the zero-field step in the IV-characteristic [9,15]. Theoretical treatment of zero-field steps in the presence of multimode oscillations proved also such a form of the dependence $I^{F2}(\phi)/I_c$ for single junction [16]. We can conclude that the found form of the second Fiske step is characteristic for junctions which reveal zero-field steps. It is necessary to check this supposition experimentally and to investigate the physical origin of this effect in high-temperature superconductors.

Conclusions

In the present paper we investigated zero-field steps and Fiske steps in the stack of two interacting wide Josephson junctions with normal edges. Each of the wide junctions in the stack was modeled as a multijunction interferometer consisted of twenty ‘elementary junctions’. These ‘elementary junctions’ were described in the range of the resistively shunted model. In our model wide junctions in the stack can inductively interact with each other. Zero-field steps appear in IV-curves of the stack as a result of the interaction of Josephson generation with electromagnetic excitations which are introduced through normal edges. We found that due to the interaction, the zero-field step was split in two zero-field steps. Frequencies of split steps obeyed relations for inductively interacting resonance contours. We investigated also the behaviour of amplitudes of the first and the second Fiske steps in applied external magnetic field. Due to the inductive interaction between junctions, Fiske steps were also split. Dependences of amplitudes of the split first Fiske steps on the normalized magnetic flux were approximated by the theory with the satisfactory agreement, whereas the behaviour of the split second Fiske step at $\phi \le 0.5$ deviated from predictions of the theory.

1. S. Sakai and P. Bodin, N. F. Pedersen. J. Appl. Phys., 73, 2411 (1993).
2. R. Kleiner, P. Müller, H. Kohlstedt. N. F. Pedersen, S. Sakai. Phys. Rev. B50, 3942 (1994).
3. Hideki Matsumoto, Shoichi Sakamoto, and Fumihiro Wajima, Tomio Koyama, Masahiko Machida. Phys. Rev. B60, 3666 (1999).
4. M. Machida, T. Koyama, M. Tachiki. Phys. Rev. Lett. 83, 4618 (1999).
5. L. Ozyuzer, A. E. Koshelev, C. Kurter, N. Gopalsami, Q. Li, M. Tachiki, K. Kadowaki, T. Yamamoto, H. Minami, H. Yamaguchi, T. Tachiki, K. E. Gray, W.-K. Kwok, U. Welp. Science, 318, 1291 (2007).
6. B. Gross, S. Guénon, J. Yuan, M. Y. Li, J. Li, A. Ishii, R. G. Mints, T. Hatano, P. H. Wu, D. Koelle, H. B. Wang, and R. Kleiner. Phys. Rev. B 86, 094524 (2012).
7. Alexander Grib. Visnyk Kharkivs’kogo Natsional’nogo Universitetu imeni V. N. Karazina, N1135, ser. "Fizika" 21, 61 (2014).
8. T. A. Fulton and R. C. Dynes. Solid State Commun., 12, 57 (1973).
9. Antonio Barone and Gianfranco Paternò. Physics and applications of the Josephson effect, A Wiley-Interscience Publication, New York (1982), 529 p.
10. K. K. Likharev. Dynamics of Josephson junctions and circuits, Gordon and Breach, Philadelphia. (1991), 750 p.
11. Alexander Grib and Paul Seidel., J. Phys.: Conf. Ser., 507, 042038 (2014).
12. Alexander Grib and Paul Seidel. Low Temp. Phys. 38, 321 (2012).
13. N. F. Pedersen and D. Welner. Phys. Rev. B29, 2551 (1984).
14. I. O. Kulik. Zh. Tekh. Fiz., 37, 157 (1967) [Sov. Phys. Tech. Phys., 12, 111 (1967)].
15. G. Paternò and J. Nordman. J. Appl. Phys, 49, 2456 (1978).
16. K. Enpuku, K. Yoshida, and F. Irie. J. Appl. Phys. 52, 344 (1981).

Вісник ХНУ, № 1158, серія «Фізика», вип. 22, 2015. с. 58-62

УДК 536.94:538.945.6
PACS 74.40.De, 85.25.Dq

Experimentally controlled stochastic resonance in a superconducting quantum interferometer

O.G. Turutanov

B. Verkin Institute for Low Temperature Physics and Engineering,
NAS of Ukraine, 47 Lenin ave., 61103 Kharkov, Ukraine

The stochastic resonance effect is observed experimentally in a niobium superconducting quantum interferometer (RF SQUID loop) and manifests itself in a non-monotonic rise of the gain of a weak low-frequency harmonic signal which peaks at a certain level of Gaussian quasi-white noise flux inside the loop. It is shown experimentally that the gain of the weak harmonic signal can be varied and maximized when the noise flux intensity is insufficient to realize the SR condition by introducing a deterministic ac magnetic flux into the loop, the ac flux frequency highly exceeding the useful signal frequency.

Keywords: RF SQUID, stochastic resonance, controllable stochastic resonance, ScS contact, Josephson junction.

В одноконтактном ниобиевом сверхпроводящем квантовом интерферометре (кольце ВЧ СКВИДа) экспериментально наблюдается эффект стохастического резонанса, выражающийся в немонотонном росте усиления слабого низкочастотного гармонического сигнала, которое достигает максимума при определенном уровне квазибелого гауссова шумового потока, вносимого в кольцо. Экспериментально показано, что при интенсивности шумового потока, недостаточной для реализации условия стохастического резонанса, можно регулировать стохастическое усиление слабого гармонического сигнала и достичь его максимально возможного значения путем внесения в кольцо детерминированного переменного магнитного потока с частотой, значительно превышающей частоту усиливаемого полезного сигнала.

Ключевые слова: ВЧ СКВИД, стохастический резонанс, управляемый стохастический резонанс, ScS-контакт, контакт Джозефсона.

У одноконтактному ніобієвому надпровідному квантовому інтерферометрі (кільці ВЧ НКВІДу) експериментально спостерігається ефект стохастичного резонансу, що виражається в немонотонному зростанні посилення слабкого низькочастотного гармонійного сигналу, яке досягає максимуму при певному рівні квазібілого гаусового шумового потоку, що вноситься до кільця. Експериментально показано, що при інтенсивності шумового потоку, недостатній для реалізації умови стохастичного резонансу, можна регулювати стохастичне посилення слабкого гармонійного сигналу і досягти його максимально можливого значення шляхом внесення до кільця детермінованого змінного магнітного потоку з частотою, що значно перевищує частоту підсилюваного корисного сигналу.

Ключові слова: ВЧ НКВІД, стохастичний резонанс, керований стохастичний резонанс, ScS-контакт, контакт Джозефсона.

Introduction

The Superconducting Quantum Interference Devices (SQUIDs) based on low- and high-T_c superconductors are the key element in designing the most sensitive magnetometers widely used in laboratory setups, industry equipment, biomedical applications, geophysics, etc. The sensitivity of SQUIDs, usually degraded in a noisy environment, can, however, be enhanced [1-6] due to the same thermodynamic fluctuations and the external noise by using the stochastic resonance (SR) effect.

The SR conception was coined in the early 1980s [7,8]. The SR manifests itself in various ways, the most obvious one is a non-monotonic rise of the response of a non-linear system to a weak informational (often periodic) signal. As a result, the signal is amplified and peaks at a certain noise intensity. Other signal "quality characteristics" (e.g., signal-to-noise ratio) become better, too, at the system output. To make the SR possible in a specific system, the time duration for which the system exists in one of its metastable states (MS) (the residence time) must be a function of the noise intensity. The SR effect has been found in numerous natural and artificial systems, both classic and quantum. Till now, a lot of detailed analytical and experimental studies of the SR were performed, the criteria and quantifiers to estimate the noise-induced ordering were elaborated [9,10]. For the aperiodic systems with strong dissipation (which are mostly explored both theoretically and experimentally), the "stochastic filtration" (SF) is rather more correct term than the widely accepted "stochastic resonance" [11)].

Although a noticeable number of the theoretical and modeling studies of the SR in the superconducting loop are published, there is still a lack of the experimental investigations of the stochastic dynamics in SQUIDs [12] (e.g., [1-3]). Therefore some interesting challenges remain in this field, including possible practical applications. One of such problems is the issue of maximizing the signal gain while stochastically amplified at a non-optimal noise level.

If the barrier height is fixed, the optimal stochastic gain can be achieved by varying the noise intensity [9,10], but in most practical cases the noise intensity may be suboptimal while a change in the device temperature is undesirable. The SR gain can be controlled by changing the interferometer parameters (mainly the Josephson junction critical current; the loop inductance is hardly changeable) but this will alter the “operation point” of the device which incorporates the interferometer. Therefore, more convenient mechanisms controlling the stochastic signal amplification at suboptimal noise in the SQUID should be looked for. A noticeable number of methods to control the stochastic gain in various system including SQUIDs were suggested such as re-normalizing the potential barrier height in a single-junction interferometer by microwave field [13] (this effect was later [14] utilized to parametrically amplify a weak informational signal in an RF SQUID with microwave pumping), dynamic violation of symmetry of a model potential by mixing two harmonics with various amplitudes and initial phase shift [15], by changing the threshold of a Schmitt trigger with frequency of the input signal [16] and by system flip-over in a certain time with a pulse signal [17], etc. We should like to notice the theoretical work [18] suggested an approach to control the SR which is similar to that we realized experimentally; the substantial differences we will discuss below.

This work reports the experimental results demonstrating a possibility of controlling the stochastic amplification of a weak signal in an RF SQUID loop by introducing a periodic ac magnetic flux into the loop whose frequency is much higher than the signal frequency and amplitude is large enough to ensure an increase in the mean rate of transitions of the loop between its metastable current (magnetic) states. We found this effect earlier [19] by numerical simulation of the magnetic flux dynamics in an RF SQUID loop and called it “stochastic-parametric resonance”.

RF SQUID dynamics and experimental

RF SQUID loop is the “heart” of RF SQUID magnetometers. It is a superconducting loop with inductance L interrupted by a Josephson junction with critical current I_c, normal resistance R and capacitance C (Fig. 1,a). Assuming sinusoidal current-phase relation $I_s(\varphi) = I_c \sin\varphi$ for the Josephson junction, the RF SQUID potential energy, which is the sum of the loop

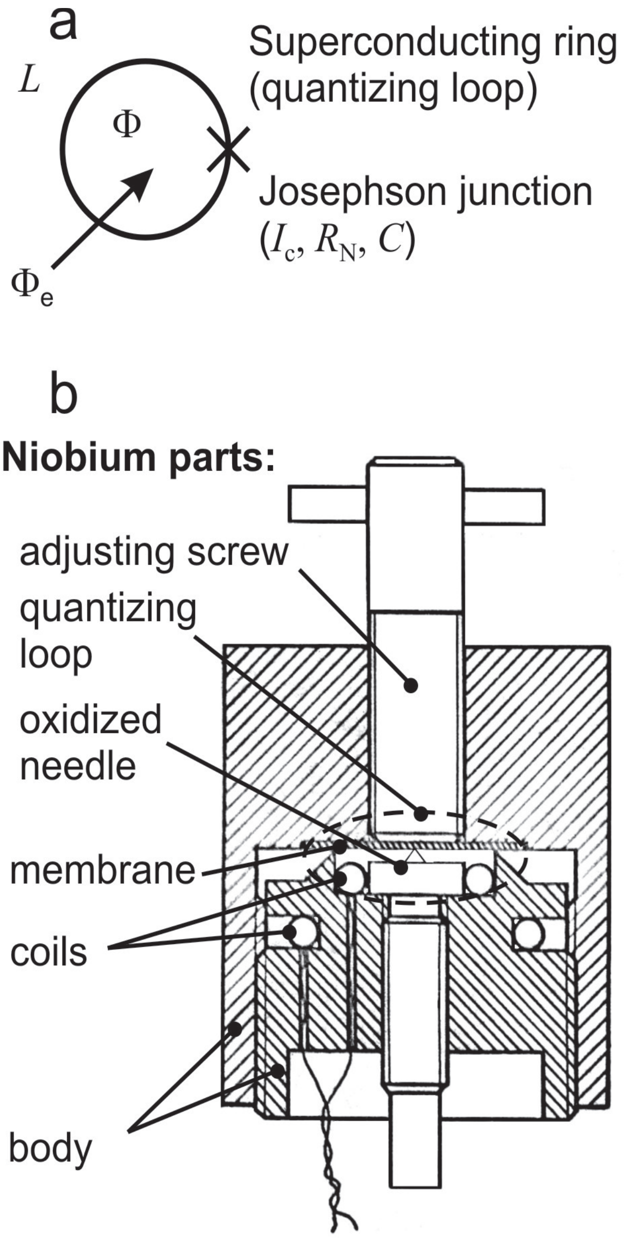

Fig. 1. (a) Principal schematic of the RF SQUID loop; the parameters are explained in the text. (b) Practical design of the RF SQUID loop as a 3D self-shielded toroidal construction with adjustable point Josephson contact, tank, transformer and input coils, all the parts are made of pure niobium except the tank and input copper-wire coils.

magnetic energy and the coupling energy the Josephson junction, in dimensionless units reads

$$u(x, x_e) = (x - x_e)^2 / 2 - \frac{\beta_L}{4\pi^2}\cos(2\pi x), \quad (1)$$

where $x = \Phi / \Phi_0$ and $x_e = \Phi_e / \Phi_0$ are dimensionless internal and external magnetic fluxes, correspondingly, $\Phi_0 \approx 2.07 \cdot 10^{-15}$ Wb is the magnetic flux quantum, $\beta_L = 2\pi L I_c / \Phi_0$ is dimensionless parameter of non-linearity; the energy is normalized to $\Phi_0^2 / 2L$. The β_L

parameter defines the number and depth of the local minima of the SQUID potential energy, the potential becomes two- or multi-well when $\beta_L > 1$.

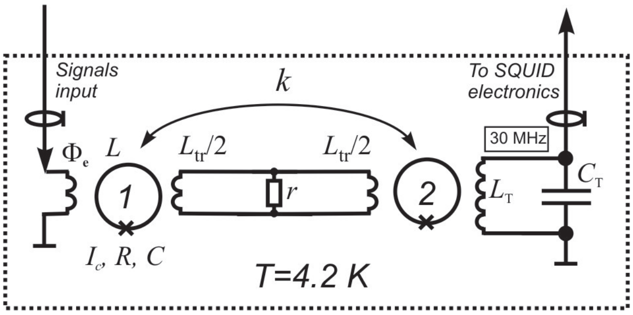

Fig. 2. The simplified diagram of the measurements. External magnetic flux Φ_e is applied by a coil to the loop of the interferometer-under-test (denoted by number 1). The in-loop flux is measured with RF SQUID magnetometer (denoted by number 2) via the superconducting magnetic flux transformer. The coupling coefficient between the loops is denoted by k. The dotted line indicates the superconducting led shield.

Real device, keeping topology of a ring, is usually a much more complicated unit than the schematic view of Fig. 1,a. Our interferometer-under-test was designed as the niobium 3D self-shielded toroidal construction with the adjusted point contact (Fig. 2,b). The device design is described in detail in [20]. In our experiments we tested the interferometers with $\beta_L \approx 4.7 - 5.4$ and low impedance ($R \sim 1\,\Omega$) Josephson junctions of the ScS (superconductor-constriction-superconductor) type having low intrinsic capacitance ($C \approx 3 \cdot 10^{-15}$ F), the toroidal loop inductance being $L \approx 3 \cdot 10^{-10}$ H. Such a parameter value set (the smallness of C and R) determines the overdamped regime of the SQUID as a stochastic oscillator and allowed us to neglect the second derivative in the flux motion equation [21] and reduce it to the form convenient for calculations and computer simulations [4-6]:

$$\frac{dx}{dt} = \frac{1}{\tau_L}\left[x_e(t) - x + \frac{\beta_L}{2\pi}\sin(2\pi x) \right], \qquad (2)$$

where $\tau_L = L/R$ is the loop flux decay time. As seen, the equation describes an aperiodic system. The external flux x_e is the sum of the fixed bias flux ($x_{dc} = 0.5$) symmetrizing the potential, the weak low-frequency signal $x_s = a\sin 2\pi f_s t$ (a<<1), uncorrelated (white) Gaussian noise $x_N = \xi(t)$, $\langle \xi(t) \cdot \xi(t') \rangle = 2D\delta(t - t')$, where D is the noise intensity (variance), and a high-frequency "pumping" $x_p = A\sin 2\pi f_p t$ with f_p>>f_s and the amplitude A comparable with the noise mean-square amplitude $s = D^{1/2}$. In both in the calculations and the experiments the noise is frequency-band limited by a cut-off frequency f_c. To consider it practically uncorrelated in the context of discussed SR model, the cut-off frequency should sufficiently exceed the signal frequency: f_c>>f_s. In our experiments we chose $f_s = 37\ Hz$, $f_c = 50\ kHz$ and $f_p = 50\ kHz$. The Gaussian noise was generated by a real physical source (diode) and went through low-pass filters.

The interferometer-under-test (denoted by 1 in Fig. 2) was coupled to an instrumental RF SQUID magnetometer (denoted by 2 in Fig. 2) via the superconducting magnetic flux transformer L_{tr} with the interferometer loop-to-loop flux coupling coefficient $k = 0.05$. The resistor $r = 0.3\,\Omega$ shunted the transformer forming a low-pass filter with the cut-off frequency r / L_{tr}. It eliminated the influence of the RF (30 MHz) pumping oscillations in the instrumental SQUID tank circuit $L_T C_T$ onto the interferometer-under-test. The spectral density of the magnetic flux noise (the sensitivity) of the magnetometer was $S_\Phi^{1/2} \approx 2 \cdot 10^{-4}\ \Phi_0 / Hz^{1/2}$ in the operation frequency band of 2 to 200 Hz. The coupling coefficients, the fluxes and the coil RF currents were determined from the measurements of the amplitude-frequency and the amplitude-flux characteristics of the interferometer-under-test while changing the loop flux within $\pm 5\Phi_0$. The experimental setup is similar ideologically to that reported in [2] and will be described elsewhere. The measurements were taken at temperature 4.2 K inside a superconducting shield. The cryostat was placed into a three-layer mu-metal shield. The output signal was fed to the spectrum analyzer Brüel&Kjær model 2033. The number of the instrumentally averaged spectra was 16.

Results and discussion

The numerical calculations [1,2,4-6] showed that the spectrum density of the internal flux in the SQUID loop at the frequency of the useful signal rapidly rises, peaks and then slowly decreases with the increase of the Gaussian noise intensity D, in accordance with the theory [9,10].

Fig 3 displays the experimentally obtained amplitude spectral density $S_\Phi^{1/2}(f_s)$ of the flux Φ inside the interferometer loop at the information signal frequency f_s as a function of mean-square amplitude of the Gaussian noise $D^{1/2}$. The amplitude of the harmonic information signal inside the interferometer-under-test was $a = 0.05$ in Φ_0 units, $\beta_L = 4.71$. The interferometer behavior is typical for the scenario of SR (or SF) in a bi-stable system. The maximum gain of about 10 dB was obtained in this

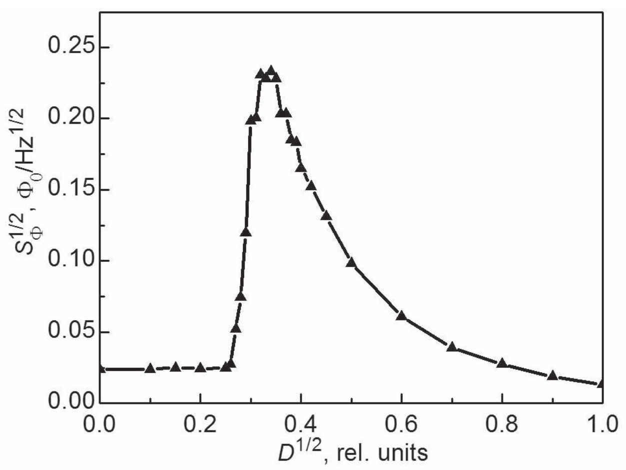

Fig. 3. The amplitude spectral density $S_\Phi^{1/2}(f_s)$ of the magnetic flux inside the RF SQUID loop at the signal frequency f_s as a function of the mean-square amplitude $D^{1/2}$ of the Gaussian noise. The signal amplitude $a = 0.05\ \Phi_0$, the signal frequency $f_s = 37\ Hz$, the noise cut-off frequency $f_c = 50\ kHz$, the non-linearity parameter $\beta_L = 4.71$, the temperature $T = 4.2\ K$.

experiment. It is interesting to note that the exact shape of this "classical" SR curve turns out to be fairly sensitive to the specific potential relief $U(\Phi)$. Verifying the curve by a numerical simulation, we found that the best fit corresponded to the model of ScS Josephson contact at a finite temperature [22] rather than traditionally used tunnel junction model (1) or even ScS contact model at zero temperature [6]. Although the niobium needle is thermally oxidized (Fig. 1,b) and the critical current calculated from the expression for β_L was small enough ($I_c = 5.2\ \mu A$), the real structure of the point contact may involve both tunnel and direct conductivity in various proportions making difficult to formulate an exact adequate model for its description. The curve comparison with various models and the details of the fitting procedure will be discussed in further papers.

We showed earlier [19] by a computer simulation that the SR signal gain can be maximized at an insufficient noise level by introducing a high-frequency field into the interferometer. We called this cooperative effect "stochastic-parametric resonance" because the high-frequency field affects the Josephson inductance as a device parameter. However, many various signal combinations were proposed to control the SR gain (see Introduction) that way or another changing the potential. Particularly, the difference may lie in the auxiliary signal frequency: if it is higher than the loop response time L/R then it works much like the temperature, really re-normalizing the barrier height [23]. Our case is adiabatic one, f_p<<L/R. To distinguish the effect discussed here, it is probably better to call it "deterministically-assisted stochastic resonance" (DASR). In the work [18] we found theoretical elaboration of a similar idea but the authors added an ac field with a frequency only 2-3 times higher than the weak signal frequency and analyzed both commensurate and incommensurate cases. We propose [19] "noise-substituting" periodic oscillations with a frequency that substantially exceeds the weak signal frequency, $f_p > 10 f_s$; practically, $f_p \approx 1000 f_s$.

Figure 4 shows the experimental curves of the amplitude spectral density $S_\Phi^{1/2}(f_s)$ of the internal magnetic flux Φ at the signal frequency f_s vs. amplitude A of the ac magnetic flux (high-frequency pumping) at various noise levels $D^{1/2}$. It is seen that if the noise intensity is lower than the optimal value necessary for obtaining maximum stochastic amplification (compare with Fig. 3), then the maximal gain can be reached through additional high-frequency pumping. Since f_p>>f_s, there is no experimental difference between frequency-commensurate and incommensurate modes. All the

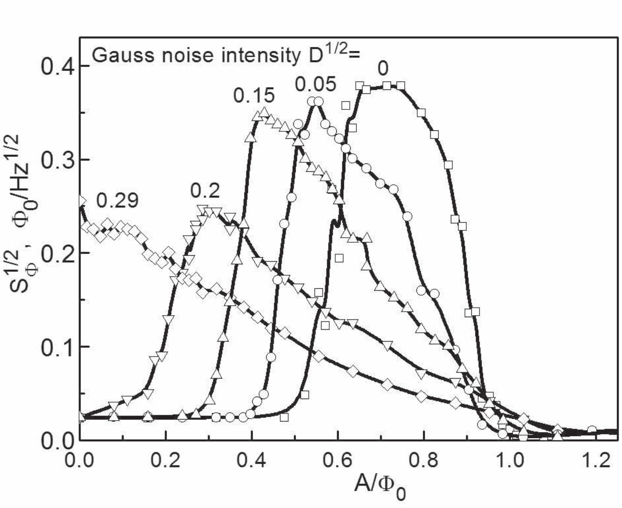

Fig. 4. The amplitude spectral density $S_\Phi^{1/2}(f_s)$ of the magnetic flux inside the RF SQUID loop at the signal frequency f_s as a function of the high-frequency ac magnetic flux A expressed in Φ_0 units at various sub-optimal mean-square amplitudes $D^{1/2}$ of the Gaussian noise indicated neae each curve). The signal amplitude $a = 0.05\ \Phi_0$, the signal frequency $f_s = 37\ Hz$, the noise cut-off frequency $f_c = 50\ kHz$, the sinusoidal ac flux frequency $f_p = 50\ kHz$, the non-linearity parameter $\beta_L = 4.71$, the temperature $T = 4.2\ K$.

unwanted intermodulation products are far-spaced in the frequency domain and can be easily filtered out. Thus, this effect can be used in SQUID-based instruments (and other devices because of its universality) for fine tuning the stochastic amplification gain. Further investigation may include a change in signal-to-noise ratio, non-linear distortion, amplified frequency band, etc., as compared to classical SR.

Conclusion

1. The stochastic resonance effect in a single-junction superconducting quantum interferometer (RF SQUID) manifesting itself in an amplification of a weak harmonic low-frequency signal is experimentally observed.

2. The SR-like effect of a weak signal amplification, that we found earlier by numerical modeling, but caused, unlike SR, by the action of a periodic (deterministic) high-frequency field and the cooperative action of both this field and the noise flux inside the system is experimentally proved. We suggest designating it as "deterministically-assisted stochastic resonance" (DASR).

3. A possibility of controlling the stochastic amplification of a weak harmonic signal and maximizing the signal gain at a suboptimal noise level using the DASR effect is experimentally demonstrated.

4. A statement concerning the most adequate model of the Josephson contact incorporated in the interferometer-under-test is made which requires a further numerical analysis.

1. R. Rouse, S. Han, J.E. Lukens, Appl. Phys. Lett. 66, 108 (1995).
2. A.D. Hibbs, A.L. Singsaas, E.W. Jacobs, A.R. Bulsara, J.J. Bekkedahl et al., J. Appl. Phys. 77, 2582 (1995).
3. A.D. Hibbs, B.R. Whitecotton, Appl. Supercond. 6, 495 (1998) .
4. O.G. Turutanov, A.N. Omelyanchouk, V.I. Shnyrkov, Yu.P. Bliokh, Physica C 372–376, 237 (2002).
5. A.M. Glukhov, O.G. Turutanov, V.I. Shnyrkov, A.N. Omelyanchouk, Low Temp. Phys. 32, 1123 (2006).
6. O.G. Turutanov, V.A. Golovanevskiy, V.Yu. Lyakhno, V.I. Shnyrkov, Physica A 396, 1 (2014).
7. R. Benzi, A. Sutera, A. Vulpiani, J. Phys. A 14, L453 (1981).
8. C. Nicolis, G. Nicolis, Tellus 33, 225 (1981).
9. L. Gammaitoni, P. Hänggi, P. Jung, F. Marchesoni, Rev. Mod. Phys. 70, 223 (1998).
10. V.S. Anishchenko, A.B.Neiman, F. Moss, L. Shimansky-Geier, Phys. -Usp. 42, 7 (1999).
11. Yu. L. Klimontovich, Phys. -Usp. 42, 37 (1999).
12. A.R. Bulsara, Nature 437, 962 (2005).
13. V.I. Shnyrkov, V.A. Khlus, G.M. Tsoi, J. Low Temp. Phys. 39, 477-496 (1980).
14. V.I. Shnyrkov, Yu.P. Bliokh, XII Trilateral German-Russian-Ukrainian Seminar on High-Temperature Superconductivity, Program and Abstracts, Kiev: 1999, P.81.
15. G. Schmid, P. Hänggi, Physica A. 351, №1.-P.95-105.
16. L. Gammaitoni, M. Löcher, A. Bulsara, P. Hänggi, J. Neff, K. Wiesenfeld, W. Ditto, M.E. Inchiosa, Phys. Rev. Lett. 82, 4574 (1999).
17. J. Mason, J.F. Lindner, J. Neff, W.I. Ditto, A.R. Bulsara, M.L. Spano, Phys. Lett. A 277, 13 (2000).
18. S. Savel'ev, A.L. Rakhmanov, and F. Nori, Phys.Rev.E. 72, 056136 (2005).
19. O.G. Turutanov, V.I. Shnyrkov, A.M. Glukhov, J. Low Temp. Phys. 34, 37 (2008).
20. V.I. Shnyrkov, A.A. Soroka, and O.G. Turutanov, *Phys. Rev. B* **85**, 224512 (2012).
21. A. Barone, G. Paterno, Physics and Applications of the Josephson Effect, Wiley, New York, 1982.
22. O.G. Turutanov, V.Yu. Lyakhno, and V.I. Shnyrkov, arXiv.org:1506.00953.
23. V.A. Khlus, Sov. J. Low Temp. Phys. 12 (1986) 14.

Вісник ХНУ, № 1158, серія «Фізика», вип. 22, 2015. с. 63-67

PACS:
74.78.Fk Multilayers, superlattices, heterostructures
74.25.F Transport properties
74.40.Kb Quantum critical phenomena
УДК 538.945

Influence of transport current on the magnetic field induced superconductor-insulator transition in PbTe/PbS heterostructures

O.I.Yuzephovich[1,2]

[1] *B. I. Verkin Institute of Low-temperature Physics and Engineering, Lenina ave. 47, 61103 Kharkov, Ukraine*
[2] *International Laboratory of High Magnetic Fields and Low Temperatures, 530421 Wroclaw, Poland*
yuzephovich@ilt.kharkov.ua

Transport properties of semiconductor heterostructures PbTe/PbS with a superconducting interface are studied. The influence of the electric current on the resistive state of the heterostructures is investigated. The possibility of the realization of the electric current induced superconductor-insulator transition is shown. The temperature dependence of critical magnetic fields of the transition is obtained.

Keywords: superconductivity, quantum superconductor-insulator transition, semiconductor heterostructures.

Проведено вимірювання транспортних властивостей напівпровідникових гетероструктур PbTe/PbS з надпровідним інтерфейсом. Досліджено вплив транспортного струму на резистивний стан гетероструктур. Продемонстровано можливість реалізації в таких структурах індукованого транспортним струмом переходу надпровідник-ізолятор. Одержано залежність критичного магнітного поля переходу від температури.

Ключові слова: надпровідність, квантовий фазовий перехід надпровідник-ізолятор, напівпровідникові гетероструктури.

Проведены измерения транспортных свойств полупроводниковых гетероструктур PbTe/PbS со сверхпроводящим интерфейсом. Исследовано влияние транспортного тока на резистивное состояние гетероструктур. Продемонстрирована возможность реализации в таких структурах индуцированного транспортным током перехода сверхпроводник-изолятор. Получена зависимость критического магнитного поля перехода от температуры.

Ключевые слова: сверхпроводимость, квантовый фазовый переход полупроводник-изолятор, полупроводниковые гетероструктуры.

Introduction

In this paper we present the results of an experimental study of the influence of electric current and strong magnetic fields on the superconducting state of nanostructures that formed on the interface between semiconducting layers of the epitaxial PbTe/PbS heterostructures [1, 2, 3, 4, 5, 6]. Here, we examine the possibility of the transport current induced quantum superconductor-insulator phase transition (SIT) [4].

Superconductor-insulator phase transitions have been intensively studied for the last time. They are found experimentally in a number of low-dimension systems such as ultrathin amorphous films, granular films, and arrays of Josephson junctions. This phenomenon occurs when the internal parameters of the system (such as disorder or film thickness) change or under the influence of external impact such as magnetic fields H, electric fields or transport currents I. Superconductor insulator transitions have also been observed experimentally in HTSC compounds and even in one-dimensional long nanowires. Features of SIT depend on the material properties and the experimental conditions [7, 5]. The nature of the superconductor-insulator transition is still an open question.

Interpretation of the superconductor-insulator transition observed experimentally in uniform thin disordered films is sufficiently complicated. As an example, for films with relatively low resistance R per square the characteristic features of SIT can be explained by quantum mechanical corrections to the conductivity [6]. In this case, on the insulating side there will be a slight increase of no more than 10% in the resistance. In the case of a large increase in the resistance on the insulating side induced by a magnetic field, the superconductor-insulator transition in uniform thin disordered films is most often explained by Fisher's scaling theory [7] (a theory of duality between Cooper pairs and vortices). It is assumed that at $T \to 0$

delocalized Cooper pairs and localized vortices exist below the transition at $H<H_c$ (superconductor), and localized pairs with delocalized vortices above the transition $H>H_c$ (insulator). The magnetic field and temperature dependence of the resistance per square follow the scaling law for phase transitions $R(\delta\ T) = R_c F(\delta x / T^{1/\nu z})$, where F is a constant introduced to maintain the dimensionality of the equation; δ is a variable parameter that drives the phase transition, in this case, a magnetic field with $\delta=|H-H_c|$; and, νz is the critical exponent. The model predicts that the critical resistance per square R_c should equal the universal quantum resistance $R_Q = h/4e^2 = 6.5$ kOhm. The scaling law proposed for the resistance by Fisher [10] is in good agreement with a variety of experimental data [see reviews 7, 8]. Nevertheless, many experiments have yielded a large scatter in the values for the critical resistance and the critical exponent νz. Thus, one of the main predictions of Fisher's theory (a universal quantum resistance) is not observed experimentally in all systems during superconductor-insulator transitions.

In granular systems with small granules [8, 9] and artificially prepared regular arrays of Josephson junctions, [10, 11, 12, 13] the SIT can be explained by a competition between the inter-granule Josephson binding energy J and the charge Coulomb energy E_C of an individual granule. When $E_c>>J$ Coulomb blockade predominates. As a result, Cooper pairs become localized and the system transforms into an insulating state. If, on the other hand, the granules are larger, then Coulomb blockade is not effective and SIT takes place due to disruption of the Josephson links by an external impact (e.g., magnetic field). Single particle transport is also blocked because of the need to overcome a potential barrier comparable to the superconductor gap energy [7]. The Josephson coupling between granules is affected by both magnetic field and electric current. Thus it may be possible to observe the transport current induced superconductor-insulator transition.

Here, the two-layer semiconductor PbTe/PbS heterostructures are studied for the SIT. Interest in research on this heterostructures arises from the possibility of creating superconducting nanostructures with different topologies in a controlled fashion at their interface. We have found [3–6] that superconductivity of the interface of $A^{IV}B^{VI}$ heterostructures is related to an inversion of bands in the narrow-band semiconductors (PbTe, PbS, PbSe) owing to inhomogeneous elastic stresses along a network of misfit dislocations produced at the interface during pseudomorphic epitaxial growth. The period of the superconducting nanonetwork is equal to the period of the network of misfit dislocations and ranges from 3.3–40 nm, depending on the combination of semiconductors. For PbTe/PbS heterostructures it equals 5.2 nm. Thus, by varying the heterostructure parameters, such as the thickness of the semiconductor layers and the number of them, we can create arrays of individual quantum dots with weak Josephson links, as well as continuous superconducting nanonetworks and quasi-three dimensional multilayer structures (superlattices). These superconducting nanostructures have properties inherent in 0 -, 1 -, 2 -, and 3-dimensional systems. Thus, semiconducting PbTe/PbS heterostructures can serve as model objects for the study of effects of the localized superconductivity such as the superconductor-insulator transition. In fact, in our previous works the SIT was found in the heterostructures [14, 15].

It was established that the discontinuity of the superconducting interface is a necessary condition for the magnetic field induced superconductor-insulator transition observation and has a significant influence on its features: a fan-like set of resistance curves *R(T),* intersection of the *R(H)* curves and negative magnetoresistance. A scaling analysis based on Fisher's theoretical model was carried out for these samples. No evidence of a SIT was observed in heterostructures with a perfect interface. It appears that the SIT is related to percolation phenomena inherent in granular superconductors. Up to now the effect of transport current on the magnetic field induced SIT in these structures has not been studied. In the present work we investigate the influence of transport current on the magnetic field induced superconductor-insulator transition in heterostructures PbTe/PbS.

Samples preparation and measurement methods

Two-layer heterostructures were fabricated by sequential condensation of the vapors of the corresponding semiconductors on a freshly cleaved (001) surface of single crystal KCl at 520–570K in an oil-free vacuum of 10^{-6} Torr. The thickness d of each layer was 80nm. Deposition rate was monitored *in situ* using a quartz resonator. The first layer on the substrate always was PbS and the second one was PbTe. These semiconductors have a NaCl-type crystal structure with a small misfit (8%) between the parameters of the unit cells. During epitaxial growth the pseudomorphic stress relaxes through formation of a network of edge misfit dislocations at the interface. When a critical thickness d_c of the upper PbTe layer is reached (about 1-2nm) the first islands of misfit dislocation network arise at the interface [6, 16]). Further thickness increase leads to the merging of the islands and at thickness 100 nm a continuous square network of edge misfit dislocations covers the entire interface [6].

Transport measurements were made in a helium cryostat equipped with a 14T superconducting Oxford Instrument magnet. The accuracy of the temperature stabilization was 10^{-3} K. The resistance R was measured by the four-probe method. The direction of the dc transport current I is parallel to the plane of the sample and $\mathbf{I} \perp \mathbf{B}$. The upper critical magnetic fields B_{c2} were determined from the resistive transitions at the point $R = R_n / 2$, where

R_n is the resistance before the superconducting transition.

Experimental data and interpretation

Earlier it was found that two-layer PbTe/PbS heterostructures can be divided nominally into 3 categories [6], although there is no sharp boundary between these categories.

The first category includes samples with semiconducting layer thicknesses d>80 nm. They have a metallic conductivity in the normal state. The ratio of the resistance at room temperature to the resistance before the onset of the superconducting transition ($r=R_{300}/R_{\mathrm{n}}$) varies from 2 to 8. The corresponding critical temperatures T_c lie in the interval 4.2–6.5K. For samples from this category SIT has not been found.

The second category includes samples with thicknesses of 50–80 nm. This category can be referred to as intermediate. A sample in the normal state can exhibit both metallic conductivity and semiconductor behavior. But in any case at low temperatures it enters a superconducting state. The critical temperature ranges from 2.3–3.3K and r ranges from 0.9 to 1.7. Samples from this category always reveal all SIT features [17,18].

The third category includes samples with d<50 nm. The *R(T)* curves in the normal state for these samples are always characterized by a negative resistance coefficient *dR/dT* above T_c. The resistance per square R_{sq} exceeds 1.5 kOhm and r<1. For these systems T_{c} is often below 1K and they undergo an unending transition into the superconducting state down to the lowest temperatures at which the experiments were carried out (0.3 K), or they do not go into the superconducting state at all. The samples from this category can reveal initial features of SIT [18].

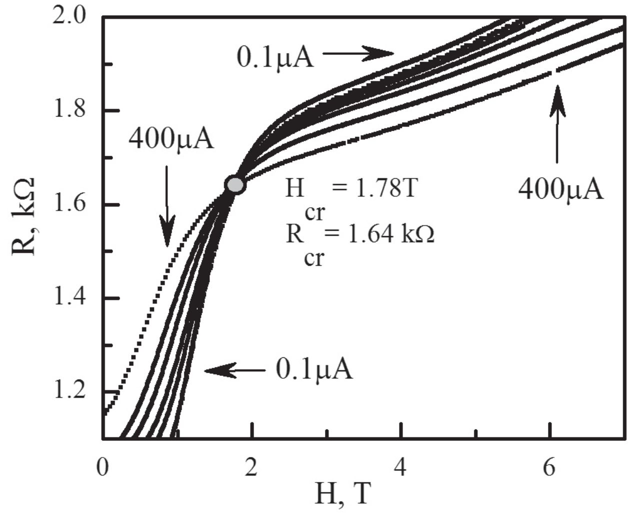

Fig.1. R(H) for different transport currents in a magnetic field parallel to the interface; d=80 nm. T=1.8K.

We will focus our attention on the samples from the second category for which two types of evolution of the *R(T)* curves in magnetic fields were observed. The first type, illustrated in Fig.1 in Ref.17, is characterized by the presence of a horizontal separatrix that clearly separates the $R(T)$ curves which move downward with the temperature decrease (superconductor) from the curves which move upward (insulator). This "fanlike" set of curves is regarded as an "ideal" case of SIT [7] and was observed in the heterostructures with the semiconductor layer thicknesses d=70-80 nm. For samples with d=40-70 nm the second type of the $R(T)$ curves set with tilted or non-monotonic sepratrix is observed [17, 18] which is out of the framework of this article.

For samples with the horizontal separatrix we always see another distinctive sign of the SIT – a single cross point of magnetic field dependences of the resistance $R(H)$ at different temperatures (Fig. 2 in Ref17).

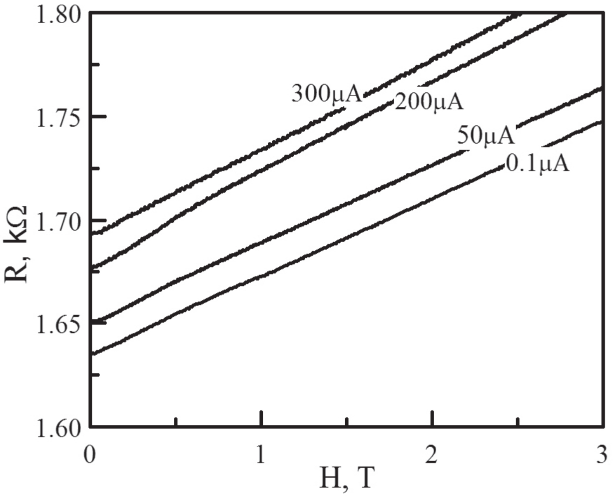

Fig.2. R(H) for different transport currents in a magnetic field parallel to the interface; d=80 nm. T=6.5K.

In this work the resistance dependences on magnetic field at different transport currents and fixed temperature are presented for the PbTe/PbS heterostructure with d=80 nm. It can be seen (Fig.1) that all $R(H)$ curves corresponding to different transport currents intersect precisely at the single point like at different temperatures on the Fig2 in Ref.17. The critical parameters H_{cr} =1.78 T, R_{cr} =1.64 Ohm for the temperature T=1.8K obtained for cross point. At the temperatures higher than critical temperature ($T>T_c$), magnetic field dependences at different transport current do not intersect, and SIT is not observed (Fig.2).

Superconducting areas at the interface may be considered like superconducting granules. Resistance of the whole system is determined by the resistance of granules and intergranular spacers. At sufficiently low temperatures and the absence of external influences the whole system is in a coherent superconducting state. Granules are superconducting, and there are weak Josephson links between them. Magnetic field $H>H_{crSIT}$ breaks weak links. The dissipative state arises. Resistance reaches the maximum because of Cooper pair tunneling through normal regions is blocked by the potential barrier which height is commensurate with the energy of the superconducting gap. Conductivity of the system is now determined only by low probability of single-particle tunneling due to the small number of quasiparticles at the Fermi level. The transport current increase leads to the destruction of superconductivity directly in the superconducting granules (decoupling of Cooper pairs). Number of quasiparticles at the Fermi level rises, the single-particle charge carriers begin to contribute to the conductivity of the system [17] and the resistance decreases (Fig.3).

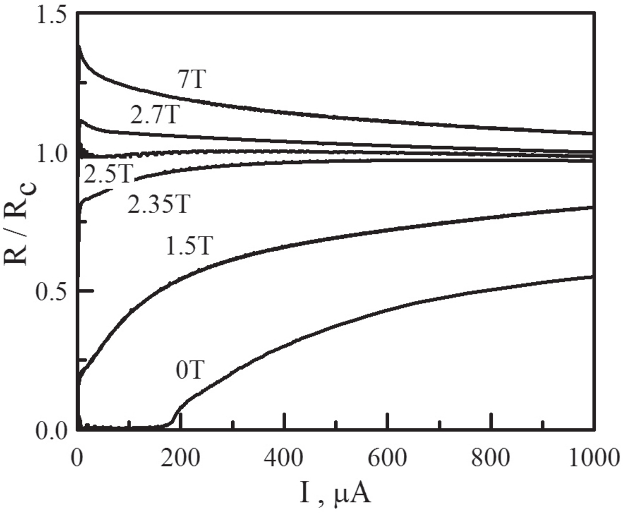

Fig.3. R(I) dependences at different values of parallel magnetic field. *T*=1.5K.

On another side, the transport current increase causes a corresponding increase of voltage at the boundaries of superconducting islands, thus reducing the height of the potential barriers between them. Therefore, the tunneling probability rises and tends to reduce the resistance.

Similar experimental results were obtained in [18] in the thick amorphous bismuth films. The authors of this work suggest a different interpretation of the experimental results within the framework of the hypothesis of overheating of the electron gas. For a final clarification of the mechanism of this phenomenon, we need more experimental data for large values of the transport current in strong magnetic fields.

The temperature dependence of the critical magnetic field of transport current induced SIT is obtained. As seen in Fig.4, the critical field at which we see horizontal separatrix (H_{crSIT}) and cross point on $R(H)$ curves increases with temperature decrease. The dependence $H_{crSIT}(T)$ separates the superconducting state and the state of the localized superconductivity.

Thus, for the first time the possibility of transport current assisted the superconductor-insulator transition is shown in superconducting nanostructures based on heterostructures PbTe/PbS. This phase diagram with $H_{c2}(T)$ and $H_{crSIT}(T)$ curves separate the superconducting state and the state of the localized superconductivity.

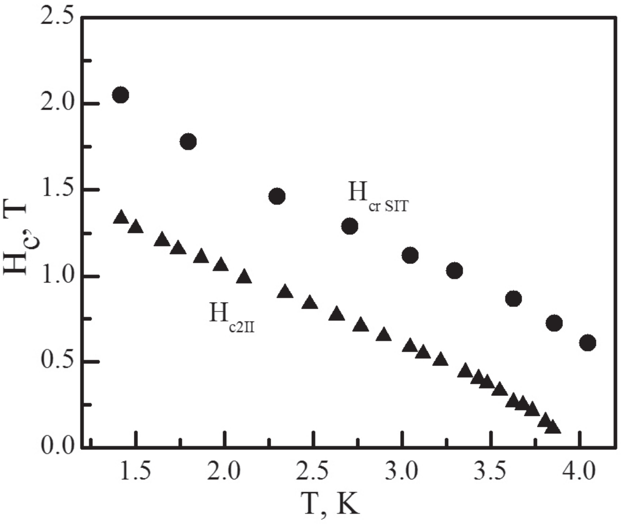

Fig.4. Temperature dependence of the critical magnetic field of SIT and the temperature dependence of upper critical fields.

Acknowledgments

Author is very grateful to A.Yu.Sipatov for technical assistance with the sample preparation and characterization, S.V.Bengus for useful discussion of the experimental results.

Conclusions

1. It is shown that all of the typical features of the SIT (the fan-like set of *R*(*I*) dependences at different magnetic fields, the crossing of *R*(*H*) curves in a single point at different transport currents) are observed in PbTe/PbS geterostructures with the island-like superconducting interface. The mechanism of the SIT realization is similar to that one which realizes in granular systems with the percolation conductivity. The possibility of realization of a transport current induced superconductor-insulator transition is shown.

2. The dependence of the critical magnetic field of the SIT is obtained.

3. It is shown that $A^{IV}B^{VI}$-type heterostructures can serve as model objects for the study of effects of localized superconductivity, because we can vary the topology of the superconducting interface at the preparation stage.

1. O. A. Mironov, B. A. Savitskii, A. Yu. Sipatov, A. I. Fedorenko, A. N. Chirkin, S. V. Chistyakov, and L. P. Shpakovskaya, *Pis'ma Zh. Eksp. Teor. Fiz.* **48,** 100 (1988) [*JETP Lett.***48**, 106 (1988).
2. A. I. Fedorenko, V. V. Zorchenko, A. Yu. Sipatov, O. A. Mironov, S. V. Chistyakov, and O. N. Nashchekina, *Fiz. Tverd. Tela* **41**, 1693 (1999) [*Phys. Solid State* **41**,

1551 (1999)].

3. N. Ya. Fogel, A.S. Pokhila, Yu.V. Bomze, A.Yu. Sipatov, A.I. Fedorenko, and R.I. Shekhter, *Phys. Rev. Lett.* **86**, 512 (2001).
4. N.Ya. Fogel, E.I. Buchstab, Yu.V. Bomze, O.I. Yuzephovich, M.Yu. Mikhailov, A.Yu. Sipatov, E.A. Pashitskii, R.I. Shekhter, and M. Jonson, *Phys. Rev. B* **73,** 161306(R) (2006).
5. N.Ya. Fogel, E.I. Buchstab, Yu.V. Bomze, O.I. Yuzephovich, A.Yu. Sipatov, E.A. Pashitskii, A. Danilov, V. Langer, R.I. Shekhter, and M. Jonson, *Phys. Rev. B* **66**, 174513 (2002).
6. O. I. Yuzefovich, M. Yu. Mikhailov, S. V. Bengus, A. Yu. Aladyshkin, E. E. Pestov, Yu. N. Nozdrin, A. Yu. Sipatov, E. I. Buchstab, and N. Ya. Fogel’, *Fiz. Nizk. Temp*.**34**, 1249 (2008) [*Low Temp. Phys*. **34**, 985 (2008).
7. V. F. Gantmakher and V. T. Dolgopolov, *Usp. Fiz. Nauk* **180**, 3 (2010) [*Phys. Usp*.**53**, 1 (2010)].
8. A.M. Goldman, *Int. J. Mod. Phys. B* **24**, 4081 (2010).
9. V.M. Galitski and A.I.Larkin, *Phys. Rev. B* **63**, 174506 (2001).
10. M.P.A. Fisher, *Phys. Rev. Lett*. **65**, 923 (1990).
11. K. B. Efetov, *Zh. Eksp. Teor. Fiz*. **78**, 2017 (1980) [*Sov. Phys*. *JETP* 51, 1015 (1980)].
12. I.S. Beloborodov, A.V. Lopatin, and V.M. Vinokur, K.B. Efetov, *Rev. Mod. Phys*. **79**, 469 (2007).
13. P. Delsing, C.D. Chen, D.B. Haviland, Y. Harada and T. Claeson, *Phys. Rev. B* **50**, 3959 (1994).
14. H.S.J. van der Zant, F.C. Fritschy, W.J. Elion, L.G. Geerlings and J.E. Mooji, Phys. Rev. Lett. **69**, 2971 (1992).
15. H.S.J. van der Zant, W.J. Elion, L.G. Geerlings and J.E. Mooji, *Phys. Rev. B* **54**, 10081 (1996).
16. Watson Kuo and C.D. Chen, *Phys. Rev. Lett*. **87**, 186804 (2001).
17. S.V. Bengus, A.Yu. Sipatov, O.I. Yuzephovich, *Low Temp. Phys*. **v.39**, 695 (2013).
18. O.I. Yuzephovich, S.V. Bengus, A.Yu. Sipatov, Vestnik KNU, seria «Physica», 81 (2013).
19. L.S. Palatnik, A.I. Fedorenko, *J. Cryst. Grow* **52**, 917 (1981).
20. B.I. Belevtsev, N.V. Dalakova A.S. Panfilov E.Yu. Beliayev, *Physica B*, **405**, 1307 (2010).
21. K.A.Parendo, K. H. Sarwa B. Tan, and A. M. Goldman, Hot-electron effects in the twodimensional superconductor-insulator transition, *Phys. Rev*. B **74**, 134517 (2006).

Вісник ХНУ, № 1158, серія «Фізика», вип. 22, 2015. с. 68-70

UDK 539.37
PACS numbers: 61.72. – y + 83.50. – v

Healing the cracks in crystalline solids under uniaxial compression normal to the plane of crack deposition

M.A. Volosyuk

Kharkov National Automobile and Highway University,
Petrovskogo st, 25, 61002, Kharkov, Ukraine

The results of experimental and theoretical investigations on the process of healing the artificially created disc-like cracks in uniaxially compressed samples of galvanic purified (99.999%) polycrystalline copper at room (T_{room}) and high (T=873 K) temperatures are described. It has been shown that at $T=T_{room}$ under loading, cracks emitting dislocation loops reduce their radius to some stationary value depending on loading; dislocation mechanism of healing takes place. The obtained calculated dependence of the crack radius on loading has been experimentally supported.

It has been shown that at high temperature, the formed after loading dislocation assemblage becomes quasi-stationary due to diffusion dissolving the dislocation loops and generating the new ones – that is dislocation-diffusion mechanism of healing. The calculated relations describing the process have been obtained and experimentally tested. The assumption has been made on possible dissolution of dislocation loops at the expense of absorption of interstitial atoms migrating over lattice by crowdion mechanism.

Keywords: crack, dislocation loop, stationary and quasi-stationary state, interstitial atom, crowdion, dislocation and dislocation-diffusion mechanism.

Изложены результаты экспериментального и теоретического исследований процесса залечивания дискообразных искусственно созданных трещин в одноосно сжимаемых образцах гальванически очищенной (99,999 %) поликристаллической меди при комнатной (T_{room}) и высокой (Т=873 К) температурах. Показано, что при $T=T_{room}$ при нагружении образца трещины, испуская дислокационные петли, уменьшают свой радиус до некоторого стационарного значения, зависящего от нагрузки – дислокационный механизм залечивания. Полученная расчетная зависимость радиуса трещины от нагрузки экспериментально подтверждена.

Показано, что при высокой температуре образующееся после нагружения дислокационное скопление вследствие диффузионного растворения дислокационных петель и рождения новых становится квазистационарным – дислокационно-диффузионный механизм залечивания. Получены расчетные соотношения, описывающие указанный процесс, которые проверены экспериментально. Высказано предположение о возможном растворении дислокационных петель за счет поглощения межузельных атомов, мигрирующих в решетке краудионным механизмом.

Ключевые слова: трещина, дислокационная петля, стационарное и квазистационарное состояния, межузельный атом, краудион, дислокационный и дислокационно-диффузионный механизмы.

Викладені результати експериментального і теоретичного досліджень процесу заліковування дископодібних штучно створених тріщин в зразках гальванічно очищеної (99,999 %) полікристалічної міді, що одноосно стискаються, при кімнатній (T_{room}) і високій (Т=873 К) температурах. Показано, що при $T=T_{room}$ при навантаженні зразка тріщини, випускаючи дислокаційні петлі, зменшують свій радіус до деякого стаціонарного значення, залежного від навантаження, – дислокаційний механізм заліковування. Отримана розрахункова залежність радіусу тріщини від навантаження експериментально підтверджена.

Показано, що при високій температурі дислокаційне скупчення, що утворюється після навантаження, унаслідок дифузійного розчинення дислокаційних петель і народження нових стає квазістаціонарним – дислокаційно-дифузійний механізм заліковування. Отримані розрахункові співвідношення, що описують вказаний процес, які перевірені експериментально. Висловлено припущення про можливе розчинення дислокаційних петель за рахунок поглинання міжвузельних атомів, мігруючих в решітці краудіонним механізмом.

Ключові слова: тріщина, дислокаційна петля, стаціонарний і квазістаціонарний стани, міжвузельний атом, краудіон, дислокаційний і дислокаційно-дифузійний механізми.

Introduction

Behavior of cracks in single crystals determines in many aspects their carrier ability and durability of work under loading. Studying the possibilities of healing remains a problem actual at all times. It is known that in plastic materials the cracks are able to self-healing (if mouths of cracks are sharp enough), and the plastic zone occurs around the crack [1-3]. This phenomenon is analogous to the effects of plasticity under powders sintering and self-compaction. Under uniaxial loading, like under full compression, crack healing by the dislocation-diffusion mechanism may be expected.

In the present work, we give the results of studying the mechanisms and kinetics of crack healing under uniaxial loading at low (room) and high (T=873 K) temperatures.

Materials and methods of the experiment

As the sample material, pure (99.999 %) and well annealed polycrystalline copper was used as both widely used material and suitable model object.

Each sample with cracks consisted of two plates with sizes (20×20×5) mm. One of the surfaces (20×20) mm of each plate was properly treated as to its flatness and mirror smoothness. In one of the plates, flat-bottom hollows with diameter to 1.5 mm and depth ($10^{-4}\div10^{-3}$) cm were made using a special attachment. The plates were joined by pairs (with and without hollows) and then were subjected to diffusion welding at *T=1073 K* in vacuum ($10^{-5}\div10^{-4}$) mm Hg during 30 min under loading below Peierls threshold, afterwards were annealed in vacuum 10^{-4} mm Hg without loading at *T=1073 K*for structure normalization. The initial sizes of cracks in the samples obtained were the following: radius $a_0=(2\div5)\cdot10^{-2}$ cm and thickness $(3\div5)\cdot10^{-4}$ cm. Experiments were carried out at room (T_{room}) and high (T=873 K) temperatures. Crack sizes were measured using an optical microscope.

Results and Discussion

Under applied loading, the stress state occurs in the neighborhood of the crack mouth, while on the surface of the mouth – dislocation loops of vacancy type are generated forming a dislocation assemblage with opposite stress deactivating the source on the mouth surface, so the healing process comes to stop. The crack radius attains some stable value *a* corresponding to a given value of applied stress σ; the both are related as:

$$1-\left(\frac{a}{a_0}\right)^2 = B\sigma^3, \qquad (1)$$

where $B=\dfrac{2\pi(1-\nu)c^{1/2}}{a_0^{1/2}G\sigma_p^2}$, ν is Poisson coefficient, a_0 is initial radius of the crack, *c* is thickness (or height) of the crack, *G* is shear modulus, σ_p is critical stress of shear (Peierls barrier).

Such state will be stable, if the assemblage formed near the mouth is stable. This is possible at low (room) temperature. Obtained experimental data represented in coordinates $1-(a/a_0)^2$ versus σ^3 are really linearized (Fig. 1), and σ_p value following from the plot slope is quite reasonable: $\sigma_p/G\approx0,5\cdot10^{-5}$.

In the extreme case of high temperature [2], vacancy type prismatic dislocation loops quickly formed a dislocation assemblage and reduced the crack radius from a_0 to a_0', are dissolved by diffusion; the opposite stress of the dislocation assemblage decreases that gives a possibility to generating new loops and further healing. At any temperature, generation of dislocation loops begins immediately after loading application, and the dislocation assemblage occurs quickly with corresponding reducing the crack radius to a'_0. At low temperature a'_0 is some stable value corresponding to a given loading level.

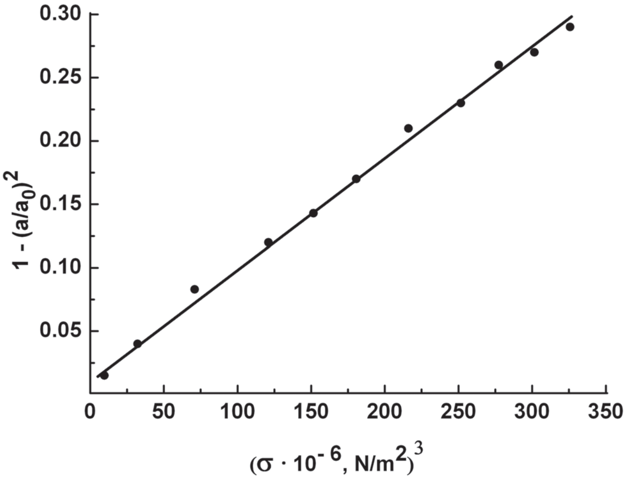

Fig.1. Dependence $1-(a/a_0)^2$ on σ^3.

At high temperature, a'_0 radius corresponds to loops coming out from the crack mouth for forming a quasi-stationary assemblage. This is initial state for further crack healing due to diffusion dissolution of the assemblage loops and replacement these by new loops (Fig. 2).

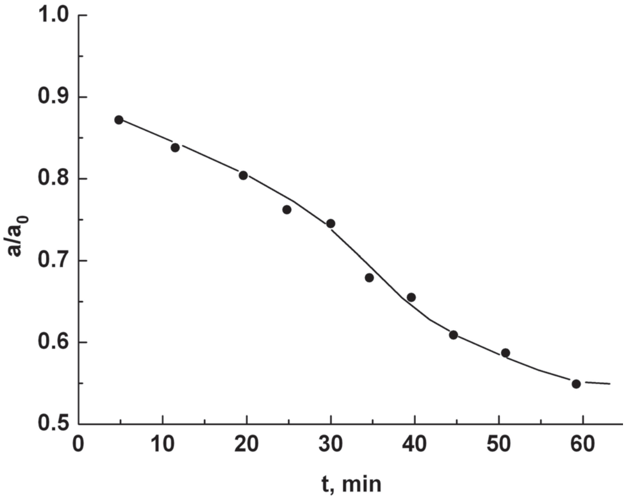

Fig.2. Dependence of stabilized relative crack size (a/a_0) on loading exposure time *t* under external compressive loading $\sigma\approx5\cdot10^6$ N/m².

Such mechanism of healing is called as dislocation-diffusion one.

Kinetic equation describing the dependence *a(t)* can be obtained, if to equate the flux of "emptiness" brought out from the crack volume dV_{cr}/dt to the "emptiness" flux from dissolved dislocation assemblage surrounding the mouth, and to take into consideration the equality of the dislocation assemblage opposite stress σ_{tur} and the stress caused by external loading σ; as a result we obtain a differential equation [3] from which it follows:

$$1-\left(\frac{a}{a_0'}\right)^2=\left(\alpha\gamma+\alpha\beta D_V\Delta C_i\right)\frac{\left(t-t_0\right)}{\sigma_p^2}, \qquad (2)$$

where $\alpha=\frac{2}{\left(a_0'\right)^2}\frac{\pi a_0^{3/2}\sigma^3}{c^{3/2}}$, $\beta=\frac{4\pi\left(1-\nu\right)R_l}{Gb\ln\left(8R_l/b\right)}$,

$\gamma=\frac{D\omega}{kT}$, t, t_0 are, respectively, the current time and the time for formation of a quasi-stationary dislocation assemblage at the vertex of the crack (here t_0 = 5 min); a_0, a, a_0' are, respectively, initial (before loading) and current radii of the crack, and radius to time t_0 ($a_0 = 4.5\cdot10^{-4}$ m, $a_0' = 0.88\ a_0$); $c = 4\cdot10^{-6}$ m is crack thickness; $\nu = 0.3$ is Poisson coefficient; $b \approx 3\cdot10^{-10}$ m is Burgers vector; $\omega = 1.18\cdot10^{-29}$ m^3 is atomic volume; $k = 1.38\cdot10^{-23}$ J/K is Boltzmann constant ; T is experimental temperature (T = 873 K); R_l is radius of an emitting dislocation prismatic loop (taken as $R_l \approx c/2 = 2\cdot10^{-6}$ m); $G = 4.15\cdot10^{10}$ N/m^2 is shear modulus in copper; $\sigma \approx 5\cdot10^6$ N/m^2 is stress from external loading; D is self-diffusion coefficient of atoms in copper (at T = 873 K, $D = 3.1\cdot10^{-17}$ m^2/s); $D = D_V C^0_V$; D_V is vacancy diffusion coefficient; C^0_V is equilibrium concentration of vacancies at given temperature T; $\Delta C_i = C_i - C^0_i$ is supersaturation of the lattice by interstitial atoms; C_i, C^0_i are, respectively, real and equilibrium concentrations of interstitials at temperature T; σ_p is Peierls threshold.

The first term in parentheses corresponds to contribution into crack healing of loops diffusion dissolution by vacancy mechanism, and the second – to contribution of loop diffusion dissolution into crack healing due to absorption of interstitial atoms. The first term is the known value. In the second one – ΔC_i is unknown. If $\Delta C_i=0$ is assumed, then after plotting dependence (a/a'_0) versus $(t-t_0)$ in coordinates $1-(a/a'_0)^2$ versus $(t-t_0)$ from the plot slope we obtain $\sigma_p/\mathrm{G}\approx 0{,}34$. This value, in principle, is reasonable for given experimental conditions therefore we cannot estimate the contribution of interstitials.

On the other hand, it is known that under conditions like local plastic deformation, there take place intersections of dislocation screw parts generating interstitials and vacancies [4]. Concentrations of both components are almost equal. But, because of high mobility of interstitials [4] the quantity of generated interstitial atoms is larger therefore these are in excessive concentration.

The second circumstance is related with the fact that external applied stress lowers energy barrier for generation of an interstitial by the value σbla, and concentration of interstitials can be determined from the relation [4]:

$$C_i=Be^{-\frac{U_{fi}-\sigma bla}{kT}}. \qquad (3)$$

According to [4], $\mathrm{B}\approx 1$, l is length of a dislocation assemblage. If to assume the terms in parentheses of (2) be equal, it follows: $\Delta C_i \approx C_i \approx 6{,}2\cdot10^{-13}$. From (3) it follows that at $\sigma\approx 5\cdot10^6$ N/m^2, it should be $l\approx\frac{U_{fi}+kT\ln C_i}{\sigma ba}\approx(4{,}6\div 4{,}8)\cdot10^{-7}$ m. This l value is in accordance with data from [4], therefore the assumption on the possible participation of interstitial transfer is reasonable. The most probable mechanism of interstitial atom migration may be "relay-race" motion in a close-packed ray in the form of crowdion configuration [5, 6].

Conclusions

It has been shown in the work that at low temperature there takes place dislocation mechanism of healing; its result is determined by the level of loading applied.

At high temperature, due to diffusion dissolution of dislocation loops and generation of new ones, the healing process becomes permanent and is described by the kinetic equation (dislocation-diffusion mechanism of healing). It follows from experiments that dissolution of dislocation prismatic loops may be caused not only by action of the vacancy diffusion mechanism, but also by absorption of interstitial atoms which occur in excess concentration in plasticity processes within crack mouth and migrate over the lattice in the form of crowdion configurations.

1. Yu.I. Boyko, M.A. Volosyuk. *Visnyk KhNU, ser. «Fizyka»*. 17, 1020, 42 (2012).
2. Yu.I. Boyko, M.A. Volosyuk, V.G. Kononenko. *Functional Materials*, 19, 245 (2012).
3. M.A. Volosyuk, A.V. Volosyuk, N.Ya. Rokhmanov. *Functional Materials*, 22, 51 (2015).
4. J.Hirth, J.Lothe. Theory of dislocations, McGraw-Hill, New York (1968), 600 p.
5. V.D. Natsik, S.N. Smirnov, E.I. Nazarenko. *FNT,* 27, 1295 (2001).
6. M.A. Volosyuk, *Problems of Atomic Science and Technology*, 4 (92), 55 (2014).

ІНФОРМАЦІЯ ДЛЯ АВТОРІВ СТАТЕЙ

журналу «Вісник ХНУ». Серія «Фізика»

У журналі «Вісник ХНУ». Серія «Фізика» друкуються статті та стислі за змістом повідомлення, в яких наведені оригінальні результати теоретичних та експериментальних досліджень, а також аналітичні огляди літературних джерел з різноманітних актуальних проблем фізики за тематикою видання.

Мова статей – українська, російська та англійська.

ТЕМАТИКА ЖУРНАЛУ

1. Теоретична фізика.
2. Фізика твердого тіла.
3. Фізика низьких температур.
4. Фізика магнітних явищ.
5. Оптика та спектроскопія.
6. Загальні питання фізики і серед них: методологія та історія фізики, математичні методи фізичних досліджень, методика викладання фізики у вищій школі, техніка та методика фізичного експерименту тощо.

ВИМОГИ ДО ОФОРМЛЕННЯ РУКОПИСІВ СТАТТЕЙ

Загальний обсяг тексту рукопису статті повинен займати не більше, ніж 15 сторінок.

Рукопис статті складається з титульної сторінки, на якій вказанно: назва статті; ініціали та прізвища авторів; поштова адреса установи, в якій була виконана робота; класифікаційний індекс за системами PACS та УДК; анотації на окремому аркуші з прізвищем та ініціалами авторів і назвою статті, викладені українською, російською та англійською мовами; основний текст статті; список літератури; підписи під рисунками; таблиці; рисунки: графіки, фотознімки.

Текст рукопису треба роздрукувати на принтері з подвійним інтервалом на аркуші паперу формату А4 (210x297) з полями ліворуч, праворуч, зверху і знизу по 2,5 см, шрифтом розміром 14 pt гарнітурою TimesNewRoman.

Електронний варіант рукопису статті повинен відповідати таким вимогам: текст рукопису статті повинен бути набраний у форматі MicrosoftWord версії 2003, вирівнювання тексту повинне бути здійснене за лівим краєм, розмір шрифту 10 pt, гарнітураTimesNewRoman, без відступів і виступів, без відступів після абзаців, без прописних букв у назвах, букви звичайні рядкові, накреслення жирного й курсивного шрифту не допускається, формули повинні бути набрані в MathType (не нижче версії 6,5), у формулах кирилиця не допускається, символи з нижніми і верхніми індексами слід набирати в MicrosoftWord, ширина формули не більше 70 мм, графіки та фотографії необхідно подавати в графічному форматі, кольоровий рисунок повинен бути в рукописі чорно-білим (grayscale), розрізнення не менше 300 dpi, поширення файлів повинно бути *.jpg, шириною в одну чи дві колонки, для однієї колонки розміри: завширшки 8 мм, для двох колонок – 16 мм. Масштаб на мікрофотографіях необхідно представляти у вигляді масштабної лінійки.

ВИМОГИ ДО ОФОРМЛЕННЯ ГРАФІКІВ

Товщина ліній не більше 0,5 мм, але не менше 0,18 мм. Величина літер на підписах до рисунків не більш 14 pt , але не менше 10 pt, гарнітура Arial.

ПРИКЛАД ОФОРМЛЕННЯ СПИСКУ ЛІТЕРАТУРИ

1. Л.Д. Ландау, Е.М. Лифшиц. Теория упругости, Наука, М. (1978), 730 с.
2. И.И. Іванов. ФТТ, 25, 7, 762 (1998).
3. A.D. Ashby. Phys.Rev., A19, 213 (1985).
4. D.V. Vert. In Progress in Metals, ed. by R. Speer, USA, New York (1976), v.4, p.17.

ДО РЕДАКЦІЇ НАДАЄТЬСЯ

1. Два роздруковані примірники рукопису статті, які підписані її авторами.
2. Електронна версія рукопису та дані щодо контактів для спілкування з її авторами. Для цього потрібно надіслати електронною поштою, тільки на адресу vestnik_phy@mail.ru.
3. Направлення від установи, де була виконана робота, і акти експертизи у двох примірниках; адресу, прізвище, повне ім’я та батькові авторів; номери телефонів, E-mail, а також зазначити автора рукопису, відповідального за спілкування з редакцією журналу.

Матеріали рукопису статті потрібно направляти за адресою: Редакція журналу «Вісник Харківського національного університету імені В.Н. Каразіна. Серія: фізика», Криловському В.С., фізичний факультет, майдан Свободи, 4, Харківський національний університет імені В.Н. Каразіна. тел. (057)-707-53-83.

Наукове видання

Вісник Харківського національного університету імени В.Н.Каразіна

№ 1158

Серія “Фізика”

випуск 22

Збірник наукових праць

Українською, російською та англійською мовами.

Комп’ютерне верстання С.В. Лебедєв

Підписано до друку 08.07.2015. Формат 60x84 1/8.

Папір офсетний. Друк ризограф. Ум. друк. арк. 8,7. Обл.-вид. арк 13,7.

Тираж 100 пр.

Надруковано: ХНУ імені В.Н. Каразіна
61022, Харків, майдан Свободи, 4.
Тел.705-24-32

Свідоцтво суб'єкта видавничої справи ДК №3367 від 13.01.09